

UC San Diego
Scripps Institution of Oceanography Technical Report

Title

Mesoscale Coupled Ocean-Atmosphere Interaction

Permalink

<https://escholarship.org/uc/item/8w71d1hk>

Author

Seo, Hyodae

Publication Date

2007-07-09

UNIVERSITY OF CALIFORNIA, SAN DIEGO

Mesoscale Coupled Ocean-Atmosphere Interaction

A dissertation submitted in partial satisfaction of the
requirements for the degree Doctor of Philosophy

in

Oceanography

by

Hyodae Seo

Committee in charge:

Arthur Miller, Co-Chair
John Roads, Co-Chair
Guillermo Algaze
Sarah Gille
Glenn Ierley
Andrew Moore
Joel Norris

2007

Copyright

Hyodae Seo, 2007

All rights reserved.

The dissertation of Hyodae Seo is approved, and it is acceptable in quality and form for publication on microfilm:

Co-Chair

Co-Chair

University of California, San Diego

2007

TABLE OF CONTENTS

Signature Page.....	iii
Table of Contents.....	iv
List of Figures and Tables.....	vii
Acknowledgments	ix
Vita	xi
Abstract	xii
Chapter 1. Introduction.....	1
Chapter 2. The Scripps Coupled Ocean-Atmosphere Regional Model (SCOAR)	
Model with Applications in the Eastern Pacific Sector	7
Abstract	7
2.1 Introduction.....	8
2.2 Regional Coupled Modeling Background	10
2.3 The SCOAR Model.....	13
2.3.1 RSM atmospheric model.....	13
2.3.2 ROMS ocean model.....	14
2.3.3 Flux-SST Coupler.....	15
2.4 Examples of SCOAR Model Simulations	17
2.4.1 TIWs in the ETP	18
2.4.1.1 Background	18
2.4.1.2 Results.....	19
2.4.2 Mesoscale Eddy Feedbacks in the CCS.....	24
2.4.2.1 Background	24
2.4.2.2 Results.....	25
2.4.3 Gap Winds in the CAC	28
2.4.3.1 Background	28

2.4.3.2 Results.....	30
2.5 Summary and Discussion	31
2.6 Acknowledgments.....	33
Chapter 3. Feedback of Tropical Instability Wave - induced Atmospheric Variability	
onto the Ocean.....	49
Abstract	49
3.1 Introduction.....	50
3.2 Model and Experiment.....	53
3.3 Results	56
3.3.1 Impact of Wind-Current Covariability on the TIWs	56
3.3.2 Impact of Surface Current on Wind Stress	62
3.3.3 Implication of TIW-induced latent Heat Flux on SST	65
3.4 Summary and Discussion	67
3.5 Acknowledgments.....	71
Chapter 4. Effect of Ocean Mesoscale Variability on the Mean State of Tropical	
Atlantic Climate.....	83
Abstract	83
4.1 Introduction.....	83
4.2 Model and Experiment Setup.....	84
4.3 Results	86
4.4 Summary and Discussion	88
4.5 Acknowledgments.....	90
Chapter 5. Precipitation from African Easterly Waves in a Coupled Model of the	
Tropical Atlantic Ocean.....	95
Abstract	95
5.1 Introduction.....	96

5.2 Models and Experiment.....	99
5.3 AEW-induced Low-level Convergence and Precipitation: Sensitivity to Model Resolution	103
5.4 Impact on the Larger-scale Mean Precipitation and SST.....	110
5.4.1 Mean Seasonal Cycle of the ITCZ	110
5.4.2 Large-scale SST Distribution	112
5.5 Conclusion and Discussion.....	115
5.6 Acknowledgments.....	117
Chapter 6. Summary and Future Plans	131
6.1 Summary of Results	131
6.2 Future Plans	135
References.....	138

LIST OF FIGURES AND TABLES

Table 2.1 Model domain specification	35
Figure 2.1 Schematic description of the Scripps Coupled Ocean-Atmosphere (SCOAR) Model	36
Figure 2.2 Model domain, bathymetry and orography Model domain, bathymetry and orography	37
Figure 2.3 Three-day averaged oceanic and atmospheric states	38
Figure 2.4 Spatial relationship of the SST and wind stress	39
Figure 2.5 Hovmöller diagram of model SST and wind stress along 1°N	40
Figure 2.6 Same as Figure 2.5, except along 4°S	41
Figure 2.7 Binned scatter plots of wind stress and SST	42
Figure 2.8 Same as Figure 2.4, except latent and sensible heat flux with the SST	43
Figure 2.9 Longitude-vertical cross-sections of atmospheric and oceanic temperature ..	44
Figure 2.10 Thirty-day averaged SST and wind stress in July 2003	45
Figure 2.11 Binned scatter plots of wind stress and heat flux with SST	46
Figure 2.12 Model climatology of wind stress vector and Ekman pumping	47
Figure 2.13 Same as Figure 2.12 except for SST	48
Figure 3.1 Three-day averaged SST and 10-m winds	72
Figure 3.2 Time-mean zonal current along 23°W and the surface eddy kinetic energy ..	73
Figure 3.3 Three-day averaged model SST fields with the vectors of model surface current and the vectors of model wind stress	74
Figure 3.4 Three-day averaged highpass filtered model SST overlaid with model surface current and model wind stress	75
Figure 3.5 Schematic representation of the relationship between wind stress and surface current over TIW-SST	76

Figure 3.6 Map of correlation of highpass filtered model wind stress and current	77
Figure 3.7 Zonal average of time mean barotropic conversion rate of the zonal flow and $\vec{u}'_{sfc} \cdot \vec{\tau}'_z$ averaged over 150 m.....	78
Figure 3.8 Hovmöller diagrams of the model perturbation vertical velocity and the model Ekman pumping velocity at 2°N	79
Figure 3.9 Time-series of model wind stresses at 2°N averaged over 20°W-15°W	80
Figure 3.10 Maps of ratio of annual mean of $ \vec{\tau}_1 - \vec{\tau}_2 $ to the annual mean of $ \vec{\tau}_1 $ and 5-day averaged ratio of $ \vec{\tau}_1 - \vec{\tau}_3 $ to $ \vec{\tau}_1 $	81
Figure 3.11 Six-year time series of $\rho LC_H \overline{U\Delta q}$ and $\rho LC_H \overline{U'\Delta q'}$ at 2°N.....	82
Figure 4.1 Mean SST from the model simulation and the observations.	92
Figure 4.2 Same as Figure 4.1, except for 10-m wind speed and vectors.	93
Figure 4.3 Same as Figure 4.1, except for precipitations.	94
Figure 5.1 Summertime mean wind, vorticity (700 hPa) and temperature (925 hPa)	119
Figure 5.2 Variance of 2-6 day filtered 850 hPa meridional wind.....	120
Figure 5.3 Hovmöller diagrams of 2-6 day band-passed 850 hPa meridional wind.....	121
Figure 5.4 Hovmöller diagrams of 2-6 day band-passed convergence	122
Figure 5.5 Two-day averages model rainfall, 10-m winds and convergence.	123
Figure 5.6 Time-series of rainfall from the PIRATA mooring and the model.	124
Figure 5.7 PDFs of 10-m wind convergence.	125
Figure 5.8 Ratio of variance of 2-6 band-pass filtered rainfall to the total rainfall.	126
Figure 5.9 Six-year mean rainfall from model and the observations.	127
Figure 5.10 Seasonal variation of latitude of the maximum precipitation.	128
Figure 5.11 Six-year mean SST and the mean difference of SST and heatflux.	129
Figure 5.12 Seasonal cycle of SST and meridional gradient of SST.	130

ACKNOWLEDGMENTS

My first thanks go to my advisors Art Miller and John Roads. Their support, encouragement and enthusiasm made all the difference in my graduate career. I am grateful for a treasured friendship that they kindly extended to me. I am also thankful for their time and effort in reading my terrible drafts. They painstakingly edited disastrous grammar and gave useful suggestions, which were essential to the completion of this dissertation. Thanks Art and John!

I would also like to thank my committee members: Guillermo Algaze, Sarah Gille, Glenn Ierley, Andrew Moore, and Joel Norris, for their comments and contribution to my dissertation research. Special thanks go to Markus Jochum and Raghu Murtugudde, who always instigated my research with insightful and challenging questions.

I express thanks to Masao Kanamitsu, Guillermo Auad, Emanuele Di Lorenzo and many other researchers for their invaluable suggestions throughout my dissertation research. Administrative and technical support was outstanding and I appreciate the assistance from Jack Ritchie, Patrick Tripp, Martin Olivera, Caroline Papadopoulos, Diane Boomer, Shivani Singh, Nirvana Singh, Kharyn Loteyro, the Climate Research Division, and the SIO Graduate Department.

I also thank my fellow students, researchers, and friends at Scripps, all of whom made my past 5 years here at Scripps memorable and valued. Theresa Carpenter was my office mate for 4 years, and I am thankful that she was. Finally, I thank my parents and family in Korea for their continued support from distance. They have been my ultimate source of support and energy.

Chapter 2, in full, is a reproduction of the material as it appears as Seo, H., A. J.

Miller, and J. O. Roads, The Scripps Coupled Ocean-Atmosphere Regional (SCOAR) Model, with Applications in the Eastern Pacific Sector, *Journal of Climate*, **20**, 381-402, 2007. Chapter 3 will appear in full as Seo, H., M. Jochum, R. Murtugudde, A. J. Miller, and J. O. Roads, Feedback of Tropical Instability Wave – induced Atmospheric Variability onto the Ocean, *Journal of Climate*, in press, 2007. Chapter 4, in full, a reproduction of the material as it appears as Seo, H., M. Jochum, R. Murtugudde, and A. J. Miller, Effect of Ocean Mesoscale Variability on the Mean State of Tropical Atlantic Climate, *Geophysical Research Letters*, **33**, L09606, 2006. Chapter 5, in full, is a reproduction of the material as it appears as Seo, H., M. Jochum, R. Murtugudde, A. J. Miller, and J. O. Roads, Precipitation from African Easterly Waves in a Coupled Model of the Tropical Atlantic Ocean, accepted, 2007.

I, the dissertation author, was the primary investigator and the author of these papers, and conducted all of the analysis presented therein and prepared the manuscripts for the publication. The coauthors provided useful discussions and contributed to revising the original draft of the paper.

My dissertation research was supported by Department of Energy (DE-FG02-04ER63857) and National Oceanic and Atmospheric Administration (NA17RJ1231 through ECPC). We acknowledge the additional funding source by the NOAA Grant, ‘Impact of oceanic mesoscale variability on the coupled climate’. I also thank the Center for Observations, Modeling and Prediction at Scripps (COMPAS) and Caroline Papadopoulos for providing computing time and technical assistance.

VITA

2002	Bachelor of Science, Yonsei University, South Korea
2002-2007	Research Assistant, University of California, San Diego
2007	Doctor of Philosophy, University of California, San Diego

PUBLICATIONS

- Seo, H., M. Jochum, R. Murtugudde, A. J. Miller, and J. O. Roads: Precipitation from African Easterly Waves in a Coupled Model of the Tropical Atlantic Ocean. *Journal of Climate*, accepted
- Small, R. J., S. de Szoeke, S. P. Xie, L. O'Neill, H. Seo, Q. Song, P. Cornillon, M. Spall, and S. Minobe: Air-Sea Interaction over Ocean Fronts and Eddies. *Dynam. Ocean. Atmos.*, in press
- Seo, H., M. Jochum, R. Murtugudde, A. J. Miller, and J. O. Roads: Feedback of Tropical Instability Wave-induced Atmospheric Variability onto the Ocean. *Journal of Climate*, in press
- Seo, H., A. J. Miller and J. O. Roads, 2007: The Scripps Coupled Ocean-Atmosphere Regional (SCOAR) Model, with applications in the eastern Pacific Sector. *Journal of Climate*, **20**, 381-402
- Seo, H., M. Jochum, R. Murtugudde, and A. J. Miller, 2006: Effect of Ocean Mesoscale Variability on the Mean State of Tropical Atlantic Climate. *Geophysical Research Letters*, **33**, L09606, doi:10.1029/2005GL025651

ABSTRACT OF THE DISSERTATION

Mesoscale Coupled Ocean-Atmosphere Interaction

by

Hyodae Seo

Doctor of Philosophy in Oceanography

University of California, San Diego, 2007

Arthur Miller, Co-Chair

John Roads, Co-Chair

This dissertation studies mesoscale ocean-atmosphere interaction using the newly developed Scripps Coupled Ocean-Atmosphere Regional (SCOAR) model. The overall goal of this study is to understand the physical processes that lie behind mesoscale ocean-atmosphere interactions and their connection with the basin-scale climate variability.

SCOAR allows air-sea feedbacks arising from the oceanic mesoscale features. The model is tested in three scenarios in the eastern Pacific Ocean sector: tropical instability waves (TIWs) of the eastern tropical Pacific; mesoscale eddies and fronts of the California Current System; and gap winds of the Central American Coast. The model reproduces aspects of the observed linear response of the atmosphere to the evolving sea surface temperatures (SST). This results in significant anomalies of wind stress curl/divergence, surface heat flux and precipitation that resemble the observations and substantiate the importance of ocean-atmosphere feedbacks involving the oceanic

mesoscale.

Extending SCOAR to the tropical Atlantic TIWs shows that air-sea coupling damps the eddy kinetic energy of the waves. TIW-induced wind stress is negatively correlated with the TIW-induced ocean surface current, and this slows down the TIW-currents.

These mesoscale oceanic and atmospheric features alter the large-scale climate variability in the tropical Atlantic. Resolving mesoscale eddies in the ocean leads a cooler equatorial cold tongue and coastal upwelling region. This results in more realistic coastal SST and precipitation. Furthermore, it is shown that synoptic-scale atmospheric African easterly waves capture stronger low-level convergence and convection, only in the higher atmospheric resolution. This triggers heavy precipitation events on the synoptic-scale, which explains a considerable fraction of the total variability. As a result, the simulation of mean rainfall in the Inter-Tropical Convergence Zone (ITCZ) and its seasonality is much improved. This suggests that capturing these transient oceanic mesoscale features and the synoptic-scale atmospheric disturbances is a key ingredient for improving the simulation of the tropical Atlantic SST and ITCZ.

Chapter 1

Introduction

Global coupled general circulation models (CGCMs) allow combined interactions of the large-scale circulation of the ocean and the atmosphere and provide us with important understanding about the inherent coupled processes of the large-scale climate system. CGCMs are used for making predictions of future climate variability on seasonal, decadal and centennial timescales. With rapid advances in computing power, CGCMs are becoming increasingly sophisticated and complicated, while steadily increasing in spatial resolution. They now closely approach the scale of previously unresolved and poorly understood phenomena that give rise to key components of climate variability.

However, these coupled climate models do not fully emulate the observations in many regions in the world ocean. The situation is particularly unsettling in the tropical oceans, where the model simulations substantially deviate from the mean and seasonal cycle of the observed climate, exhibiting large climatic biases associated with possibly spurious and poorly represented coupled feedbacks (Davey et al. 2002; Webster et al. 1998; Mechoso et al. 1995).

A possible reason for unsatisfactory results of coupled models in the tropics may be because the mesoscale¹ oceanic and atmospheric fields are not realistically

¹ The term *mesoscale* is used throughout the dissertation to loosely refer to the small-scale features both in the atmosphere and the ocean, whose horizontal scales ranges from few kilometers up to several hundred kilometers, and which are not fully captured in the

represented in models, largely due to the coarseness of the horizontal resolution. Current routine spatial resolution of the CGCMs is on the order of 2° or coarser. For this reason, coupled mesoscale processes remain unresolved and have been previously heavily parameterized. Therefore these processes cannot be fully understood in a coarse resolution global coupled modeling framework.

Recently, high-quality microwave satellite observations have begun to provide ample evidence of ocean-atmosphere interactions occurring in the presence of ocean mesoscale eddies, small-scale coastal mountains, and islands throughout the global ocean. Observational studies (as reviewed in Xie 2004 and Chelton 2004) have reported that on this small scale it is the ocean that forces the atmosphere, generating substantial perturbations in the interacting atmospheric boundary layer. A growing number of studies have begun to add to the long list of examples of this relatively novel aspect of ocean-atmosphere coupled feedbacks over the ocean wherever sharp fronts of SST, small-scale orography and island geometry can influence ocean winds, heat fluxes and rainfall.

Observational studies have suggested that atmospheric perturbations produced by mesoscale ocean-to-atmosphere forcing are large and can supply additional feedbacks on the dynamical properties and the heat balance of the upper ocean (Chelton et al. 2001). Similarly, recent coupled modeling studies suggest that mesoscale oceanic variability, such as that due to the tropical instability waves (TIWs) in the Pacific and the Atlantic Ocean and the oceanic eddy features in the tropical Indian Ocean, contribute significantly to the observed variability of the tropical ocean and thus the predictability of the tropical climate (Jochum and Murtugudde 2005, 2006). These mesoscale oceanic features are

current coarse resolution coupled climate models.

transient and intrinsic to the ocean. However, through mesoscale ocean-atmosphere feedbacks and nonlinear wave processes, they can substantially modulate the atmospheric heat, moisture and momentum fluxes, as well as vertical entrainment, and thus make a net contribution to large-scale variability.

In general, regions with large climate biases in CGCMs are also regions of rich ocean mesoscale activity and vigorous ocean-atmosphere interaction. This perhaps suggests that the common climate biases that we witness in coupled climate models are largely related to the models' inability to represent properly the effects of the oceanic mesoscale eddies and their feedback with the atmosphere (Mechoso et al. 1995).

The improvement of the quality of global atmospheric and oceanic analysis products² and the development of statistical and dynamical downscaling methods motivated my study of these climatically important mesoscale coupled features of the ocean-atmosphere system using a high-resolution *regional* coupled model. By focusing computational resources on spatial resolution in the regional domain of interest and employing additional parameterizations, the regional coupled model can produce additional insight into the air-sea interactions involving mesoscale features of the ocean and the atmosphere.

This is one of the first modeling studies of coupled mesoscale oceanic and atmospheric features using a fully coupled high-resolution regional model. A detailed description of the regional coupled model, developed as a major part of the dissertation, is provided in Chapter 2. Chapter 2 also presents the results of model simulations from three scenarios in the eastern Pacific sector from the tropics to the mid-latitudes: TIWs in

² Best-guess dynamical estimates of the state of the system

the equatorial ocean, oceanic eddies and upwelling fronts in the California Current System region, and gap winds in the Central America. The first two examples reveal that the model reproduces aspects of the observed linear response of the atmospheric boundary layer to the underlying SST changes by the oceanic mesoscale features (Chelton et al. 2001; Chelton et al. 2007). The gap wind study suggests the importance of the interaction between the small-scale orography and the mesoscale atmospheric wind variability (Chelton et al. 2004), which forces the observed oceanic thermocline response in the eastern Pacific warm pool and the region of permanent precipitation deficit within the Inter-Tropical Convergence Zone (ITCZ). This is a good example of a mesoscale coupled feedback that can alter the large-scale climate (Xie et al. 2005).

A detailed understanding of the coupled feedbacks due to TIWs and their impact on the upper ocean is particularly important because of its potential influence on large-scale climate (e.g., Weisberg and Weingartner 1988). The study of TIWs that commences in Chapter 2 is extended in Chapter 3, where it is shown that air-sea coupling involving TIWs damps the eddy kinetic energy of the waves in the tropical Atlantic (TA) Ocean. The TIW-induced perturbation wind stress is negatively correlated with the TIW-induced perturbation ocean surface current, and this slows down the TIW-currents. Furthermore, the TIWs substantially alter wind stress estimates from satellite scatterometers at TIW-frequencies, which strongly suggests the importance of ocean-atmosphere coupling in the presence of the TIWs in the ocean.

In the final two chapters, we investigate how these coupled mesoscale feedbacks can alter the large-scale structure of climate variability of the TA. Chapter 4 focuses on the rectifying effect from the mesoscale features in the ocean to the basin-wide mean climate, using high and low oceanic horizontal resolutions in the coupled model.

Compared to the non-eddy resolving low-resolution case, resolving oceanic mesoscale variability, such as that due to the TIWs near the equator, and the details of the coastal upwelling on the west coast of Africa, leads to a lower SST in those regions. This suggests that the coastal warm bias commonly exhibited in coarse-resolution coupled climate models could be considerably alleviated when resolving oceanic mesoscale variability. The altered meridional SST gradient, in turn, provides a more realistic ITCZ precipitation pattern. This result suggests that the ocean resolution of the coupled climate model should be high enough to resolve the transient oceanic mesoscale features that can significantly modulate the large-scale mean climate of the TA.

In Chapter 5, we focus on synoptic-scale weather disturbances associated with the African easterly waves and their role in maintaining large-scale mean TA ITCZ. A strong low-level convergence in the high shear of the easterly waves can cause local deep convection in the higher atmospheric resolution coupled model. This triggers heavy precipitation events associated with the tropical storms and cyclones, which accounts for a considerable fraction (60-80%) of the total rainfall variability. The climatic importance of better-resolved convergence and convection processes in the easterly waves is that they can lead to a more realistic model precipitation climatology and seasonal cycle in the Atlantic Ocean. This study suggests that capturing these transient waves and the resultant low-level convergence is important for improving the simulation of precipitation in global coupled climate models.

An enhanced understanding of the coupled climate variability discussed in this study suggests a potential for the improved predictability of the regional climate of the TA, where disastrous socioeconomic hardships are often caused in the adjacent land regions due to unpredictable components of climate anomalies. The nations of the

maritime regions in Northeast Brazil and West Africa are heavily populated, primarily depend on agriculture, and are extremely vulnerable to climate anomalies. Hence, the anomalous latitudinal position of the ITCZ can cause prolonged floods or severe droughts with, at times, devastating economic consequences in such regions (Hastenrath and Heller 1977). Dominance of the seasonal cycle in the TA climate (Xie and Carton 2004) suggests that understanding the mean and seasonal variability of the ITCZ and SST is necessary for reliable prediction of interannual rainfall variability. The current study answers a part of the question: mesoscale ocean-atmosphere coupled variability is important for the simulation of mean and seasonal cycle of SST and the ITCZ.

Moreover, TA cyclone activity and the associated extreme precipitation events, which severely affect the eastern U.S. and the Caribbean Sea region, are significantly correlated with the variability of the synoptic-scale easterly waves (Avila and Pasch 1992; Thorncroft and Hodges 2001) and tropical Atlantic SST (Schade and Emanuel 1999; Emanuel 2005). The current study indicates that climate extremes can be substantially modulated by mesoscale ocean-atmosphere coupled variability. The importance of large-scale climatic rectification effects from the mesoscale features suggests that the current global coupled climate prediction models must take into account mesoscale coupled ocean-atmosphere interaction as a major mode of variability, and this will improve the seasonal and interannual regional climate predictability.

Chapter 2

The Scripps Coupled Ocean-Atmosphere Regional (SCOAR) Model, with Applications in the Eastern Pacific Sector

Abstract

A regional coupled ocean-atmosphere model is introduced. It is designed to admit the air-sea feedbacks arising in the presence of an oceanic mesoscale eddy field. It consists of the Regional Ocean Modeling System (ROMS) and the Regional Spectral Model (RSM). Large-scale forcing is provided by NCEP/DOE reanalysis fields, which have physics consistent with the RSM. Coupling allows the sea surface temperature (SST) to influence the stability of the atmospheric boundary layer and, hence, the surface wind stress and heat flux fields. The system is denominated the Scripps Coupled Ocean-Atmosphere Regional (SCOAR) model.

The model is tested in three scenarios in the eastern Pacific Ocean sector: tropical instability waves of the eastern tropical Pacific; mesoscale eddies and fronts of the California Current System; and gap winds of the Central American Coast. Recent observational evidence suggests air-sea interactions involving the oceanic mesoscale in these three regions. Evolving SST fronts are shown to drive an unambiguous response of the atmospheric boundary layer in the coupled model. This results in significant model anomalies of wind stress curl, wind stress divergence, surface heat flux and precipitation that resemble the observations and substantiate the importance of ocean-atmosphere

feedbacks involving the oceanic mesoscale.

2.1 Introduction

Increased interest in ocean-atmosphere interaction on spatial scales associated with the oceanic mesoscale has arisen because of new enhanced views of the global ocean and atmosphere from satellite remote sensing. Two extensive reviews by Chelton et al. (2004) and Xie (2004) describe numerous efforts to understand these observations of mesoscale air-sea coupling processes throughout the world ocean.

The close associations among ocean states (sea surface temperature [SST], currents, and thermocline depth), atmospheric states (surface winds, cloudiness, and rainfall), surface flux components (wind stress, heat flux and fresh-water flux), and geography (orography, coastlines, bathymetry, and islands) on various space and time scales are common features worldwide. Radar scatterometry and microwave imagers now provide daily estimates of wind, SST, and rainfall over 90% of the global ocean with remarkable accuracy (Chelton and Wentz 2005; Wentz and Meissner 2000; Chelton and Freilich 2005). This has stimulated air-sea interaction studies and unveiled various aspects of climatically important air-sea interaction processes. Current large-scale global analyses of the atmosphere and ocean, however, have inadequate resolution to resolve the sharp transitions of SST fronts or realistic coastal mountain ranges. Understanding the mechanisms of air-sea coupling therefore has been limited, especially in such regions.

This new information from satellites has now started to serve as a validation benchmark for the high-resolution global coupled model studies. Sakamoto et al. (2004), for example, used the high-resolution atmosphere-ocean coupled general circulation model run on Japan's Earth Simulator to successfully reproduce the far-reaching

influences of the Hawaiian Islands. This verified the hypothesis by Xie et al. (2001), based on the observations, that disturbances of SST, wind, and cloudiness in the wake of the Hawaiian Islands are caused by island-induced wind stress curl.

Although global coupled models are beginning to increase their resolution to attempt to resolve smaller scale processes, high-resolution regional coupled ocean-atmosphere models, if properly driven by the large-scale circulation, could provide additional advantages in the study of the detailed patterns of air-sea interactions involving oceanic mesoscale eddies, including meanders. By concentrating most of the computational resources in spatial resolution and detailed parameterizations, small-scale processes may be effectively and optimally isolated and studied.

A high-resolution *regional* coupled ocean-atmosphere model has been developed with this approach in mind. The system is denominated the Scripps Coupled Ocean-Atmosphere Regional (SCOAR) model. The goal in this paper is to introduce the model and demonstrate its basic performance capabilities in the eastern Pacific Ocean. The spatial and temporal patterns of air-sea interaction in the model are found to be similar to those observed in three unique regions of the eastern Pacific sector.

Additional efforts are now in progress to test various hypotheses of regional air-sea interactions proposed by numerous investigators. For example, the model is capable of producing more realistic mean features of the tropical Atlantic climate by resolving ocean mesoscale features, such as tropical instability waves (TIWs) and coastal upwelling (Seo et al. 2006). Other key questions to be addressed in this modeling framework include: How do the turbulent fluxes contribute to the evolving SST? How do SST-induced wind stress perturbations affect dynamical stability properties of the ocean? Future work will involve more rigorous and quantitative analysis to carefully compare

with the observations and also render the regional coupled modeling system capable for hindcasting, nowcasting, and forecasting experiments.

In section 2.2, some previous regional coupled modeling studies are summarized. In section 2.3, each component of the SCOAR model is introduced. In section 2.4, three examples of the coupled model simulations are discussed, followed by a summary and discussion in section 2.5.

2.2 Regional coupled modeling background

There have been a growing number of attempts in the past decade to develop regional coupled ocean-atmosphere models with various goals in several parts of the globe. These previous studies are summarized here.

Early progress in building a regional coupled model was a major element within the Baltic Sea Experiment. In that effort, Gustaffason et al. (1998) coupled a high-resolution atmospheric model to a low-resolution ice-ocean model for the purpose of accurate weather forecasting in the Baltic Sea. Hadegorn et al. (2000) coupled the Max Plank Institute (MPI) REgional atmospheric MOdel (REMO) to the 3D Kiel ocean model in the same Baltic area. The model SST improved even without flux correction, although the improvement was limited to summertime because the sea-ice modeling component was incomplete. Schrum et al. (2003) achieved full flux coupling using the same atmospheric model coupled to the 3D Hamburg Ocean Model. They showed that their interactively coupled ocean-atmosphere runs were stable and distinctively better than atmospheric runs with prescribed SST. Döscher et al. (2002) developed a regional coupled ocean-atmosphere-ice model, RCAO, with the aim of simulating regional coupled climate scenarios over northern Europe based on multi-year hindcasts.

More advanced high-resolution coupled model studies using the REMO coupled to a global MPI ocean model are being used to study the effect of air-sea coupling on Indonesian rainfall (Aldrian et al. 2005) and interannual variability of sea-ice extent in the Arctic Ocean and Nordic Seas (Mikolajewicz et al. 2005).

Another motivation for developing regional coupled modeling system is to study the effect of the surface state of the ocean or lakes (e.g., surface waves, surface roughness) on atmospheric circulation. One example of such a study is Powers and Stoelinga (2000). They developed a comprehensive atmosphere-ocean-wave coupled modeling system and performed sensitivity tests on the surface roughness parameterization of the atmospheric model (MM5) for the case of frontal passage over the Lake Erie region. They showed that a marine roughness parameterization that takes into account the wave age from the wave model can significantly improve the calculation of surface wind stress and heat flux.

A high-resolution regional air-sea coupled model including ocean waves is also useful in studying the effect of sea spray, wind-induced mixing, and surface wave fields on simulating the intensity and evolution of hurricanes for both research and operational purposes (Bao et al. 2000; Li and Xue 2002; Bender and Ginis 2000; Perrie et al. 2004; Chen et al. 2006; among many others). A regional coupled model also has been shown to be useful in simulating the east-Asia summer monsoon (Ren and Qian 2005) despite the presence of a cold drift in SST in their model.

A coupled model is also valuable for studying extreme weather events in the Adriatic Sea region. Loglisci et al. (2004) applied their coupled model to studying effect of Bora wind event on the dynamics and thermodynamics in the Adriatic Sea. They found that accurate heat flux from the sea surface needs to be considered for better

representation of air-sea interactions associated with this high wind event and for improved simulations of SSTs in the response. However, their climatological initialization for the ocean model generated systematic errors in SST. More recently, Pullen et al. (2006) established a regional coupled system comprising the Navy Coastal Ocean Model (NCOM) coupled to Coupled Ocean/Atmosphere Mesoscale Prediction System (COAMPS) in the same region. They focused on the coupled effects of fine-resolution SST on air properties, in particular during the course of a Bora wind event. They found that the simulated SST after a Bora event had a stabilizing effect on the atmosphere, thus reducing atmospheric boundary layer mixing and yielding more skillful near-surface winds.

Now regional coupled models are beginning to be used for studying basin-scale climate simulations. Huang et al. (2004) applied a regional coupling strategy in a global coupled ocean-atmosphere GCM, where active air-sea coupling is allowed only in the Atlantic Ocean basin. The study showed that this regional coupling strategy allowed them to isolate the effects of local feedbacks on the resulting mean SST. Xie et al. (2006) constructed the regional ocean-atmosphere coupled system (iROAM) which couples a regional atmospheric model (iRAM) to a basin-scale ocean model in the Pacific, with interactive coupling permitted only in the eastern half of the basin. A major advantage of iROAM is that by affording reasonably high resolution to the model (0.5° in the atmosphere and ocean) compared to most coupled GCMs, it can effectively explore the role of local air-sea feedbacks arising from ocean mesoscale features and land topography while allowing significant internal coupled variability free from the prescribed lateral boundary conditions. It is specifically designed to study processes and reduce biases in the eastern tropical Pacific climate, where many coupled GCMs exhibit common

problems.

As we shall see in the next section, the uniqueness of the SCOAR model compared to many of these coupled models is that it has greater portability, more complete coupling, parallel architecture, state-of-the-art physics, and dynamical consistency with the NCEP reanalysis forcing. The three eastern Pacific examples discussed in section 2.4, together with the Atlantic domain used by Seo et al. (2006), demonstrate that the model can be set up anywhere in the world ocean at any chosen resolution. This portability, together with SCOAR’s flexible coupling processes, ability to run on massively parallel computers, sophisticated physical parameterizations, and realistic large-scale forcing yields a great potential for SCOAR to be applied throughout the world ocean for numerous scientific goals.

The main target of the SCOAR model is to study the fundamental nature of ocean-atmosphere feedbacks on the ocean mesoscale in hindcasts. Hence, the current modeling system does not include any operational forecasting framework or data assimilation components to produce skillful predictions. Nevertheless, the use of the SCOAR model for operational and/or forecasting purposes (Wilkin et al. 2005), including data assimilation (Moore et al. 2004), is part of our long-term plans.

2.3 The SCOAR Model

2.3.1 RSM atmospheric model

The atmospheric component of the coupled model is the Experimental Climate Predictions Center (ECPC) Regional Spectral Model (RSM). The RSM was originally developed by Juang and Kanamitsu (1994) and underwent frequent improvements and updates to the functionality, efficiency and its dynamics and physics (Juang et al. 1997).

Briefly, the RSM used here is a regional extension to the Global Spectral Model (GSM) used in the National Centers for Environmental Prediction (NCEP)/Department of Energy (DOE) Reanalysis (Kanamitsu et al. 2002a).

The RSM is a primitive equation hydrostatic model on terrain-following sigma coordinates, and the large-scale (low-wavenumber) components of the flow are specified in the model by the NCEP/DOE Reanalysis (RA2) downscaling procedure or by any GSM simulation. Numerous sensitivity studies (e.g., Roads et al. 2003) demonstrate the excellent performance of the RSM, which has a significantly greater freedom to respond to internal dynamics compared with other regional models. The RSM boundary layer physics employs a nonlocal diffusion concept (Hong and Pan 1996). This scheme is strongly coupled to the surface layer physics. In the scheme, the turbulent diffusivity coefficients are calculated from a prescribed profile shape as a function of boundary layer height and scale parameters derived from similarity requirements. Above the mixed layer, a local diffusion approach is applied to account for free atmospheric diffusion. The parameterization for deep convection is based on Relaxed Arakawa-Schubert Scheme (Arakawa and Schubert 1974; Moorthi and Suarez 1992). Further details about the model physics can be found in Kanamitsu et al. (2002b).

2.3.2 ROMS ocean model

The oceanic part of the coupled model is the Regional Ocean Modeling System (ROMS). The ROMS solves the incompressible and hydrostatic primitive equations with a free surface on horizontal curvilinear coordinates, and utilizes stretched generalized sigma coordinates in order to enhance vertical resolution near the sea surface and bathymetry (Haidvogel et al. 2000; Shchepetkin and McWilliams 2005). A radiation

method is used along the open boundaries in order to allow for stable, long-term integrations, together with a flow-adaptive nudging term for relaxation toward the prescribed lateral boundary conditions. That is, the nudging is stronger (timescale of 1 day) if the flow is inward and weaker (timescale of 1 year) for outflow (Marchesiello et al. 2001). Implicit diffusivity associated with 3rd-order upstream horizontal advection is used in the lateral plane as opposed to explicit diffusivity. Mixed layer dynamics are parameterized using a KPP scheme (Large et al. 1994), with vertical mixing coefficient of $10^{-5} \text{ m}^2 \text{ s}^{-1}$ (Shchepetkin and McWilliams 2005). In all three examples in section 2.4, 20 vertical sigma layers are used, with approximately ten layers in the upper 100 m in the open ocean.

The lateral boundary conditions (BC) that force ROMS are provided either from the ocean analysis from the Estimating the Circulations and the Climate of the Ocean project, or from climatological mean temperature and salinity (Levitus 1994a,b). The latter is more appropriate for studying an equilibrium structure of ocean currents (e.g., Marchesiello et al. 2003; Di Lorenzo 2003; and Di Lorenzo et al. 2005), while the former is preferred for retrospective simulations.

2.3.3 Flux-SST Coupler

In order to build a coupled modeling system, a flux-SST coupler that bridges the atmospheric model (RSM) and ocean model (ROMS) needed to be constructed (Figure 2.1). The coupler currently works in a sequential fashion; the RSM and ROMS take turns integrating while exchanging forcing. The interacting boundary layer between RSM and ROMS is based on either RSM's boundary layer physics package, or the bulk formula that is implemented in ROMS. The former calculates forcing fields necessary to drive

ROMS based on the non-local boundary layer scheme described in Section 2.3.1. The latter computes surface fluxes of momentum, sensible heat, and latent heat from near-surface meteorological variables based on Fairall et al. (1996), adapted from the COARE (Coupled Ocean-Atmosphere Response Experiment) algorithm. For all model applications in section 2.4, a bulk parameterization is used at the air-sea interface. ROMS then forces the RSM at the lower boundary by providing SST. Various coupling intervals can be specified in the coupler (3, 24, or 120 hours, and so on), depending on the interaction timescales of interest. In each experiment discussed below, 24 hr coupling is used.

Both atmospheric and ocean models conventionally assume that atmospheric wind stress imposed on the sea surface is a function of atmospheric wind only. This is often justified due to the fact that ocean current speed is typically small compared to the wind speed by order of magnitude. The corresponding conventional parameterization for wind stress in that case is $\tau = \rho C_d |U_a| U_a$, where ρ is air density and C_d is drag constant, and U_a is wind at 10 m heights. However, the importance of surface current in the estimation of surface wind stress (Bye 1986) has been noted in several observational studies (e.g., Kelly et al. 2001; Cornillon and Park 2001; Park et al. 2006) using the QuikSCAT scatterometer, which measures wind velocity relative to the ocean surface velocity. Furthermore, Chelton et al. (2004) showed that narrow and intense ocean currents such as Gulf Stream and Kuroshio exert a strong influence on wind stress curl fields (cf. Behringer et al. (1979) who showed that SST in these regions strongly influences wind stress curl).

Wind stress in SCOAR is therefore calculated by taking into account the relative motion of wind and ocean current using $\tau = \rho C_d |U_a - U_o| (U_a - U_o)$, where U_o denotes

ocean current speed. The importance of this parameterization is supported by the recent study of Luo et al. (2005), who showed that allowing momentum exchange between the surface ocean currents and wind in their coupled GCM could effectively reduce the familiar cold SST bias in the equatorial ocean. Dawe and Thompson (2006) reported a similar result. Duhaut and Straub (2006) further demonstrated with a scaling argument and a simple modeling study that the perturbation to the wind stress due to ocean currents could lead to substantial changes in the curl of wind stress. This is because the spatial scale associated with ocean currents is much smaller than that of wind speed. It should also be noted that we assume the effect of surface gravity waves on the sea state is negligible.

Since the grids of the atmosphere and ocean models are generally different, a simple linear interpolation is used to map the SST and ocean currents to the atmospheric physical-space grid and the resultant fluxes to the ocean grid. Care must be taken in choosing the land-sea mask near the coasts because the atmospheric model is spectral and Gibbs phenomena can result in unphysical structures in the surface flux forcing fields over the oceanic grid points adjacent to the coast. In each example domain to be discussed next, the land-sea mask was qualitatively optimized to reduce this effect of the mismatch between spectral atmospheric and physical space oceanic models.

2.4 Examples of SCOAR model simulations

Three different model domains are examined to test of the SCOAR model performance and capabilities. These include the Eastern Tropical Pacific (ETP), the California Current System (CCS), and the Central American Coast (CAC). The ETP contains TIWs, the CCS provides examples of midlatitude mesoscale eddy feedbacks,

and the CAC allows gap winds to drive ocean mesoscale structures. Table 2.1 summarizes the resolution used in these domains, and Figure 2.2 shows the model bathymetry and orography for each case. In each case, the ocean model was first spun-up using climatological atmospheric forcing for approximately eight years, followed by one to two years of coupled model spin-up with realistic forcing that precede the experiments described next.

2.4.1 TIWs in the ETP

2.4.1.1 Background

In the eastern tropical Pacific, SST fronts associated with the permanent cold tongue are perturbed by TIWs (Figure 2.3c). They are most clearly observed from satellite measurements as wavelike oscillations of SST (Legeckis 1977; Legeckis et al. 1983; Wentz et al. 2000). These SST undulations in the Pacific are observed to have horizontal wavelengths of 1000-2000 km and periods of 20-30 days, propagating westward at $\sim 0.5 \text{ m s}^{-1}$ (Qiao and Weisberg 1998). Observations and numerical studies have shown that TIWs are generated by instability of the various components of the equatorial current/countercurrent system (e.g., Philander 1976, 1978; Cox 1980; Hansen and Paul 1984; Yu et al. 1995). They are an important element in heat budget in the equatorial cold tongue through eddy heat transport and atmospheric heat flux (Hansen and Paul 1984; Baturin and Niller 1997; Jochum and Murtugudde 2006).

Recent studies using high-resolution satellite data highlight the vigorous air-sea coupling processes associated with the undulating SSTs generated by TIWs. Deser et al. (1993) noted the excellent correlation between SST and stratocumulus cloudiness, suggestive of SST modulation of the atmospheric boundary layer (ABL) moisture

content. Hashizume et al. (2002) showed that SST-induced wind changes in the ABL are due to stability changes, as hypothesized earlier by Sweet et al. (1981), Wallace et al. (1989), and Hayes et al. (1989). Chelton et al. (2001) argued that TIWs further affect the wind stress curl and divergence depending on the alignment of the direction of wind stress and SST gradient. The goal of the next section is to describe how the SCOAR model captures TIW behavior and reproduces the observed response of the atmosphere to the undulating SST.

2.4.1.2 Results

As an initial test of the coupled model, a simulation was executed in the ETP domain for five years from 1999 to 2003 with RA2 forcing. Figure 2.3 illustrates the large-scale characteristics of the wind stress and its relationship to the SST fields during a typical TIW season simulated from the model and the observations. The simulated SST and wind stress are strikingly comparable with the observations, exhibiting a pronounced equatorial cold tongue and SST fronts, cusp-shaped SST fluctuations due to TIWs, and associated anticyclonic oceanic eddies. The wind stress magnitudes increase by a factor of 2 or 3 over the regions east of the cold cusps. Discrepancies in the details between modeled and observed TIWs are due to them being a result of an internal instability of the ocean rather than being deterministically forced.

The undulating SST patterns are associated with perturbations of the wind stress field (Figures 2.3b and 2.4a). The wind stress perturbations occur in phase with SST, with stronger (weaker) wind stress over warm (cold) SST. The effect of SST on the wind stress derivatives, however, depends on the alignment of the direction of wind stress and SST-gradient vector (Chelton et al. 2001). Figure 2.4a,b shows that when the winds blow

parallel to the SST gradient vectors (i.e., perpendicular to the isotherms), the positive maximum divergence occurs where the SST gradients are steepest. On the other hand, Figure 2.4a,c shows pronounced positive wind stress curl closely following the SST waves where winds blow parallel to the isotherms. Kessler et al. (2003) found that inclusion of the these narrow strips of positive wind stress curl in the forcing of the Sverdrup flow substantially improved its match to the observed zonal current system. This suggests the importance of local air-sea interactions on the regional ocean circulation. It is encouraging that the SCOAR model produces perturbation wind stress curl patterns quantitatively comparable to those of QuikSCAT via local air-sea interactions (compare Figure 2.4c with Figure 4e in Chelton et al. 2001).

The coupling of wind and SST displays a coherent spatial and temporal variability. Figures 2.5 and 2.6 show time-longitude diagrams of SST and wind stress north (1°N) and south (4°S) of the cold tongue during the cold season (June-December) of 1999. SST propagates westward in time both north and south of the cold tongue. The phase speed of SST north of the cold tongue is approximately 0.6 m s^{-1} , with maximum SST anomaly exceeding 2°C . It should also be noted that the model visibly reproduces the Southern Hemisphere signature of the TIWs, which is an underappreciated characteristic of TIWs (Chelton et al. 2000c; Hashizume et al. 2001) perhaps due to limited data coverage of the observations in the tropics. Consistent with Chelton et al. (2000c, 2001), the TIWs in the south are less well defined and exhibit faster propagation compared to the north. Figures 2.5a and 2.6a show nearly in-phase propagation between SST and wind stress magnitude, again indicating the tight coupling between SST and the resultant surface wind stress.

The TIW-induced SST anomalies clearly perturb the divergence and curl of the

wind stress fields in the atmosphere. Figures 2.5c and 2.6c (2.5d and 2.6d) show the relation between the perturbation wind stress divergence (curl) and downwind (crosswind) SST gradient, similar to the figures from Chelton et al. (2001). Downwind and crosswind SST gradient are computed respectively from $\nabla T \cdot \hat{\tau} = |\nabla T| \cos \theta$ and $\nabla T \times \hat{\tau} \cdot \hat{k} = |\nabla T| \sin \theta$, where T is SST, $\hat{\tau}$ is a unit vector in the direction of the wind stress, and θ is the counterclockwise angle from the vector ∇T to $\hat{\tau}$. Model-simulated relations between the perturbation wind stress divergence (curl) and downwind (crosswind) SST gradient appear to be generally consistent with the observations, with positive divergence (curl) co-propagating with positive downwind (crosswind) SST gradient in Figures 2.5c and 2.6c (Figures 2.5d and 2.6d).

The simple positive correlations between SST gradient and the perturbed wind stress derivatives are illustrated more precisely with binned scatter plots in Figure 2.7. Coupling coefficients estimated from the linear fit between the perturbed wind stress divergence (curl) and downwind (crosswind) SST gradient in the model are 1.5 (0.9), comparable to the values computed from observations by Chelton (2005) over a similar region.

Consistent with the previous observations, the wind stress curl response to the SST gradient is smaller than that of the divergence. Chelton et al. (2001) suggest that the weaker response in wind stress curl can be explained by ocean surface currents that are in the direction of wind stress near the region of maximum crosswind SST gradient. Surface currents in this region reach nearly 1 m s^{-1} (Figure 2.3a) and are in the same direction as near-surface winds ($\sim 4 \text{ m s}^{-1}$, not shown).

We performed a simple sensitivity test to examine the contribution of ocean

surface currents to the wind stress fields. Identical atmospheric forcing during the cold season (July to December) of the year of 1999 from SCOAR was prescribed in two forced ROMS runs, with the ocean current effect on stress included in one, but not in the other. This sensitivity test revealed that the strength of coupling of wind stress curl to crosswind SST gradient is reduced by roughly 25% when the ocean current effect is allowed, while coupling of divergence to downwind SST gradient remains nearly constant (not shown). This reduction accounts for a large part of the 40% weaker response in curl than in divergence seen in Figure 2.7. The remaining difference may be attributable to the different adjustment time-scales for atmospheric flow along or across an SST front, as discussed in Chelton et al. (2001).

Latent and sensible heat fluxes associated with the TIWs are affected both by SST directly, by altering the stability of the ABL, and indirectly, by the influence of SST on the wind speed variations (Thum et al. 2002). Since wind stress and SST are in phase, the latent heat flux and SST are out of phase (Figure 2.5b, Figure 2.6b, and Figure 2.8a). Increased winds over the warm water on the eastern sides of the cold cusps enhance the evaporative cooling at the sea surface, and thus decrease SST. Sensible heat flux is also out of phase with SST, resulting in sensible cooling of warm water with a smaller magnitude than latent heat flux (Figure 2.8c).

The qualitative description of the relation between SST and surface turbulent heat flux is in agreement with the previous study by Zhang and McPhaden (1995). They found that, on TIW-related timescales in the eastern Pacific cold tongue, SST variations are important in forcing latent heat flux variations, implicating an instantaneous atmospheric response to SST. The simulated latent heat flux anomaly from the SCOAR model is about $34 \text{ W m}^{-2} [1^\circ \text{ K SST}]^{-1}$ based on the linear-fitted line of binned scatters (Figure

2.8b), somewhat lower than the observed estimates of 40 W m^{-2} by Thum et al. (2002) and $50 \text{ W m}^{-2} [1^\circ \text{ K SST}]^{-1}$ by Zhang and McPhaden (1995). According to the simple calculation by Thum et al. (2002), this anomaly in latent heat flux would produce 0.5°C cooling of warm water, unambiguously indicating a negative feedback on the SST. Furthermore, Deser et al. (1993) found the increased low-level cloudiness over warm SST on TIW scales, hence reducing solar insolation reaching the sea surface. The resultant impact is to cool warm water at roughly $0.6^\circ\text{C} [\text{month}]^{-1}$, again indicating a negative feedback. Therefore the surface heat flux response to the evolving SST would be to suppress the development of SST anomalies by TIWs (a negative feedback), as discussed by numerous investigators (e.g., Liu et al. 2000; Chelton et al. 2001; Thum et al. 2002; Xie et al. 2004).

The vertical stratification of the upper ocean and lower atmosphere associated with TIWs is presented in Figure 2.9a,c for a longitudinal transect of the model. In the upper ocean, sharp patches of cold water periodically reach the surface roughly every 11° in longitude. The alternating occurrence of cold and warm water implies anticyclonic ocean eddies as seen in the map of SST in Figure 2.3a as vectors of surface current. The simulation also reveals the enhanced stratification of the upper ocean below the eastern part of the anticyclonic eddies as indicated by the steeper thermocline (Figure 2.9d).

In the atmosphere, waves of temperature with similar wavelengths as TIWs are found below the model mixed layer ($\sim 400 \text{ m}$), suggesting that SST affects the vertical stratification of the lower atmosphere. Over cold waters stratification is markedly enhanced, decoupling the surface mixed layer from the flow aloft. This reduces the turbulent mixing of momentum (Wallace et al. 1989), thus decreasing winds near the surface and increasing winds aloft (Figure 2.9b). In particular, the increase of winds aloft

(above 400 m) over cold water has been barely evident in the observations, perhaps due to the superimposed synoptic variability (e.g., Hashizume et al. 2002). More comprehensive fieldwork during the East Pacific Investigation of Climate (EPIC) 2001 (Cronin et al. 2002; Raymond et al. 2004) showed the stronger zonal and meridional winds over cold water at heights between 400-800 m (de Szoeke et al. 2005; Small et al. 2005). The model studies by de Szoeke and Bretherton (2004) and Small et al. (2003, 2005) also produced similar results. Another important point here is whether SST influences the atmosphere above the atmospheric model boundary layer. If it does, then it would suggest that SST might be more important than previously believed on these spatial and temporal scales in climate modeling (Seo et al. 2006).

2.4.2 Mesoscale eddy feedbacks in the CCS

2.4.2.1 Background

The tight associations between SST and the ABL on the ocean mesoscale are not limited to the tropical ocean, but commonly observed in the subtropics and midlatitude ocean (e.g., Behringer et al. 1979; Nonaka and Xie 2003; Vecchi et al. 2004; O'Neill et al. 2005). As one example, consider the rich mesoscale features of the California Current System (Hickey 1979), which is characterized by seasonal development of equatorward alongshore winds and corresponding coastal upwelling (Allen 1980; Lynn and Simpson 1987). Associated with this coastal upwelling are thin, cold filaments and squirts that extend far offshore (Strub and James 2000).

Chelton et al. (2006, hereafter CSR06) showed that ocean-atmosphere coupling is observed in the CCS region during the summertime where the upwelling fronts are well developed. Based on the analysis of QuikSCAT wind stress along with the newly

available SST data set from the advanced Microwave Scanning Radiometer on the EOS-*Aqua* satellite (AMSR-E) on the monthly times scales, they concluded that SST fronts generated by mesoscale variability and coastal upwelling exert an unambiguous influence on the perturbation of summertime wind stress curl (and divergence). The dynamical effects on the CCS may be far more important than in the equatorial ocean. Haack et al. (2005) also found that positive wind stress curls were closely aligned with the tight SST gradient prescribed in their COAMPS atmospheric model, implicating an important dynamic feedback to ocean. CSR06 suggest that open-ocean Ekman pumping due to this SST-generated wind stress curl is as important as Ekman transport due to alongshore wind forcing in the CCS region (see also Pickett and Paduan 2003).

The observed strong coupling and dynamic feedback strongly suggest that this ocean-to-atmosphere forcing may be substantially underestimated in conventional forced ocean and atmospheric CCS models. Current coastal weather forecast models neglect the mesoscale ocean-to-atmosphere forcing and the subsequent feedbacks. Eddy-resolving regional ocean models forced with the observed high-resolution wind stress will also suffer from consistency problems unless the ocean model reproduces SST fields that quantitatively match observations. Numerical studies with high-resolution ocean-atmosphere coupling will be essential to provide new insights to the dynamics of the CCS region. The goal of the next section is to describe how the SCOAR model captures CCS behavior and reproduces the observed response of the atmosphere to midlatitude mesoscale eddies.

2.4.2.2 Results

As an initial test of the coupled model in the CCS region, a simulation was

executed in for 4 years from 2001 to 2004 with RA2 forcing. The results are analyzed based on monthly mean data to facilitate comparison with the observational estimates by CSR06. It should be noted, however, that the coupling coefficient (defined as the linear relationship between the derivative wind stress fields and the SST gradient) is somewhat sensitive to the subjectively chosen temporal and spatial averaging scales.

Figure 2.10 shows typical summertime statistics of SST and wind stress fields obtained from the model in July 2003. Equatorward wind stress is predominant during the summertime along the coast (Figure 2.10a). Two wind stress maxima ($>0.14 \text{ N m}^{-2}$) are found off Cape Mendocino and Pt. Conception. In association with these wind patterns, the SST distribution is zonally asymmetric, with colder upwelled SSTs near the coast and warmer SST offshore. Figure 2.10b shows that both coastal upwelling filaments and offshore mesoscale eddies generate SST gradients greater than $\sim 5\text{-}6^\circ\text{C}$ over 100 km, in agreement with that inferred from satellites (CSR06; Castelao et al. 2006). The resultant SST fronts reveal a similar impact on the monthly mean wind stress derivatives and surface heat fluxes as found for TIWs. The alignment of the SST gradient vectors to the overlying wind stress directions causes spatially coherent patterns between wind stress divergence and downwind SST gradient (Figure 2.10c) and between wind stress curl and crosswind SST gradient (Figure 2.10d). It is also apparent that the gradient of latent heat flux is almost in phase with the SST gradient. On ocean eddy scales, positive SST and negative latent heat flux (and sensible heat flux, not shown) are spatially in phase, while on larger scales they are not.

The strength of the linear response of monthly mean wind stress curl (divergence) to crosswind (downwind) SST gradient was also evaluated for this region using binned scatter plots in the same region as CSR06 (Figure 2.11a-c). The coupling coefficients

inferred from the linear fits between the respective derivatives are ~ 0.5 for wind stress divergence and downwind SST gradient, and ~ 0.2 for wind stress curl and crosswind SST gradient. This coupling strength is weaker by a factor of about 5 for divergence and about 10 for curl than that inferred from observations by CSR06, in contrast to the TIW region where the coupled model produced comparable slopes.

The reason for the smaller coupling coefficients in the model may be that spatial patterns of seasonal mean wind stress and SST are somewhat different from the observations, with the summer wind stress maximum and CCS SST front located roughly 200 km further offshore than observed (not shown). The inconsistency may be partly due to the use of climatological lateral boundary conditions for the ocean. Additionally, the coupled model does not implement data assimilation in the atmospheric component as some other regional atmospheric models do (see Perlin et al. 2004), resulting in a biased mean state and different distributions for the variance fields. For example, the bottom panel of Figure 2.11 shows binned scatter plots over a region that has variance levels more comparable to those in the region defined by CSR06 from observations. The coupling strength in this region is larger than found in the upper panel, although still much weaker than observed.

Midlatitude air-sea coupling at oceanic frontal scales in this eastern boundary current region also may not be adequately captured by this model for several other reasons. Stronger synoptic weather variability, smaller scales of SST fronts, and interactions involving the coastline and coastal orography could obscure the relevant coupling signals in this region compared to the resounding signals found in the tropics. However, Figure 2.10 and Figure 2.11 clearly reveal that the SCOAR model generates coupling signals in the CCS region qualitatively comparable to the observations, even

with climatological biases.

2.4.3 Gap Winds in the CAC

2.4.3.1 Background

The high-elevation mountains of the Sierra Madres along the central American cordillera block low-level winds blowing from the Gulf of Mexico and the Caribbean Sea toward the Pacific Ocean except through three low-elevation gaps in the Isthmus of Tehuantepec, in the Nicaragua lake district, and at Panama (Figure 2.2c). Orographically induced low-level wind jets through these narrow mountain gaps are strongest during the boreal winter, reaching $10\text{-}20 \text{ m s}^{-1}$ with the frequent gusts of 60 m s^{-1} (Stumpf 1975), and extending at least 500 km offshore into the Pacific Ocean (Roden 1961). The high-wind gap flows exert a strong influence on the mean geostrophic circulations and dynamics of the regional ocean, and thus are an imperative climatic element of the eastern Pacific Ocean, establishing a distinctively different climate regime in the eastern Pacific than the central and western Pacific (Kessler 2002).

The gap winds are historically of great interest. Hurd (1929a,b) and Parmenter (1970) both observed arched squall lines and the formation of dense fog associated with the northerly wind of the Tehuantepec. Overland and Walter (1981) noted that these winds are driven by the along-gap pressure gradient. Numerous studies have investigated the structure and evolution of the gap winds (e.g., Schultz et al. 1997; Steenburgh et al. 1998; Chelton et al. 2000a,b), while others have examined their impacts on the regional ocean circulation (McCreary et al. 1989; Kessler 2002), upwelling and formation of stationary or propagating eddies (e.g., Roden 1961; Stumpf 1975; Stumpf and Legeckis 1977; Trasviña et al. 1995; Palacios and Bogard 2005), and the oceanic ecosystem

(Fiedler 1994, 2002).

Recently, Xie et al. (2005) focused on the Papagayo jet, whose zonal orientation and resulting band of Ekman pumping on its southern flank yield far more important influences on the thermocline topography of the ocean than the Tehuantepec jet. In addition to jet-induced Ekman pumping in the wintertime, the positive wind stress curl on the southern flank of the Papagayo jet remains fairly strong throughout the year. This is maintained with the aid of large-scale atmospheric flow as the cross-equatorial southerly wind curves eastward and supplies additional background cyclonic wind shear. It results in a permanent shoaling of the thermocline called the Costa Rica Dome, centered at 9°N and 90°W, where the mean depth of the 20°C isotherm is less than only 30 m (see Figure 2.2 of Kessler 2002). Kessler (2002) noted that a linear Sverdrup balance forced by the enhanced positive Ekman pumping could explain the dynamic topography of the cyclonic Costa Rica Dome. Xie et al. (2005) explained that the zonal orientation of the Papagayo jet is responsible for the thermocline response, as the effect of Ekman pumping is accumulated westward from the coast in the zonal integral of the Sverdrup relation. The meridionally oriented Tehuantepec jet, on the other hand, permits east-west canceling of Ekman forcing in the zonal integral, thus leaving only marginal impact on the dynamic topography in the wintertime.

Xie et al. (2005) subsequently revealed an important ocean-atmosphere feedback process involving the Costa Rica Dome and seasonal precipitation. The isolated cold spot at the sea surface, which is the surface expression of the Costa Rica Dome, leaves a marked impact on atmospheric deep convection in summer by generating a regional rainfall deficit within the inter-tropical convergence zone (ITCZ). The goal of the next section is to examine how well the SCOAR model reproduces the observed mean climate

and ocean-atmosphere coupling processes on seasonal timescales in the CAC region.

2.4.3.2 Results

As a test of the coupled model in the CAC domain, we performed a 5-year (1999–2003) coupled model simulation with RA2 forcing to investigate the air-sea interactions associated with the gap winds (Figure 2.2c; Table 2.1). This 5-year period corresponds to the time period studied by Xie et al. (2005), which facilitates the direct comparison with the observations. Figure 2.12a,c shows the seasonal climatology of wind stress vectors and their magnitudes. Prevailing easterlies are seen on the east coast of Central America and over the Gulf of Mexico. The gap-forced wind jets are well defined in the surface wind stress fields, exhibiting pronounced gap outflows off the coast of the three gaps. Figure 2.12b,d illustrates the Ekman pumping velocity generated by these low-level wind jets, clearly showing that they force upwelling (downwelling) on the left (right) flank of the jets. Seasonal gap winds, and the corresponding curl-induced upwelling and downwelling, become stronger in the wintertime when the gap winds are more frequent.

Xie et al. (2005) suggest that Tehuantepec and Papagayo wind jets and the resultant vorticity forcings remain strong in their summer climatology. The present model displays only a slight hint of these summertime low-level winds, indicating a model deficiency. Nevertheless there is an indication of the patterns of alternating upwelling and downwelling along the coast during summertime within the ITCZ-induced broad band of upwelling (Figure 2.12d).

These low-level wind jets exert a distinctive impact on the underlying SST fields. Figure 2.13a,c show the climatology of model SST, where the distinct minima off the three gaps that intensify in winter are illustrated. These cold regions are a direct response

to mixing by wind gusts and associated Ekman upwelling that shoal the model thermocline (not shown). Comparing with the observations (Xie et al. 2005), in boreal winter the cold tongue off the Gulf of Tehuantepec is too warm while two other ones to the south are too cold. The surface expression of the Costa Rica Dome tends to be exaggerated in the model during both seasons, indicating that the model suffers a significant cold bias in the warm pool region (Figure 2.3a,c).

The SCOAR simulation supports the Xie et al. (2005) hypothesis of the feedback of SST on summertime precipitation by qualitatively reproducing a similar precipitation climatology (Figure 2.13b,d). Over the Costa Rica Dome, SST is colder by 2°C beyond its periphery. The SST colder than the convective threshold suppresses precipitation, producing a region of rainfall deficit within the ITCZ. This “dry hole” in the model is, however, only ~300 km in diameter, which is smaller than the ~500 km pattern apparent in observations.

It is worth noting that gap winds and air-sea interaction are also allowed in the ETP case since it includes the CAC domain, but with only half the horizontal resolution (Table 2.1). Interestingly, the dry hole was not visually evident in the ITCZ in this coarser resolution run (not shown). This result is consistent with the study by Xie et al. (2006), in which a 0.5° resolution coupled model was not able to produce the observed dry hole.

2.5 Summary and discussion

The SCOAR model, which combines two well-known ocean (ROMS) and atmosphere (RSM) models with a flux coupling strategy, was developed to study small-

scale coupled interactions. Its capabilities are demonstrated for three phenomena in three domains of the eastern Pacific Ocean: tropical instability waves in the eastern tropical Pacific, mesoscale eddies in the California Current System, and gap winds along the Central American Coast. These phenomena are modeled here for the first time using high resolution and full coupling, with key aspects of model variables compared favorably with observations.

In the Eastern Tropical Pacific region, the SCOAR model reproduces key features of observed air-sea coupling involving TIWs and cross-equatorial winds. Stability within the ABL changes as the surface winds blow across the front (Wallace et al. 1989). This results in acceleration of surface winds and enhanced turbulent heat flux over warmer SST to the north. The heat flux response yields thermodynamic feedback to the TIWs by enhancing (reducing) evaporative and sensible cooling of warmer (colder) water. This is consistent with numerous studies that suggest that the feedback of turbulent and radiative flux on SST is negative, suppressing the growth of SST by TIWs (e.g., Deser et al. 1993; Thum et al. 2002).

In addition to the negative heat flux feedback from the perturbed atmosphere, TIWs induce a dynamic feedback from the atmosphere by generating narrow bands of strong wind stress curl and divergence along the SST fronts. In idealized experiments, Pezzi et al. (2004) found that active wind stress coupling modified by the underlying SST results in a slight decrease in TIW variability. Additional experiments using SCOAR with and without the effects of thermodynamic and dynamic feedbacks in this region are now in progress to address the role of each type of atmospheric feedback with TIWs.

In the CCS region, a similar linear relationship between derivatives of SST and wind stress was also identified in monthly averaged model outputs. Wind stress curl and

divergence are linearly proportional to the crosswind and downwind SST gradient near the coastal ocean. However, the linear slopes computed from the scatter plots are weaker than observed (Chelton et al. 2007), perhaps due to the discrepancy between the model climatology and observations or to the resolution limitations of the satellite SST data. A closer examination of SST-induced perturbation of wind stress curl and the subsequent impact on the open ocean dynamics is currently underway using SCOAR.

Along the west coast of Central America, coupled feedbacks involving coastal mountains, low-level wind jets, thermocline topography, and precipitation are replicated on seasonal timescales. Despite discrepancies in the intensity of Ekman forcing by wind jets, the extent of the Costa Rica Dome, and the size of the dry hole within the ITCZ, the model reasonably well reproduces the seasonal climatology in this region. Most importantly, the SCOAR model captures the key features of ocean-atmosphere feedback between the surface expression of the Costa Rica Dome and the dry hole in the ITCZ.

These preliminary results motivate further studies of these and other coupled ocean-atmosphere phenomena that occur around the globe. A key modeling strategy will involve comparing simulations in fully coupled, partially coupled, and uncoupled modes. By introducing and adjusting the coupling parameters of the thermodynamic and dynamic interaction of the air and sea, one can address fundamental questions on the role of the ocean-induced atmospheric feedbacks to the ocean anomalies, and the relative importance of the thermodynamic and dynamic feedbacks. Detailed analyses are in progress.

2.6 Acknowledgments

The text of this chapter, in full, is a reproduction of the material as it appears as

Seo, H., A. J. Miller, and J. O. Roads, The Scripps Coupled Ocean-Atmosphere Regional (SCOAR) Model, with Applications in the Eastern Pacific Sector, *Journal of Climate*, **20**, 381-402, 2007. The dissertation author was the primary investigator and author of this paper. The coauthor listed in this publication directed and supervised the research which forms the basis for this chapter.

We gratefully acknowledge funding support from NOAA (NA17RJ1231 through ECPC and CORC), DOE (DE-FG02-04ER63857), ONR (N00014-05-1-0363), NSF (OCE0121332), and NASA (NNH04ZYS008N). The views expressed herein are those of the authors and do not necessarily reflect the views of these agencies. We thank Dr. Masao Kanamitsu, Prof. Emanuele Di Lorenzo, Prof. Raghu Murtugudde, Dr. Markus Jochum, Prof. Shang-Ping Xie, Dr. Guillermo Auad, Dr. Hideki Kanamaru, Dr. Larry O'Neill, and Mr. Akihiko Shimpo for their important discussions. We also thank Prof. Dudley Chelton and two anonymous reviewers for providing extensive comments and suggestions that significantly improved the manuscript.

Table 2.1 Model domain specifications for Eastern Tropical Pacific (ETP), Central American Coast (CAC), and California Current System (CCS). For all experiments, RSM (ROMS) uses 28 (20) vertical layers. The ETC and CAC cases are 5-year simulations from 1999-2003, while the CCS case is 4 years from 2001-2004.

Application	RSM		ROMS	
	Horizontal resolution (km)	Grid size ($N_x \times N_y$)	Horizontal resolution (km)	Grid size ($N_x \times N_y$)
ETP	50	129×86	42	147×88
CCS	16	107×120	7	220×250
CAC	27	129×86	25	138×82

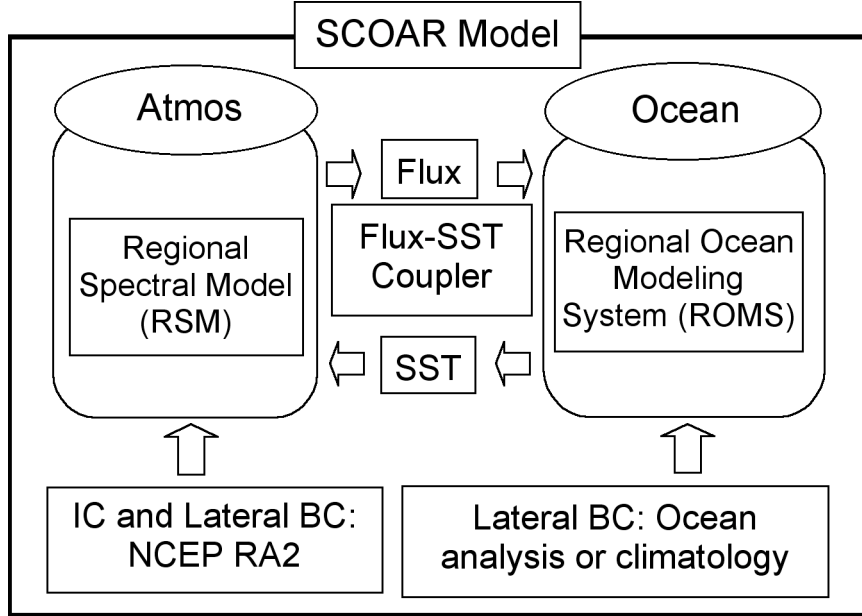


Figure 2.1 Schematic description of the Scripps Coupled Ocean-Atmosphere Regional (SCOAR) model; Initialization and large-scale atmospheric flows specified as low-wavenumber forcing of the RSM are obtained from NCEP/DOE Reanalysis (RA2). Initial and boundary conditions for ROMS are from the ocean analysis from the Estimating the Circulations and the Climate of the Ocean (ECCO) project, or Levitus climatological mean temperature and salinity. The RSM and ROMS are coupled sequentially with typical coupling intervals of 3, 24, or 120 hours.

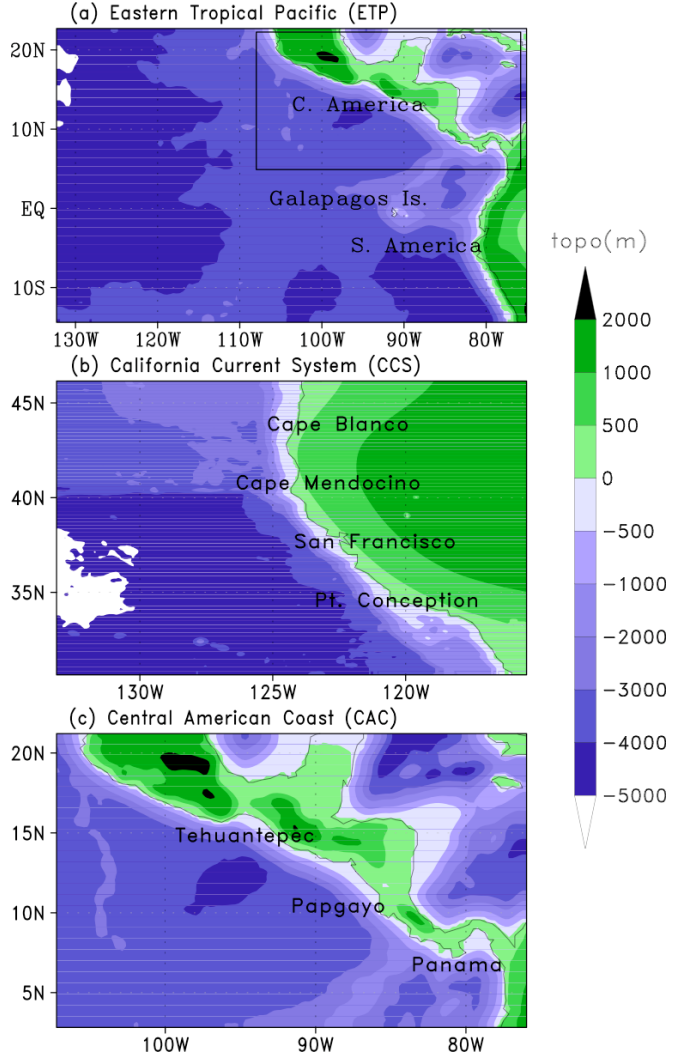


Figure 2.2 Model domain, bathymetry and orography (m) for (a) Eastern Tropical Pacific (ETP), (b) California Current System (CCS), and (c) Central American Coast (CAC). Solid box on (a) represents CAC domain in (c).

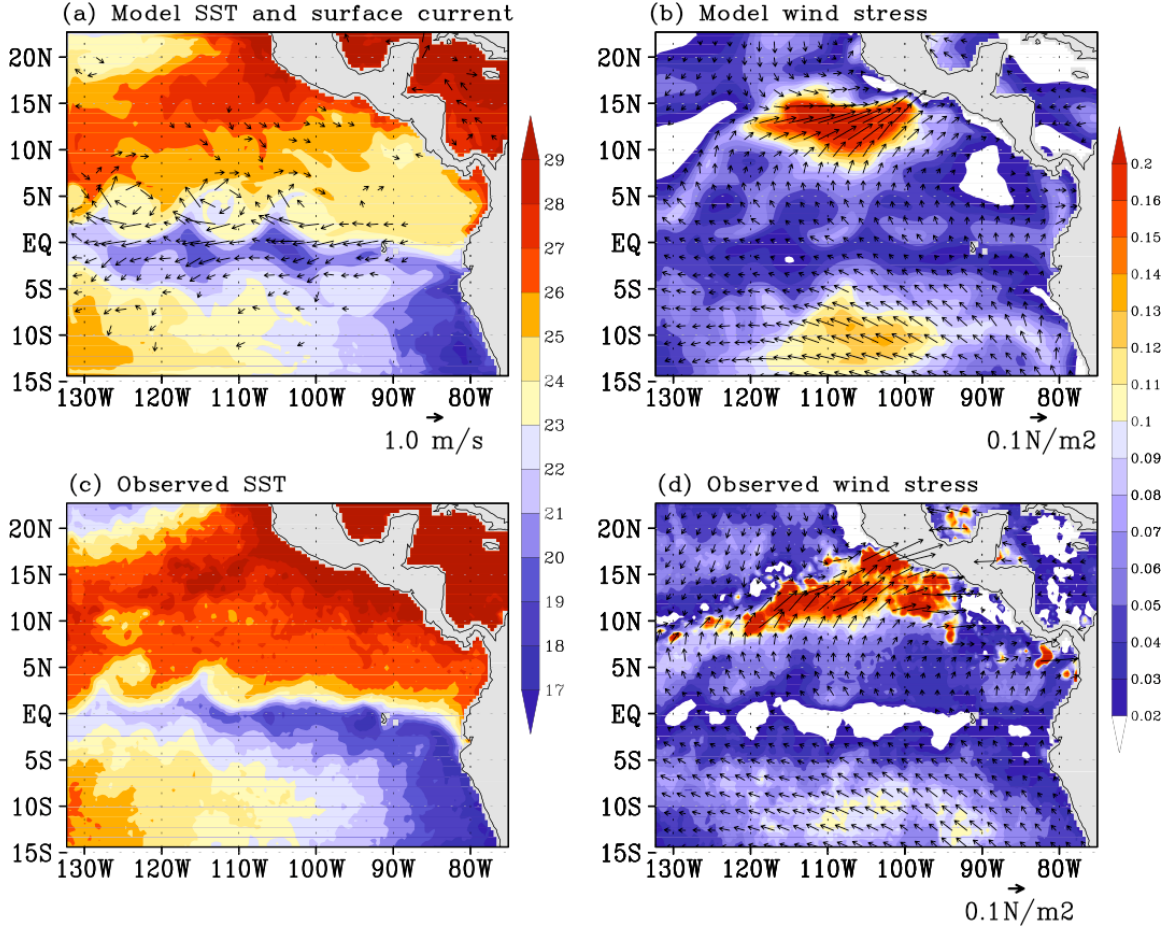


Figure 2.3 Three-day averaged oceanic and atmospheric states centered on September 3, 1999 from (upper panel) the model simulations, and (bottom panel) from the observations. (a) SST ($^{\circ}$ C) and ocean surface currents ($m s^{-1}$), (b) wind stress (WS) vector and magnitude ($N m^{-2}$). (c) SST ($^{\circ}$ C) from TMI, and (d) wind stress vectors and magnitude from the QuikSCAT. Surface current speed less than $0.4 m s^{-1}$ is not plotted in (a). Wind stress magnitude less than $0.02 N m^{-2}$ is not plotted in (b) and (d).

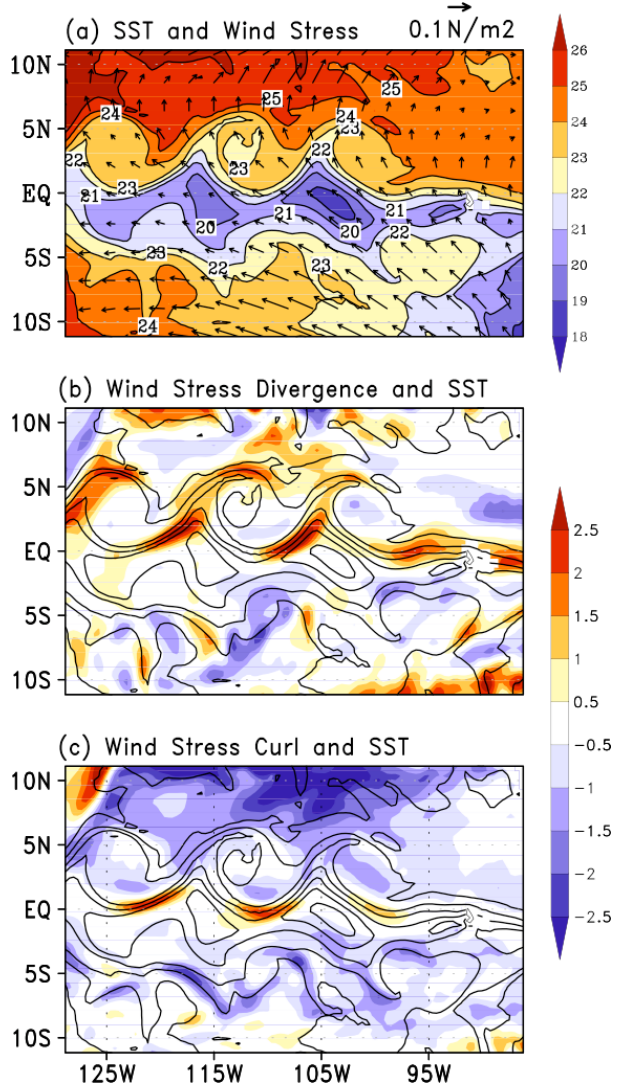


Figure 2.4 Example of the SST and wind-stress spatial relationship simulated by the coupled model (3-day mean centered on September 5, 1999). (a) SST ($^{\circ}\text{C}$) and wind stress vector (N m^{-2}), (b) wind stress divergence ($\text{N m}^{-2} [10^4 \text{ km}]^{-1}$) and SST contours shown in (a), and (c) wind stress curl ($\text{N m}^{-2} [10^4 \text{ km}]^{-1}$) and SST contours shown in (a).

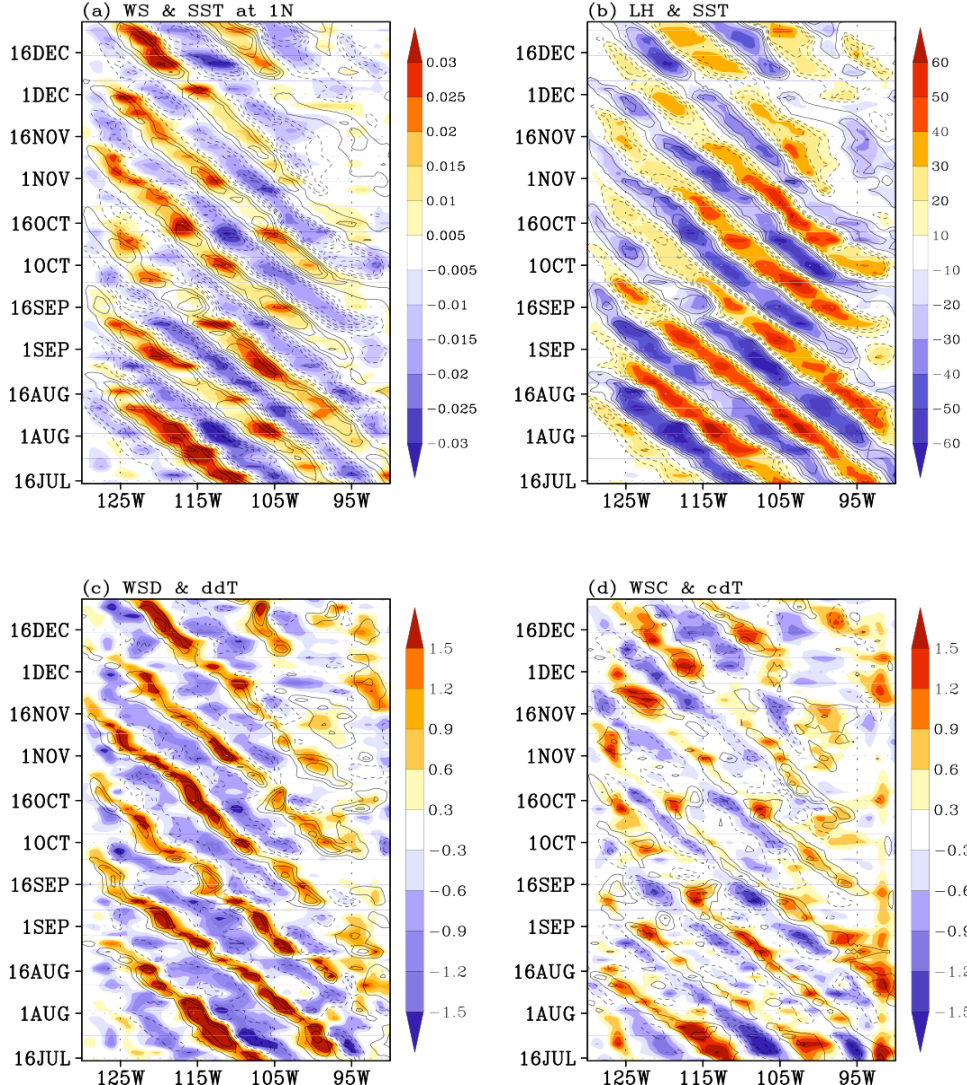


Figure 2.5 Longitude-time plots along 1°N on the north side of the equator of model SST and wind stress fields from July 16 to December 31, 1999: (a) perturbation wind stress (WS) with contours of perturbation SST ($^{\circ}C$), (b) perturbation latent heat flux ($N m^{-2}$) with contours of perturbation SST ($^{\circ}C$), (c) wind stress divergence (WSD , $N m^{-2} [10^4 km]^{-1}$) overlaid with contours of downwind SST gradient (ddT , $^{\circ}C [100 km]^{-1}$), and (d) wind stress curl (WSC , $N m^{-2} [10^4 km]^{-1}$) overlaid with contours of crosswind SST gradient (cdT , $^{\circ}C [100 km]^{-1}$). Contour intervals for SST in (a) and (b) are $0.5^{\circ}C$, and contour intervals for ddT in (c) and cdT in (d) are $0.5^{\circ}C [100 km]^{-1}$. For clarity, contours of zero values are not plotted. Solid (dashed) contours represent positive (negative) values.

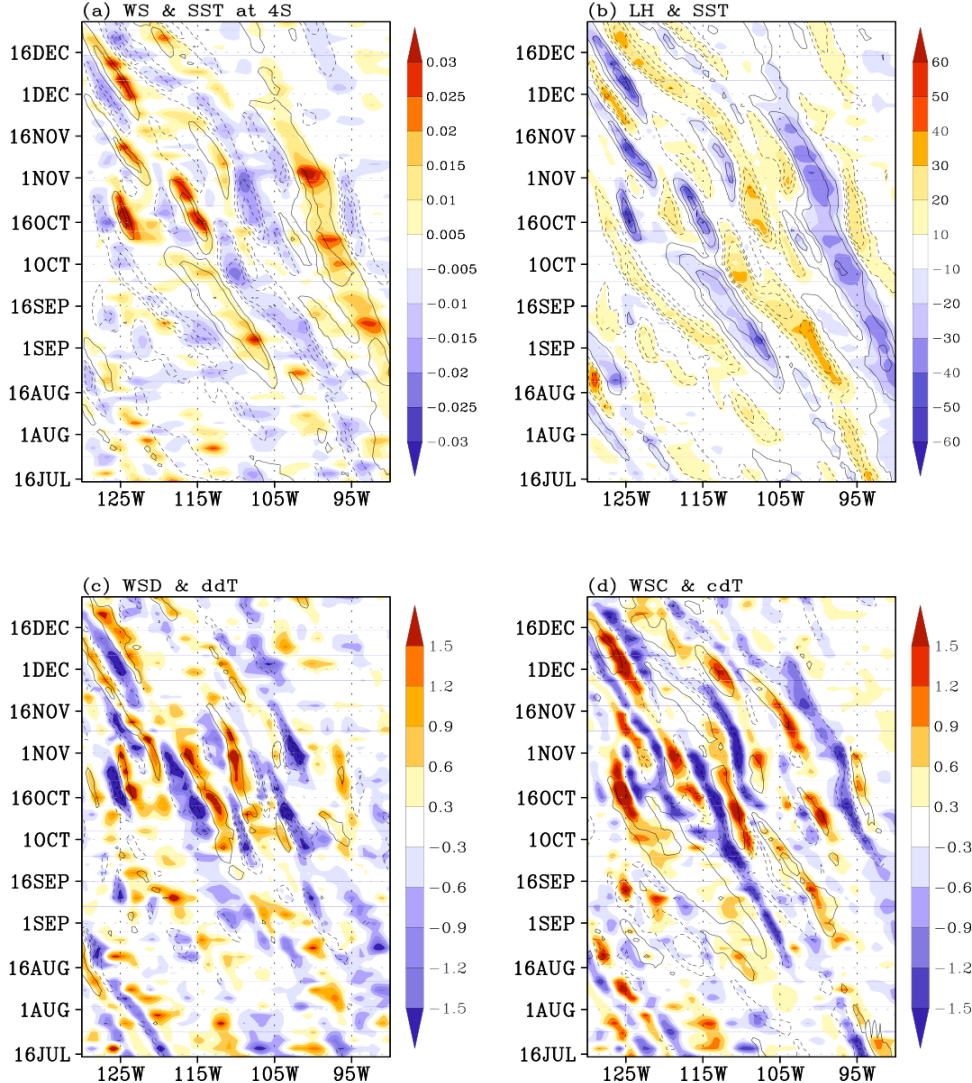


Figure 2.6 The same as Figure 2.5, except along 4°S on the south side of equator.

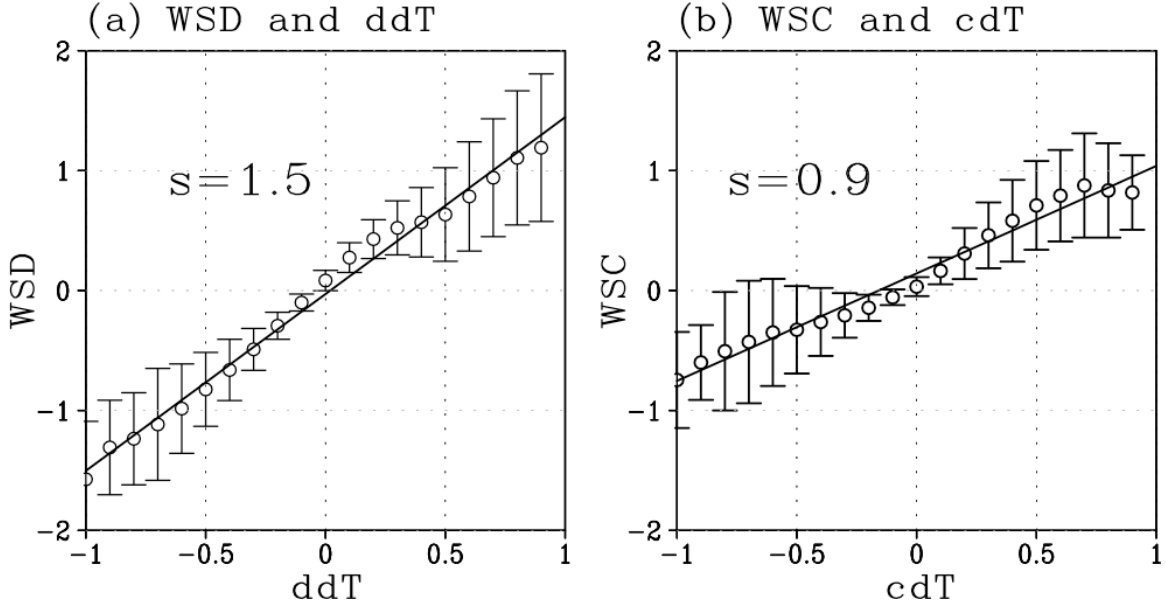


Figure 2.7 Binned scatter plots of (left) the zonally high-pass filtered wind stress divergence (WSD , $N m^{-2} [10^4 km]^{-1}$) and the downwind SST gradient (ddT , $^{\circ}C [100 km]^{-1}$), and (right) wind stress curl (WSC , $N m^{-2} [10^4 km]^{-1}$) and crosswind SST gradient (cdT , $^{\circ}C [100 km]^{-1}$) over $125^{\circ}W-100^{\circ}W$, and $5^{\circ}S-5^{\circ}N$ from cold seasons (July to December) for 5 years (1999-2003). Solid circles in the plot indicate the overall mean values within each bin for the whole period of time, and the error bars represent the ± 1 standard deviations of the scatter. The solid lines through the binned means represent least squares fits of the binned means to the straight lines. The parameter, s , in each plot indicates the slopes of the fitted line (coupling strength). Daily SST at 42 km ROMS grid was smoothed using 4° longitudes by 2° latitudes block running mean. The SST gradient was computed from the resultant smoothed SST by centered differences. The wind stress curl and divergence (and heat flux) were computed from the unsmoothed wind stress at 50 km RSM grid by the same difference method. Then, the derivative SST and wind stress fields were zonally high-pass filtered to reduce the variability with zonal scales longer than 20° longitudes. The binned scatters were computed based on 3-day averaged data of the resultant high-pass filtered fields.

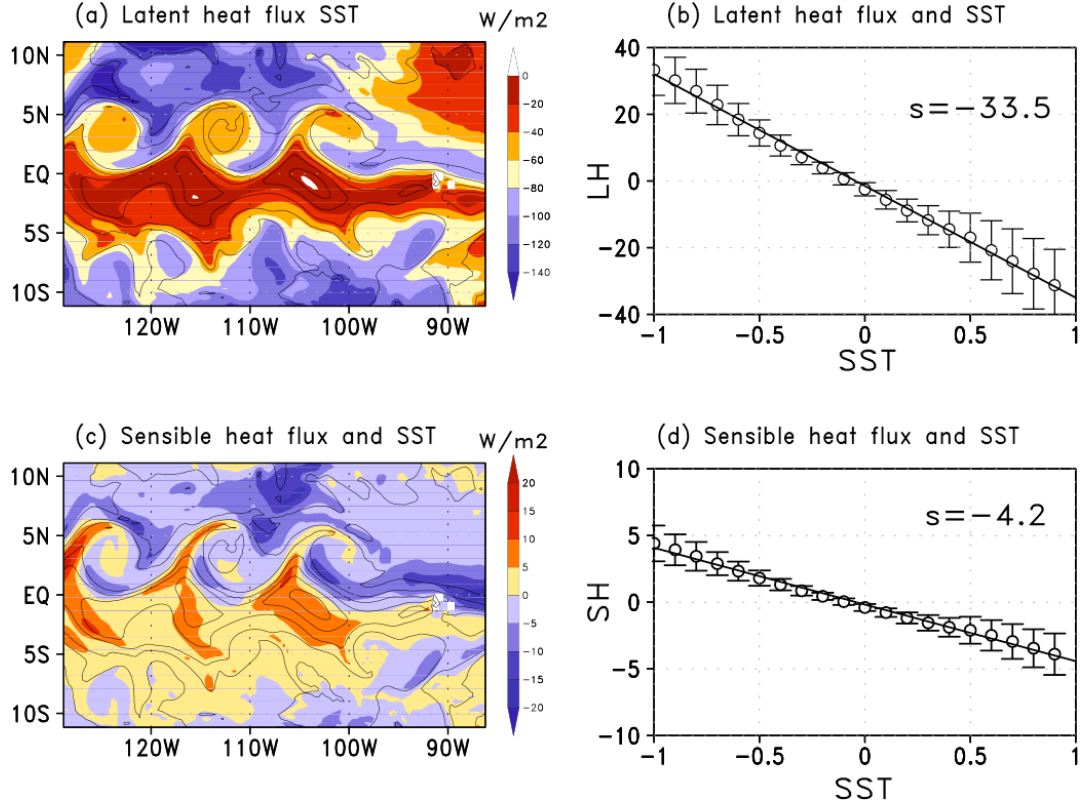


Figure 2.8 (left) Same as Figure 2.4, except (a) latent heat flux (W m^{-2}) overlaid with contours of SST ($^\circ\text{C}$) shown Figure 2.4a, (c) sensible heat flux (W m^{-2}) with contours of SST ($^\circ\text{C}$) shown Figure 2.4a, (right) same as Figure 2.7 except for plots of (b) perturbation latent heat flux (W m^{-2}) and SST ($^\circ\text{C}$) and (d) perturbation sensible heat flux (W m^{-2}) and SST ($^\circ\text{C}$). The convention of sign of heat flux is such that positive flux warms the ocean. SST, and latent and sensible heat flux used in the binned scatter plots were lowpass- and highpass-filtered as described in Figure 2.7.

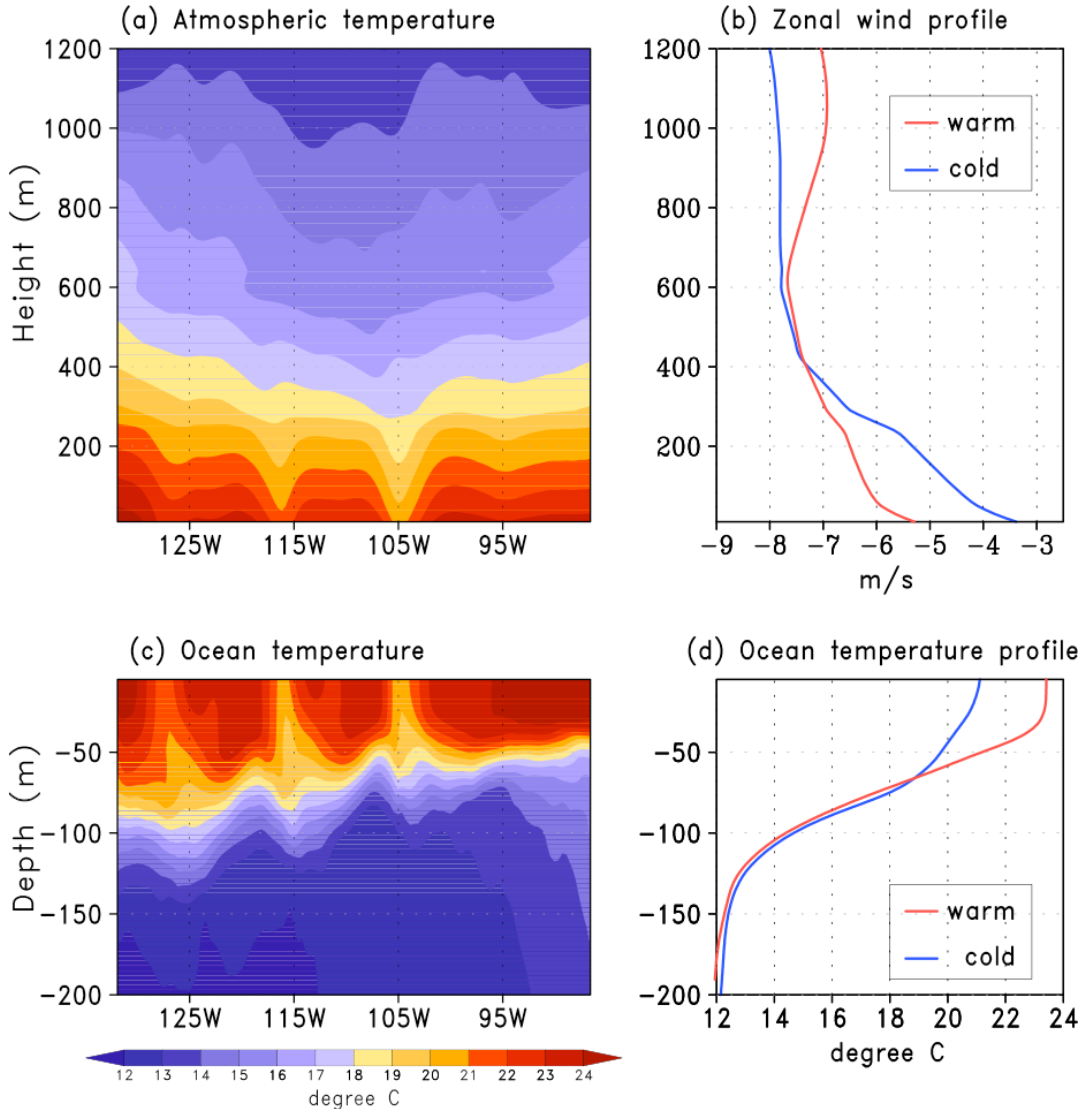


Figure 2.9 (left) Longitude-height (depth) cross-sections of (a) atmospheric temperature ($^{\circ}\text{C}$) and (c) ocean temperature ($^{\circ}\text{C}$) from 2-4 September 1999 averaged from 1°N - 2°N . (right) The composite profiles of (b) zonal wind (m s^{-1}) and (d) vertical ocean temperature ($^{\circ}\text{C}$). Red (blue) lines are mean profiles when zonal deviation of SST is warmer (colder) than 1 standard deviation. There were 17 (15) warm (cold) phases from 2-4 September 1999.

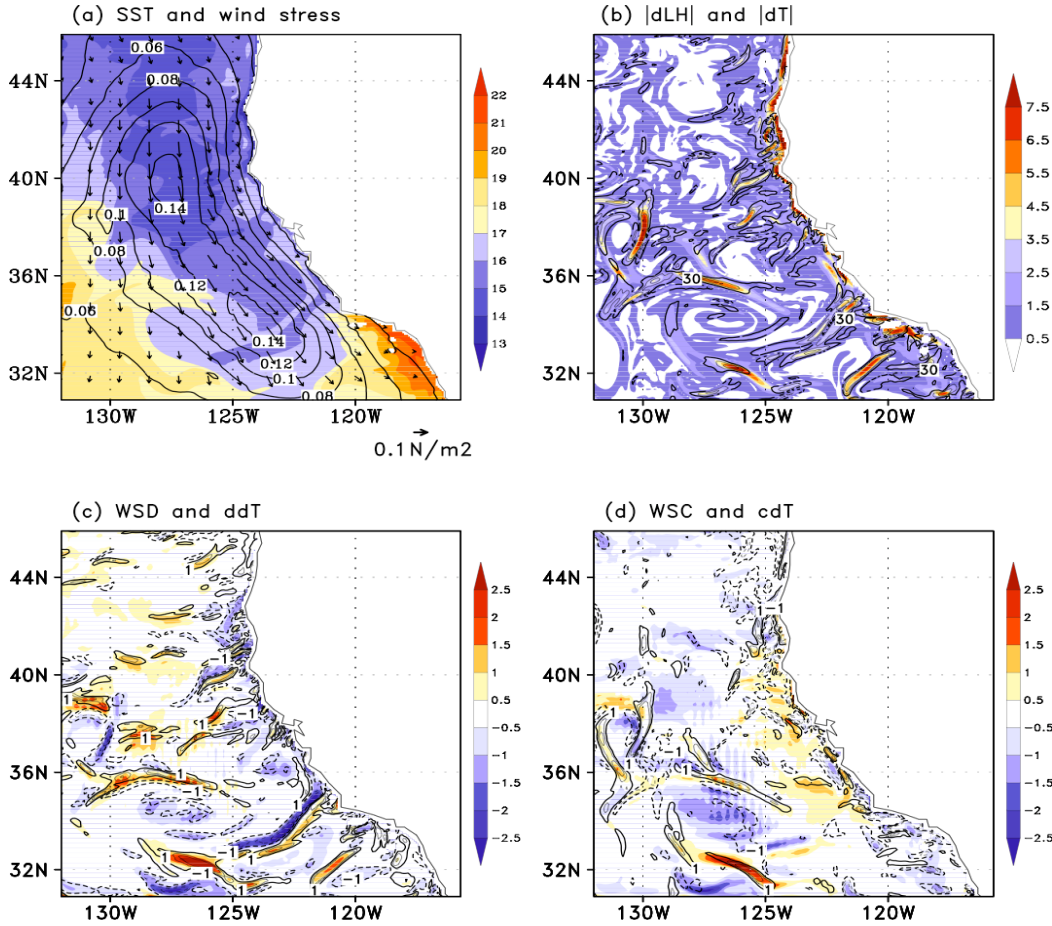


Figure 2.10 Model-derived 30-day average fields of SST and wind stress in July 2003. (a) SST ($^{\circ}\text{C}$) overlaid with vectors of wind stress (WS) and contours of WS magnitude (N m^{-2}), (b) absolute values of latent heat flux gradient ($|dLH|$, $\text{W m}^{-2} [100 \text{ km}]^{-1}$) with contours of SST gradient ($|dT|$, $^{\circ}\text{C} [100 \text{ km}]^{-1}$), (c) anomalous wind stress divergence (WSD , $\text{N m}^{-2} [10^4 \text{ km}]^{-1}$) with contours of downwind SST gradient ($^{\circ}\text{C} [100 \text{ km}]^{-1}$), (d) anomalies of wind stress curl (WSC , $\text{N m}^{-2} [10^4 \text{ km}]^{-1}$) with contours of crosswind SST gradient ($^{\circ}\text{C} [100 \text{ km}]^{-1}$). Contour interval of wind stress magnitudes in (a) is 0.02 N m^{-2} . Contours of $|dLH|$ are every $30 \text{ W m}^{-2} [100 \text{ km}]^{-1}$ (thick contours for $30 \text{ W m}^{-2} [100 \text{ km}]^{-1}$). WSC and WSD are plotted every $1 \text{ N m}^{-2} [10^4 \text{ km}]^{-1}$ (thick contours for $\pm 1 \text{ N m}^{-2} [10^4 \text{ km}]^{-1}$). Summertime averages are removed from wind stress derivatives and the respective components of SST gradient in (c) and (d).

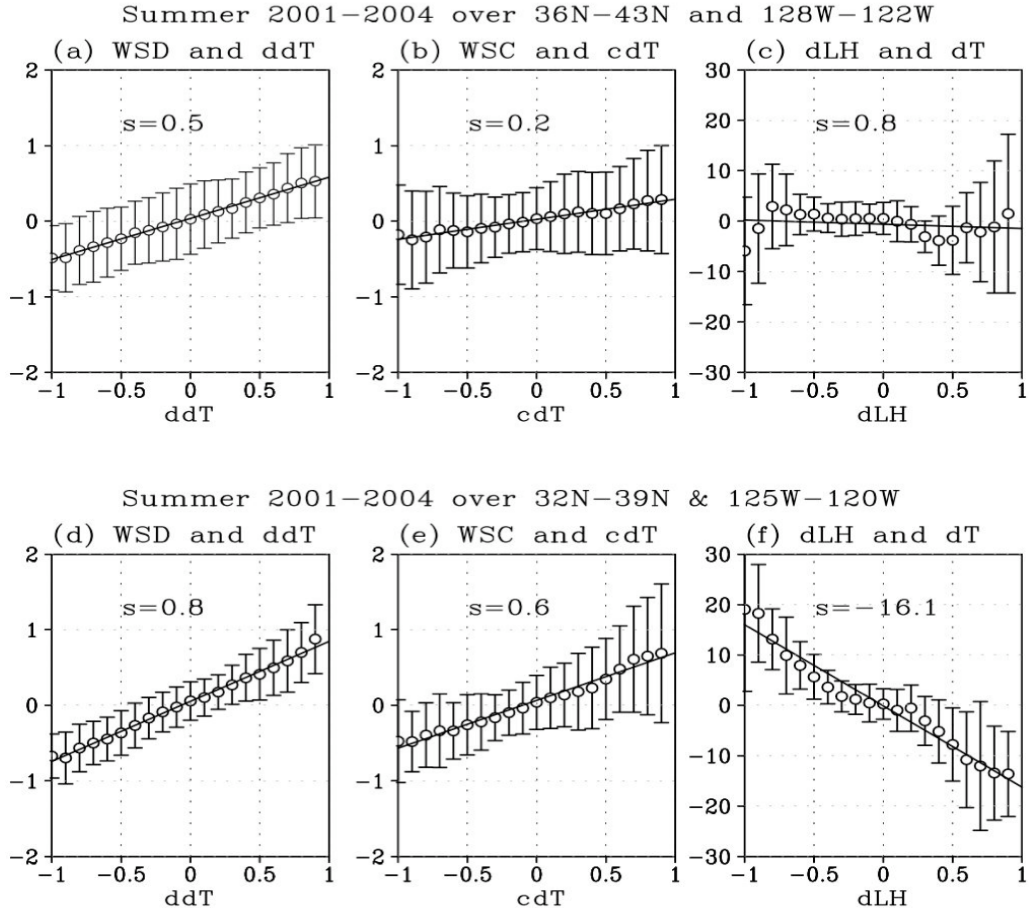


Figure 2.11 Binned scatter plots over California coastal ocean computed from summertime (July–October) monthly-averaged data from 2001 to 2004 over (upper panel) 36°N - 43°N , and 128°W - 122°W as used in Chelton et al. (2006), (lower panel) 32°N - 39°N and 125°W - 120°W . (left) wind stress divergence (WSD , N m^{-2} [10^4 km^{-1}]) and downwind SST gradient (ddT , $^{\circ}\text{C}$ [100 km^{-1}]), (middle) wind stress curl (WSC , N m^{-2} [10^4 km^{-1}]) and crosswind SST gradient (cdT , $^{\circ}\text{C}$ [100 km^{-1}]), and (right) latent heat flux gradient (dLH , W m^{-2} [100 km^{-1}]) and SST gradient (dT , $^{\circ}\text{C}$ [100 km^{-1}]). Daily SST on the 7 km ROMS grid and atmospheric flux on the 16 km RSM grid were monthly averaged and smoothed using 0.5° block averages. The SST gradient was computed from the resultant smoothed SST with centered differences. The derivatives of wind stress and heat flux were computed from the unsmoothed wind. The binned scatters were computed based on monthly averaged data for summertime. Large-scale summertime mean SST and wind stress are subtracted from full fields in left and middle panels.

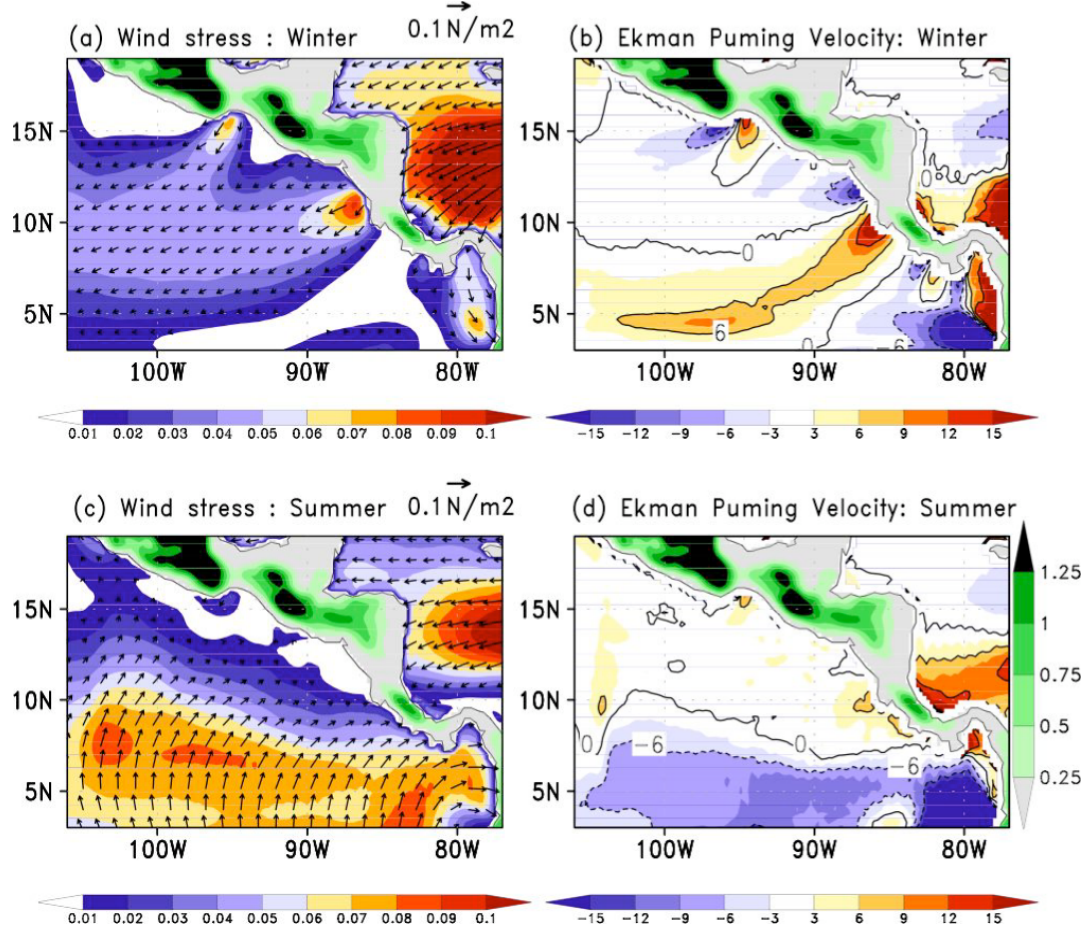


Figure 2.12 (left) Model climatology (1999-2003) of wind stress (WS) vector and magnitude (N m^{-2}) averaged from (a) January to April (winter) and (c) from July to October (summer), (right) Wind-induced Ekman pumping velocity (w_e , 10^{-6} m s^{-1}) exerted by gap winds for (b) winter and (d) summer.

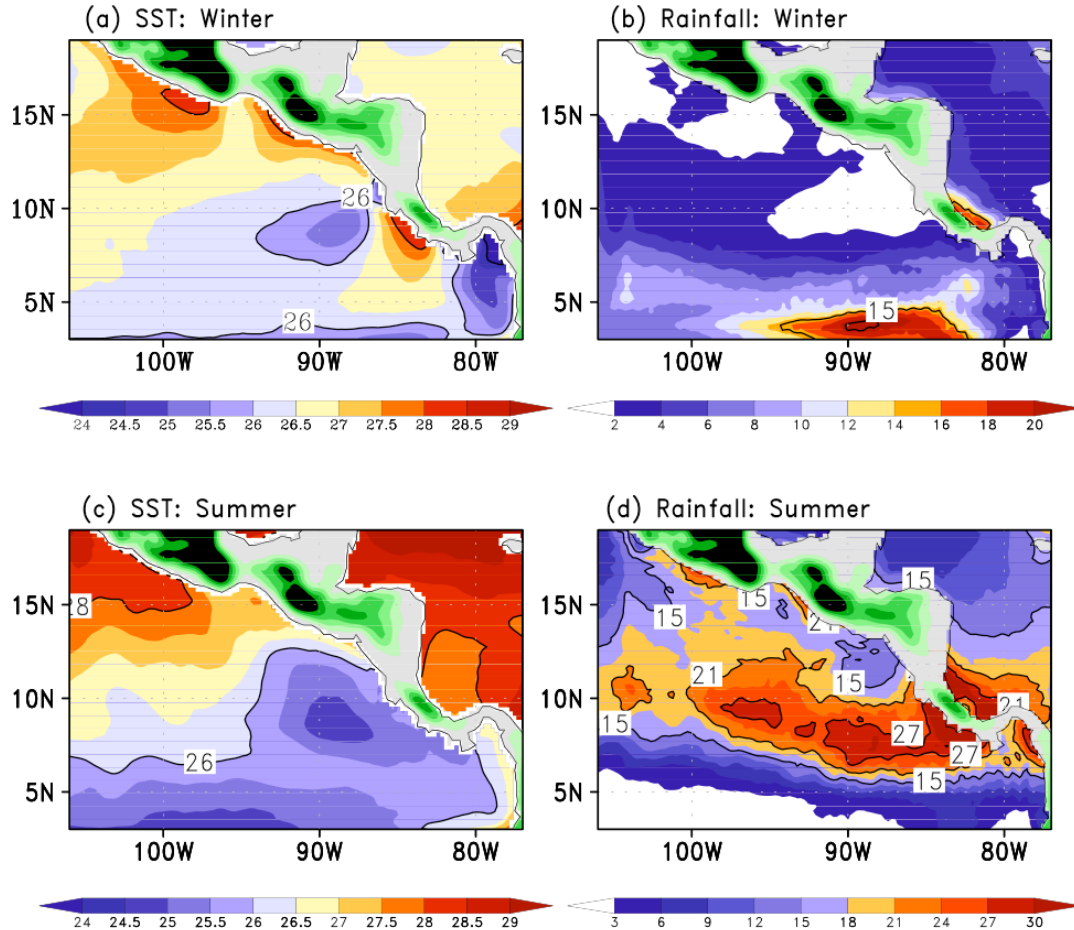


Figure 2.13 Same as Figure 2.12 except for SST ($^{\circ}\text{C}$) for (a) and (c). Corresponding precipitation (mm day^{-1}) is shown in (b) for winter and (d) for summer. Note that color-scale is different in (b) and (d) to better display the precipitation patterns in the different seasons.

CHAPTER 3

Feedback of Tropical Instability Wave - induced Atmospheric Variability onto the Ocean

ABSTRACT

The effects of atmospheric feedbacks on tropical instability waves (TIWs) in the equatorial Atlantic Ocean are examined using a regional high-resolution coupled climate model. The analysis from a 6-year hindcast from 1999-2004 reveals a negative correlation between TIW-induced wind perturbations and TIW-induced ocean currents, which implies damping of the TIWs. On the other hand, the feedback effect from the modification of Ekman pumping velocity by TIWs is small compared to the contribution to TIW growth by baroclinic instability. Overall, the atmosphere reduces the growth of TIWs by adjusting its wind response to the evolving TIWs. The analysis also shows that including ocean currents (mean + TIWs) in the wind stress parameterization reduces the surface stress estimate by 15-25% over the region of the South Equatorial Current. Moreover, TIW-induced perturbation ocean currents can significantly alter surface stress estimates from scatterometers, especially at TIW frequencies. Lastly, the rectification effect from the atmospheric response to TIWs on latent heat flux is small compared to the mean latent heat flux.

3.1. Introduction

Tropical Instability Waves (TIWs) are generated from instabilities of equatorial zonal currents and are a common feature in both the tropical Atlantic (Düing et al. 1975) and Pacific Oceans (Legeckis 1977; Legeckis et al. 1983). Observations reveal TIWs as westward propagating wave-like oscillations of the sea surface temperature (SST) near the equator with a typical wavelength of $\sim 10^\circ$ longitude and a phase speed of $\sim 0.5 \text{ m s}^{-1}$ (Weisberg and Weingartner 1988; Qiao and Weisberg 1995, and references therein). A detailed study of TIWs is necessary because they are an important element in the momentum balance (Weisberg 1984) and in the equatorial ocean heat budget (Hansen and Paul 1984; Bryden and Brady 1989; Baturin and Niiler 1997; Jochum and Murtugudde 2006).

Numerous studies have discussed the generation mechanisms and energetics of TIWs. Analytical studies by Philander (1976; 1978) showed that meridional shear of the zonal currents leads to a barotropic conversion of mean kinetic energy to eddy kinetic energy (EKE), which supports the growth of waves with wavelengths and periods similar to those of the observed TIWs. Cox (1980) showed that baroclinic instability, though less important, is also a source of the EKE that is drawn from the mean potential energy. In addition, frontal instability (Yu et al. 1995) and Kelvin-Helmholtz instability (Proehl 1996) were shown to be important EKE sources for the TIWs. A more comprehensive numerical study of the generation and the energetics of Pacific TIWs has shown that the northern temperature front is baroclinically unstable, while shear of the zonal currents causes barotropic instability at the equator (Masina et al 1999; hereafter MPB). These two different instabilities are phase-locked and are both important energy sources for

TIWs. On the other hand, Jochum et al. (2004; hereafter JMB) found that barotropic instability in the Atlantic was dominant in their energy budget and the baroclinic term was less important.

Chelton et al. (2004) and Xie (2004) demonstrated that ocean-atmosphere interactions involving the oceanic mesoscale occur throughout the world ocean. SST on this scale induces a wind response in the atmospheric boundary layer through modification of the vertical turbulent mixing (Wallace et al. 1989; Hayes et al. 1989). Air over the warm water is destabilized, and increased turbulent mixing of momentum accelerates near-surface winds. Conversely, cold SST suppresses the momentum mixing, decouples the near-surface wind from wind aloft, and hence decreases the near-surface wind. Small et al. (2003) and Cronin et al. (2003) reported that the pressure gradient mechanism of Lindzen and Nigam (1987) is likely to be an important mechanism as well. Furthermore, Chelton et al. (2001) showed that undulating SST fronts by TIWs further affect the perturbation wind stress derivatives in the atmosphere, suggesting a possible feedback from the atmosphere to the TIWs through Ekman dynamics. The lack of simultaneous measurements of ocean currents and wind stresses on the TIW-scale makes it difficult to quantify in great detail the feedbacks from the perturbation wind field on the TIWs.

Pezzi et al. (2004) modeled this SST-wind coupling and showed that it reduces variability of TIWs. Their simple coupling parameterization included the effect of TIW-induced SST variations directly on the wind fields and through the modification in wind stress derivatives. Seo et al. (2007) used a full-physics high-resolution regional coupled

model to explore several aspects of the tropical Pacific TIWs, reproducing the observed coupling strength as a function of SST gradient.

Recent findings on this close coupling between the ocean and the atmosphere at the oceanic mesoscale raise new questions that have been largely unexplored in the aforementioned studies. What is the role of the wind response in the energy budget of TIWs? How do the atmospheric feedbacks amplify or dampen the TIWs? What is the rectification effect on the mean surface heat flux from the atmospheric response to the TIWs? These questions will be addressed in the present study, which is among the first of its kind using a regional coupled ocean-atmosphere model at eddy-resolving resolution.

In the present study, the regionally coupled high-resolution model of Seo et al. (2007) is used to quantify the contribution of tropical Atlantic ocean-atmosphere covariability to the energetics of the TIWs. It is shown that the direct response of winds to the TIW-induced SST imposes a negative feedback on the growth of TIWs. It is also shown that perturbation Ekman pumping due to TIWs (Chelton et al. 2001) is a very small forcing effect compared to baroclinic instability in the equatorial ocean.

It is also argued that ocean currents (mean + TIWs) substantially reduce the surface stress estimation by 15-20% over the large area of the South Equatorial Current. Moreover, TIW-induced perturbation ocean currents can significantly alter the local surface stress estimate during the active TIW season. This suggests that numerical studies of TIWs will suffer from a consistency problem when the model is forced with the observed winds such as scatterometer wind stresses.

Lastly, perturbation latent heat flux generated at the sea surface by evolving TIW-SST is small compared to the contribution from the mean component, indicating only a weak rectification effect on the ocean from these high-frequency perturbations.

In section 3.2, the model and experiment designed for this study are explained. In section 3.3, the main results of the study are discussed, followed by the conclusion and summary in section 3.4.

3.2 Model and Experiment

The coupled model used for the present study is the Scripps Coupled Ocean-Atmospheric Regional (SCOAR) model (Seo et al. 2007). It combines two well-known, state-of-the-art regional atmosphere and ocean models using a flux-SST coupling strategy. The atmospheric model is the Experimental Climate Prediction Center (ECPC) Regional Spectral Model (RSM) and the ocean model is the Regional Ocean Modeling System (ROMS).

The RSM, originally developed at the National Centers for Environmental Prediction (NCEP) is described in Juang and Kanamitsu (1994) and Juang et al. (1997). The code was later updated with greater flexibility and much higher efficiency (Kanamitsu et al. 2005; Kanamaru and Kanamitsu 2007). Briefly, it is a limited-area primitive equation atmospheric model with a perturbation method in spectral computation, and utilizes a terrain-following sigma coordinate system (28 levels). The model physics are same as NCEP global seasonal forecast model (Kanamitsu et al. 2002a) and NCEP/National Center for Atmospheric Research (NCAR) Reanalysis model

(Kalnay et al. 1996) except for the parameterization of convection and radiative processes.

The ROMS solves the incompressible and hydrostatic primitive equations with a free surface on horizontal curvilinear coordinates and utilizes stretched generalized sigma coordinates in order to enhance vertical resolution near the sea surface and bathymetry. The details of the model can be found in Haidvogel et al. (2000) and Shchepetkin and McWilliams (2005).

A flux-SST coupler bridges the atmospheric (RSM) and ocean (ROMS) models. The coupler works in a sequential fashion; the RSM and ROMS take turns integrating while exchanging forcing every 24 hr. The interacting boundary layer between RSM and ROMS is based on the bulk formula for surface fluxes of momentum, and sensible and latent heat adapted from the algorithm of Fairall et al. (1996).

Although the drag coefficient is generally a function of both wind speed and atmospheric boundary layer stability, Liu et al. (1976) showed that, for the typical environmental conditions in the tropics, with near-surface wind speeds of $\sim 7 \text{ m s}^{-1}$, the bulk transfer coefficients are only marginally sensitive to the typical changes in the stability induced by $\pm 0.5^\circ\text{C}$ changes in air-sea temperature difference. Thus bulk transfer coefficients for momentum and the moisture remain largely unchanged by the changes in the atmospheric stability due to TIW SST changes.

Seo et al. (2006) showed that resolving mesoscale variability in the equatorial Atlantic Ocean is important in improving the simulations of large-scale mean SST and the precipitation. The present study uses the identical model setup as in Seo et al. (2006), except for an enhanced atmospheric resolution of $\sim 1/4^\circ$ to match the underlying ocean

grid at $\sim 1/4^\circ$. Comparable high resolution in the coupled model allows for synchronous local feedback of ocean and atmosphere arising in the presence of ocean mesoscale eddies including TIWs.

The initialization and forcing procedures for both cases are as follows. The ROMS ocean was first spun up for 8 years with the Comprehensive Ocean–Atmosphere Data Set (COADS) climatological atmospheric forcing (da Silva et al. 1994) and climatological oceanic boundary conditions from the World Ocean Atlas 2001 (Conkright et al. 2002). Then the SCOAR coupled run was launched for 7 years from 1998 to 2004 with low-wavenumber NCEP/Department of Energy (DOE) Reanalysis II (Kanamitsu et al. 2002b) atmospheric forcing and climatological oceanic boundary conditions. The 6-year solution from 1999 to 2004 is analyzed in this study.

The model domain covers the whole tropical Atlantic basin from 30°S to 30°N and from 70°W to 20°E , including eastern Brazil and western Africa. Since the focus of the present study is the effects of atmospheric feedbacks on TIWs, the domain analyzed here is limited to the region close to the equator where TIW activity is large. Figure 3.1 shows a snapshot of SST that represents the typical spatial patterns of TIWs from the model, in comparison to measurements from the Tropical Rainfall Measuring Mission (TRMM) Microwave Imager (TMI). The simulated TIWs in the model are qualitatively similar to the observations, with cusps of SST north of the equator along the equatorial front. However, an exact correspondence of the modeled TIWs with the observations at any given time is not expected because TIWs are generated by internal ocean dynamics, rather than deterministically forced. On the other hand, the eddy statistics of the waves are well represented in the SCOAR model (Figure 3.2b).

Figure 3.2 shows an annual mean zonal current at 23°W and the EKE of the near-surface currents. The core of the equatorial undercurrent (EUC) reaching $\sim 100 \text{ cm s}^{-1}$ is located at a depth of 150 m, and this compares well with the observations (e.g., Brandt et al. 2006; Schott et al. 2003) and modeling studies (JMB). The maximum EKE, greater than $400 \text{ cm}^2 \text{ s}^{-2}$ is located at the equator, which is also consistent with time-mean perturbation kinetic energy estimated from the observations (Weisberg and Weingartner 1988).

Temporal filtering of data is useful to extract the characteristics of the TIWs (e.g., Hashizume et al. 2001; JMB). However, temporal band-pass filtering alone (e.g., 10-40 days) does not completely rid the system of intrinsic higher frequency (3-15 days) synoptic variability in the atmosphere. A spatial (zonal) filtering in combination with some temporal smoothing is more useful when one aims to highlight co-varying patterns of the ocean-atmosphere signals arising from fast-moving TIWs (e.g., Chelton et al. 2001; Small et al. 2003). Thus all the variables analyzed in this study are zonally high-pass filtered to retain the signals of the ocean and the atmosphere less than 10° longitude and also 5-day averaged to reduce the fast-changing atmospheric and oceanic variability.

3.3 Results

3.3.1 Impact of wind-current covariability on the TIWs

Figure 3.3 shows a snapshot of TIW-SST overlaid with surface currents and wind stresses. Anticyclonic ocean currents are generated north of the equator in association with TIWs (Figure 3.3a), over which large-scale winds are southeasterly, traversing the SST front (Figure 3.3b). Figure 3.4 shows a 3-day averaged snapshot of SST anomaly,

SST' , overlaid with the perturbation surface currents, \bar{u}' , and wind stresses, $\bar{\tau}'$, associated with the TIWs. SST' and $\bar{\tau}'$ have an in-phase relationship, such that warm (cold) SST' enhances (reduces) southeasterly background atmospheric flows. This is a result of changes in stratification of the lower atmospheric boundary layer according to the underlying SST' which in turn leads to the atmospheric adjustment of vertical turbulent mixing of momentum (Wallace et al. 1989; Hayes et al. 1989).

Apparent in Figure 3.4 is that $\bar{\tau}'$ is generally in the opposite direction of \bar{u}' , particularly for the meridional components in Figure 3.4a. Figure 3.5 shows a simple schematic representation of such a relationship. Cold, newly upwelled waters from the equator are pushed northward by TIWs while they drive warm water from the north equatorward (Figure 3.3a). The anomalous meridional currents are slowed down by perturbations in meridional surface winds, which are generated in response to the TIW-SST. This feedback results in a significant negative correlation north of the equator where TIWs are most energetic (Figure 3.6a). The significant positive correlation south of the equator can be understood similarly.

The relationship between the zonal TIW perturbation currents and wind stresses is more complicated because of asymmetric responses in the southern and northern part of the TIW-SST. In the northern flank of the eddy (Figure 3.4b, and Figure 3.5b), the above explanation is true, where zonal wind stress and zonal surface current generally oppose each other. This is because warm SST increases the easterly background winds where TIWs generate eastward currents (Figure 3.3a). Near the equator, however, a significant positive correlation indicates that winds and currents are aligned together zonally. This results when the warm water pushed by TIWs from the north turns westward at the

equator to close the anticyclonic ocean eddy, over which easterly winds are accelerated (Figure 3.3a, 3.4b). Figure 3.6b shows bands of positive correlation near the equator and negative correlation north of the equator. We now discuss how these correlation patterns translate into the EKE budget of the TIWs.

Here we use a similar technique as used by MPB and JMB, based on the EKE budget. The difference is that in their equation the eddy component is defined as a deviation from the time mean flow, whereas here it is defined as a deviation from the 10° longitudes zonal running mean averages. In the Pacific Ocean, a longer cutoff wavelength could be used in band-pass filtering, while this is not desirable in the tropical Atlantic Ocean because the basin is much smaller and this would give rise to more ocean grid points lost from the continental boundary. It should be noted however that the results discussed here are not significantly altered by the choice of cutoff wavelength of the zonal filter, so long as the TIW-signals are retained.

MPB estimated each term of the EKE budget in the tropical Pacific Ocean using a numerical ocean model. The EKE equation can be written as

$$\vec{U} \cdot \vec{\nabla} \vec{K}_e + \vec{u}' \cdot \vec{\nabla} \vec{K}_e = -\vec{\nabla} \cdot (\vec{u}' p') - g \rho' w' + \rho_o (-\vec{u}' \cdot (\vec{u}' \cdot \vec{\nabla} \vec{U})) + \rho_o A_h \vec{u}' \cdot \nabla^2 \vec{u}' + \rho_o \vec{u}' \cdot (A_v \vec{u}'_z)_z + \vec{u}'_{sfc} \cdot \vec{\tau}'_z \quad (1)$$

The capital letters denote the annual mean values and the primes are zonally band pass filtered values. \vec{K}_e is the EKE, (u, v, w) the ocean velocity vectors, p the pressure, ρ the density, g the gravitational acceleration, A_h and A_v are the horizontal and vertical

viscosities, respectively, and $\vec{\tau}$ the surface wind stress. The terms on the LHS are horizontal and vertical advects of EKE by the mean and eddy currents. Annual mean local tendency of the EKE is negligible. The first term on the RHS is the vertical and horizontal radiation of energy, and the second term represents baroclinic conversion process, whereby mean available potential energy is converted into EKE. The third term is the horizontal deformation work that represents a conversion from mean kinetic energy to EKE. The fourth and fifth terms designate the horizontal and vertical dissipation, respectively, of EKE by the eddies. The last term, which is the focus of the present study, corresponds to the effect of the correlation of currents and wind stresses integrated to the depth at which momentum input from wind stress vanishes.

From the estimates of each term of equation (1) using their model output, JMB concluded that barotropic conversion of the zonal flow, the component, $-\rho_o(u'v'U_y)$, of the full term, $\rho_o(-\vec{u}' \cdot (\vec{u}' \cdot \vec{\nabla} \vec{U}))$, was the dominant source for the TIW EKE. Other deformation terms in the barotropic convergence rate, $-\rho_o(u'u'U_x + u'v'V_x + v'v'V_y)$, and the baroclinic conversion rate, $-g\rho'w'$, were argued to be less important.

For the previous studies of the energetics of TIWs, including MPB and JMB, the effect of the correlation between ocean surface currents and wind stresses, the last term of equation (1), was zero by construction because their models were forced with climatological wind. Vertical averaging of equation (1) gives an estimate of the relative importance of this term, $\vec{u}'_{sfc} \cdot \vec{\tau}'_z$, compared with, for example, the barotropic convergent rate of the zonal flow, $-\rho_o(u'v'U_y)$. Figure 3.7 shows the 6-year mean and zonal mean $\rho_o(u'v'U_y)$ and $\vec{u}'_{sfc} \cdot \vec{\tau}'_z$ averaged from the surface to 150 m depth. This depth range

should include the maximal effects of both of these terms. For example, the center of the EUC is located at 150 m depth (Figure 3.2a) where $-\rho_o(u'v'U_y)$ is most dominant (JMB). Wind input, in contrast, should be largest near the surface and decrease to small values near the center of the EUC.

The magnitude of the time and zonal mean barotropic conversion of the zonal flow, $-\rho_o(u'v'U_y)$, in the present model compares well with the estimate of JMB, although there is a secondary peak at 3°N, which was not seen in their study. The sign of the energy conversion rate estimated in each direction agrees with the map of correlation. Positive correlation of zonal winds and currents (Figure 3.6b), for example, results in an EKE source at the equator (Figure 3.7). Overall, the net impact of the correlation of \vec{u}' and $\vec{\tau}'$ is largely negative, with its peak at 2°N. At this particular latitude, the wind contribution to the TIW energy budget is large, amounting to roughly 40% of the barotropic convergent rate term. If averaged over TIW region (2°S-5°N), the contribution from wind-current coupling is ~10% of the barotropic conversion term, which suggests that overall wind-current coupling is small but significant sink of EKE of the TIWs. This is one of the main results of this study. This agrees with the observational study by Polito et al. (2001) who showed, based on the analysis of TIW anomaly relationship using the satellite data and assuming geostrophy, that meridional wind speeds are in quadrature with sea surface heights, and thus in opposition to the phase of meridional TIW currents. This implies that the opposing winds slow down the surface current associated with the TIWs.

In addition to the feedback arising from a direct response of winds to TIWs, Chelton et al. (2001) found that perturbation wind stress curl generated at the front by

TIWs could be an additional feedback. Spall (2007) discussed how the observed relationship of SST and wind stresses affects the baroclinic instability of the ocean through Ekman pumping. Then he applied this model to a classic linear, quasi-geostrophic stability problem for a uniformly sheared flow originally studied by Eady (1949). For the case of southerly background winds blowing from cold to warm waters, his analysis indicates that Ekman pumping and the forced vorticity would reduce the growth rate and wavelength of the most unstable wave (Figure 1 of Spall 2007).

In the current model, the effect of Ekman pumping on the TIWs is estimated by comparing the magnitudes of Ekman pumping velocity, w_e' , and perturbation vertical velocity, w' , from the model output which enters the baroclinic conversion term (Equation 1). This w' is computed at the base of the mixed layer, which is defined as the depth at which SST decreases by 0.5°C from the sea surface. Hovmöller diagrams of w' and w_e' at 2°N for one particular TIW-season (mid-May 2001 to January 2002) illustrate the westward propagating features of both w' and w_e' , although w' exhibits more coherent spatial structures that resemble TIWs, with much stronger amplitudes. Time series of w' and w_e' at 2°N , 30°W confirm that the amplitudes of w' are much stronger than those of w_e' throughout the whole 6-year period.

This suggests that the effect of wind stress curl due to the zonal SST gradient is a minor contribution to the TIWs compared to the baroclinic energy source intrinsic to the ocean. However, this result comes with the caveat that Ekman pumping velocity becomes singular at the equator, and the variability in upwelling due to direct wind effects is difficult to quantify.

Hence, the net effect of the two sources of atmospheric feedback (i.e. a direct response of wind and Ekman pumping) due to TIW-SST weakly damps the TIWs. This is consistent with the results by Pezzi et al. (2004) who parameterized this feedback effect by adding an empirical correlation between SST and surface wind to the forcing fields of their ocean general circulation model (OGCM).

3.3.2 Impact of Surface Current on Wind Stress

The Quick Scatterometer (QuikSCAT) measures wind stresses at the sea surface from the intensity of the backscatter in the Ku-band (Kelly et al. 2001). This stress is a function of the ocean surface state, including roughness, as well as atmospheric background winds (Chelton and Frelich 2005). Kelly et al. (2001) showed that the difference of mean winds from the QuikSCAT and the Tropical Atmosphere-Ocean (TAO) array closely resembles the mean equatorial surface currents, and this is attributed to the QuikSCAT measuring the relative motion of air and sea.

Here the effect of TIW-induced surface currents on the surface wind stress estimation is examined. The surface wind stresses are computed for the different scenarios with the knowledge of the model 10-m winds and the ocean surface current using bulk formulae. The wind stress parameterization of QuikSCAT can be written as

$$\vec{\tau}_1 = \rho C_d |\vec{u}_a - \vec{u}_o| (\vec{u}_a - \vec{u}_o) \quad (2)$$

where ρ is the air density, C_d is the drag coefficient (1.3×10^{-3}), \vec{u}_a is the atmospheric wind velocity and \vec{u}_o is the ocean surface current velocity. Thus $|\vec{\tau}_1|$ is an estimated

surface stress magnitudes in the presence of the surface ocean current (mean currents + TIW currents). If the ocean surface were motionless, the wind stress, $\vec{\tau}_2$, would be

$$\vec{\tau}_2 = \rho C_d |\vec{u}_a| |\vec{u}_a| \quad (3)$$

If the effect of TIW currents on wind stresses is removed by zonal lowpass filter, this wind stress, $\vec{\tau}_3$, can then be written as

$$\vec{\tau}_3 = \rho C_d |\vec{u}_a - \vec{u}_{o_lowpass}| (\vec{u}_a - \vec{u}_{o_lowpass}) \quad (4)$$

where $\vec{u}_{o_lowpass}$ is low-passed surface current velocity to remove the TIW currents. Comparison of $|\vec{\tau}_1|$ and $|\vec{\tau}_2|$ gives an estimate of effect of ocean currents on the surface wind stresses. Comparison of $|\vec{\tau}_1|$ and $|\vec{\tau}_3|$ will show the effect of TIW-induced perturbation ocean currents on the surface wind stresses. Figure 3.9a shows a time series of $|\vec{\tau}_1|$ at 2°N averaged over 20°W and 15°W, where the TIW activity is large. Time series of $|\vec{\tau}_1|$ exhibits a strong intraseasonal variability, in particular during the second half of the year, when TIWs are active. The annual mean wind stress over this area is roughly 0.027 N m⁻².

Figure 3.9b shows that $|\vec{\tau}_1| - |\vec{\tau}_2|$ is mostly negative, with larger deficit in $|\vec{\tau}_1|$ in the second half of each year. This indicates that including ocean currents reduces the wind stress estimate at this latitude (2°N) evidently because mean South Equatorial Current is in the same direction as the large-scale winds. This is consistent with the

results of Kelly et al. (2001). Figure 3.10a shows the map of the annual mean $\frac{|\vec{\tau}_1| - |\vec{\tau}_2|}{|\vec{\tau}_1|}$.

Over the large area across the equator and the coastal regions, the effect of the ocean surface current is to reduce the surface stress by 15-20% in the current model, consistent with the previous studies (Pacanowski 1987; Luo et al. 2005; Dawe and Thompson 2006). Even larger values found at the coastal oceans suggest that strong variability of the coastal currents can significantly alter the estimated surface stresses near the coast.

Figure 3.9c shows a 6-year time-series of $|\vec{\tau}_1| - |\vec{\tau}_3|$, which closely resembles TIW currents in the ocean (Figure 3.9d, with correlation coefficient of -0.8). This shows the importance of fluctuating ocean currents on the estimation of wind stress. Since the annual mean of $|\vec{\tau}_1| - |\vec{\tau}_3|$ is close to zero because of the oscillatory cancellation of the TIW currents, the annual mean TIW-currents do not significantly affect the annual mean surface wind stress estimates. However, it should be noted that during the active season of the TIWs, TIW currents substantially modify the estimate of the surface wind stress.

Figure 3.10b shows one example from the 5-day averaged fields centered on June 23,

2000 in the model. The spatial map of $\frac{|\vec{\tau}_1| - |\vec{\tau}_3|}{|\vec{\tau}_1|}$ demonstrates the alternating bands of

positive and negative contribution from the TIW-induced perturbation currents. During this particular period, the effect of TIW currents on the surface stress can be ±25-30%.

Considering the alternating phases of the waves, the peak-to-trough difference is perhaps

even larger. The higher $\frac{|\vec{\tau}_1| - |\vec{\tau}_3|}{|\vec{\tau}_1|}$ ratio (<-40%) near the coast suggests that mesoscale

current variability associated with oceanic ring formation in the north Brazil Current

(Johns et al. 1998) can be of substantial importance to the surface stress estimation in this region.

A large influence of the perturbation ocean current on the surface stress estimation implies a potential problem in those numerical ocean modeling studies where the QuikSCAT-derived wind stress product is prescribed at the sea surface. In reality and in the SCOAR model, TIWs induce intraseasonal variability in the atmospheric wind field, whereas in OGCMs forced with high-frequency wind fields, TIWs occur with random phase and will in general be mismatched with specified local surface winds. The large alteration of surface stress by the TIW currents suggests that, in these forced models, the estimation of surface stress may be significantly misestimated, leading to a possible source of error associated with this coupled feedback.

3.3.3. Implication of TIW-Induced Latent Heat Flux on SST

Observational studies have revealed a negative impact from the perturbation surface heat flux on the evolving SST of TIWs. Deser et al. (1993) found a correlation between SST and stratocumulus cloudiness, where increased cloudiness over warm SST reduces incoming solar radiation flux, thus cooling the SST. Numerous investigators (e.g., Thum et al. 2002; Liu et al. 2000; Zhang and McPhaden 1995) have shown that increased latent and sensible heat flux is found over the warm phase of TIWs due to strong coupling between SST and winds, which dampens the growth of the TIWs. Here we examine how the perturbation latent heat flux generated by TIWs compares with zonal mean latent heat flux, i.e., the rectifying effect from perturbation heat flux to the mean SST.

In the bulk parameterization (Fairall et al. 1996), latent heat flux (LH) can be written as

$$LH = \rho L C_H U (\Delta q), \quad (5)$$

where ρ is air density of air, L is the latent heat of vaporization of water, C_H is the bulk exchange coefficient, U is wind speed, and Δq is difference between specific humidity of air and the saturation specific humidity at the temperature of the ocean surface. Thus LH is proportional to the product of U and Δq . Reynolds averaging yields

$$\overline{LH} = \rho L C_H (\overline{U \Delta q} + \overline{U' \Delta q'}), \quad (6)$$

where the bar denotes the 10° longitude running mean, and the primes denote the deviations from the zonal running mean. Thus zonally averaged latent heat flux in the equatorial ocean is determined both from the zonal mean and the deviation of the product of wind and humidity differences. Figure 3.11 shows a 6-year time series of mean and deviation component of latent heat flux at the representative region of 2°N averaged over $30^\circ\text{W}-10^\circ\text{W}$. The time-average of the mean latent heat flux at this latitude is roughly -150 W m^{-2} . The deviation can reach $\sim 1-2\%$ of the mean, but is generally small compared to the mean. This implies that rectification from the perturbation latent heat flux onto the heat budget in the equatorial ocean is close to zero.

Zhang and McPhaden (1995) found that a 1°K change in SST due to TIWs creates a latent heat flux anomaly of $\sim 50 \text{ W m}^{-2}$ in the eastern Pacific Ocean. Seo et al. (2007) found comparable values for perturbations of latent heat flux ($34 \text{ W m}^{-2} [1^{\circ}\text{K SST}]^{-1}$) in their eastern Pacific TIW model. The current model agrees with these estimates in the eastern Pacific and generates approximately 25 W m^{-2} changes in latent heat flux due to the 1°K change in TIW-SST (not shown). Thum et al. (2002) demonstrate from a simple calculation that this amount of anomaly in latent heat flux would produce $\sim 0.5^{\circ}\text{C}$ cooling of warm water, indicating a negative feedback to the TIW-SST. The present analysis of latent heat flux reveals, however, that if these alternating positive and negative latent heat flux anomalies are averaged over the TIW period, a zonal cancellation makes the net contribution from the perturbations small compared to the mean contribution.

It should be emphasized that the TIWs do potentially rectify lower-frequency coupled variability through their contribution to the large-scale SST gradients (Jochum and Murtugudde 2006). Accumulation of small annual mean perturbation heat and momentum fluxes could be important for the long-term climatic bias in SSTs and the equatorial current system in the tropical Atlantic Ocean (JMB). This low-frequency rectification must be revisited in much longer coupled simulations, but the focus here is on the rectification by the high-frequency atmospheric response to TIW-induced SST.

3.4 Summary and Discussion

Ocean-atmosphere covariability arising in the presence of tropical instability waves was examined using a regionally coupled high-resolution climate model in the tropical Atlantic Ocean. One of the goals of the present study was to study the impact of

atmospheric wind response on the TIWs. Two mechanisms by which atmospheric wind fields feed back on to TIWs are a direct exchange of momentum and through a modification of wind stress curl.

The perturbations in wind field are generated by undulating SST fronts of TIWs, which also produce perturbation surface currents. It was shown that these wind perturbations and TIW-induced currents are negatively correlated over the TIW region. Thus the perturbation surface winds are in the opposite direction to the surface currents, which slows down the TIW-currents. In the EKE equation of the TIWs, this effect is a sink. At 2°N, this energy sink amounts to ~40% of the barotropic conversion rate, which is the most dominant EKE source to the TIWs (JMB). If averaged over the TIW region (2°S-5°N), the wind contribution is roughly 10% of the barotropic conversion term.

Perturbations in wind stress curl are generated due to the TIW-induced SST gradient (Chelton et al. 2001). This wind stress curl generates perturbation Ekman pumping over the TIWs. Spall (2007) showed that Ekman pumping damps the baroclinic instability in the ocean in the presence of southerly background wind. However, the present results suggest that in the case of Atlantic TIWs Ekman pumping variability is negligible compared to the dynamically induced variability of upwelling. Thus, TIW induced wind curl variations would not significantly modify baroclinic instability processes.

Furthermore, Ekman currents forced by the TIW-induced wind stress anomalies are many orders of magnitude smaller than the TIW currents (not shown). Thus their impact on the temperature will be negligible. This indicates that the variability of SST altered by already negligible TIW-induced Ekman currents is not important.

Overall, the atmosphere reduces the growth of TIWs by adjusting its wind variability according to the underlying TIW SST field. This result corroborates the previous idealized modeling study by Pezzi et al. (2004), who implicitly includes these two atmospheric feedback mechanisms in their wind stress parameterization.

In addition, the effect of surface currents on wind stress magnitude is discussed. Over the large area across the equator in the Tropical Atlantic Ocean, the ocean currents, including mean and TIWs, reduce surface wind stress estimates, with the maximum effects of 20% at 2°N, 20°W. This is because the westward South Equatorial Current is in the same direction as the large-scale atmospheric easterly flow (Pacanowski 1987).

In the annual mean, TIW-currents only marginally rectify to affect the wind stress estimates due to the oscillatory cancellation. However, at any time during the active TIW season, they can alter the local wind stress estimate by ±25-30% depending on the phase of the waves. Alternating phases of waves indicates that the peak-to-trough difference of surface stress may be even larger. This implies a potential for not only generating low-frequency rectification but will also generate a mismatch between the TIWs simulated in forced ocean models with prescribed observed QuikSCAT wind stresses. The inconsistency between these TIWs and the specified wind forcing when they are in the wrong phase may induce a spurious damping or strengthening of TIWs through the aforementioned coupling of the ocean current and the wind stress.

In such forced model simulations with the observed large-scale QuikSCAT wind forcing, one way to include the effect of coupling of wind and current would be to add, in the prescribed large-scale QuikSCAT forcing, spatially (and/or temporally) high-pass filtered wind fields that are regressed on to the model's SST anomalies by TIWs. A test

of this method would be to compare such forced ocean simulations with fully coupled simulations (such as with the SCOAR model). The results will provide a quantitative estimation of potential impact of mismatch between the specified wind stress forcing and the model's TIWs.

Finally, the rectification effect of perturbations on the atmosphere due to TIWs is examined in terms of latent heat flux. A Reynolds averaging of the latent heat flux equation showed that zonal canceling of perturbation terms of wind speed and humidity differences gives rise to only a 1-2 % difference in latent heat flux compared to its mean contribution. This implies that, although negative feedback from heat flux response may be large at any given phase of SST, when integrated over TIW periods the perturbation heat flux will not significantly feed back on to the zonal mean heat budget of the Atlantic Ocean.

Although our results suggest that TIW-induced latent heat flux does not rectify the mean SST on the short-time scales, the TIWs still can operate over the larger-scale SST gradient to modulate the horizontal and vertical temperature advection that involves ocean-atmosphere heat and momentum exchanges (Jochum et al. 2006, Jochum et al. 2007). Moreover, there are studies that suggest a link between the interannual variability of the TIWs and the asymmetry of ENSO (e.g., Yu and Liu 2003). Long-term accumulation of small annual mean perturbation heat and momentum fluxes may be important for the longer-term climatic bias in SSTs and the currents in the tropical Atlantic Ocean. The potential low-frequency rectification of these apparently small feedbacks can be better quantified in much longer simulations of the coupled high-resolution model which we are currently carrying out and will report elsewhere. This

study is the first of its kind in addressing TIW feedback processes from a high-resolution full-physics coupled model.

3.5 Acknowledgments

The text of this chapter will appear in full as Seo, H., M. Jochum, R. Murtugudde, A. J. Miller, and J. O. Roads, Feedback of Tropical Instability Wave – induced Atmospheric Variability onto the Ocean, *Journal of Climate*, in press, 2007. The dissertation author was the primary investigator and author of this paper. The coauthor listed in this publication directed and supervised the research which forms the basis for this chapter.

The work was done during HS's visit to NCAR during summer 2006, which was made possible through a student fellowship of the Advanced Study Program. This work forms a part of the Ph.D. dissertation of HS. This research was partially funded by NOAA Grant "Impact of oceanic mesoscale variability on the coupled climate". We gratefully acknowledge additional funding support from DOE (DE-FG02-04ER63857) and NOAA (NA17RJ1231 through ECPC). The views expressed herein are those of the authors and do not necessarily reflect the views of these agencies. The Tropical Rainfall Measuring Mission (TRMM) Microwave Imager (TMI) data are obtained from the Web site of Remote Sensing Systems at <http://www.ssmi.com>.

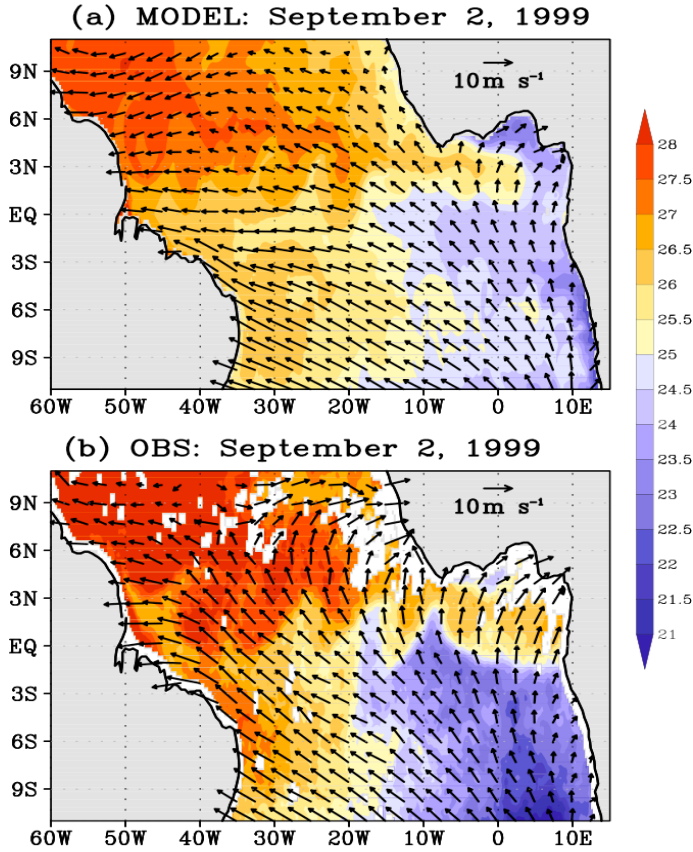


Figure 3.1 Three-day averaged SST and 10-m winds centered on September 2, 1999 (a) in the model and (b) from the satellite of Tropical Rainfall Measuring Mission (TRMM) Microwave Imager (TMI) Tropical instability waves (TIWs) and the QuikSCAT scatterometers. The TIWs are shown as undulations of the SST front near the equator. The TRMM SST and the QuikSCAT wind vectors are re-gridded to the model grid in (a). The vectors are shown on every 10 (5) grid points in x (y).

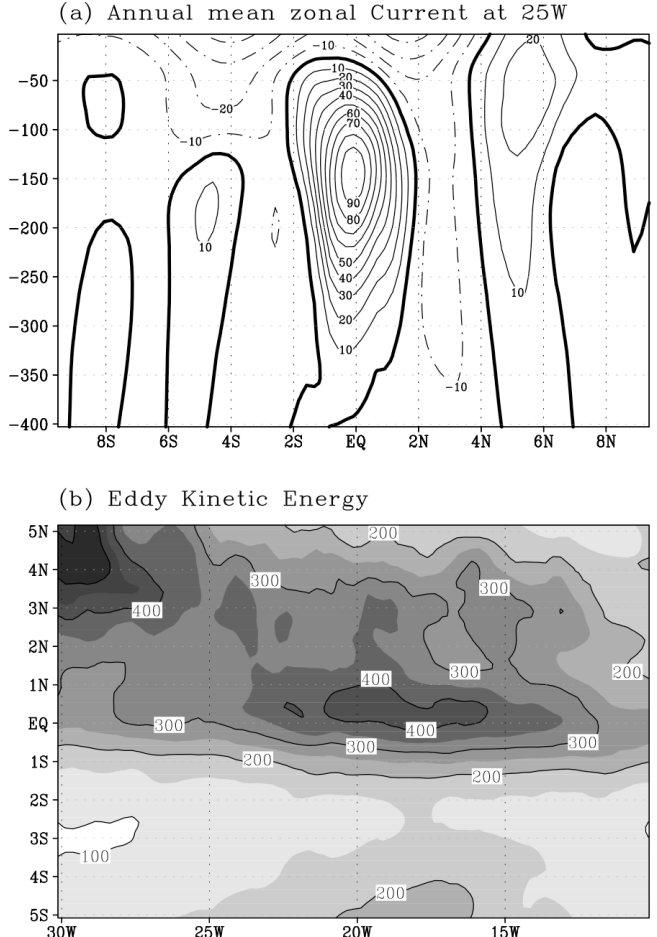


Figure 3.2 (a) Six-year model mean (1999-2004) zonal current along 23°W. The westward south equatorial current is shown by dashed contour lines. Zero values are shown in thick contours. The core of the equatorial under current is located at 150 m depth. The Tsuchiya jets are shown as the eastward subsurface currents centered at 5°N and 5°S. (b) Near-surface model eddy kinetic energy (EKE) computed by $EKE = (u'^2 + v'^2)/2$, where u' and v' are zonally highpass filtered surface currents. Maximum EKE is located north of the equator, along the core of the TIWs.

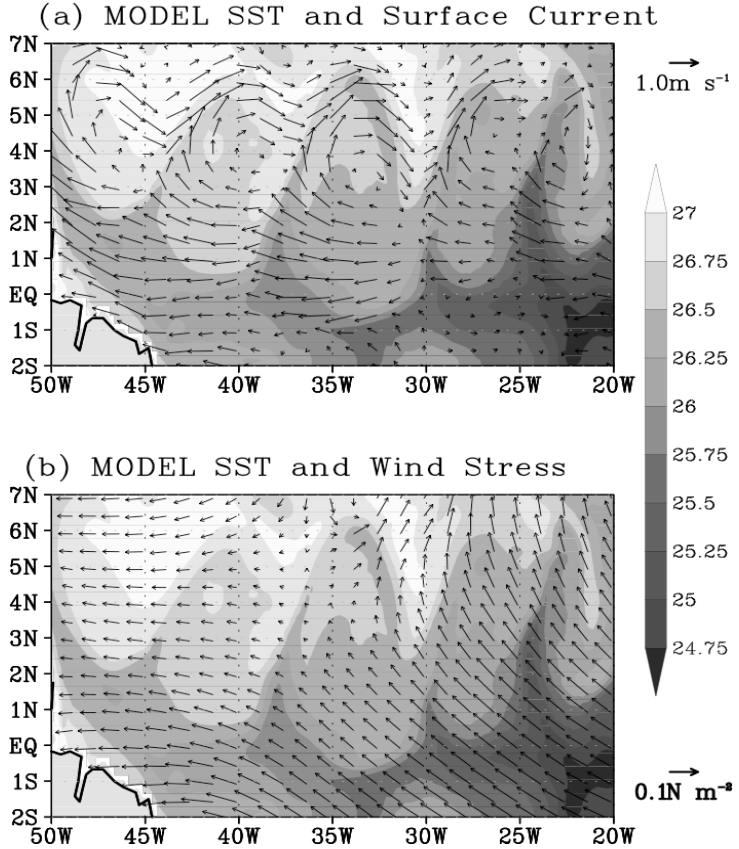


Figure 3.3 Three-day averaged model SST fields centered on September 26, 2000, with (a) the vectors of model surface current (m s^{-1}) and (b) the vectors of model wind stress (N m^{-2}). The vectors are shown on every 5 (2) grid points in x (y).

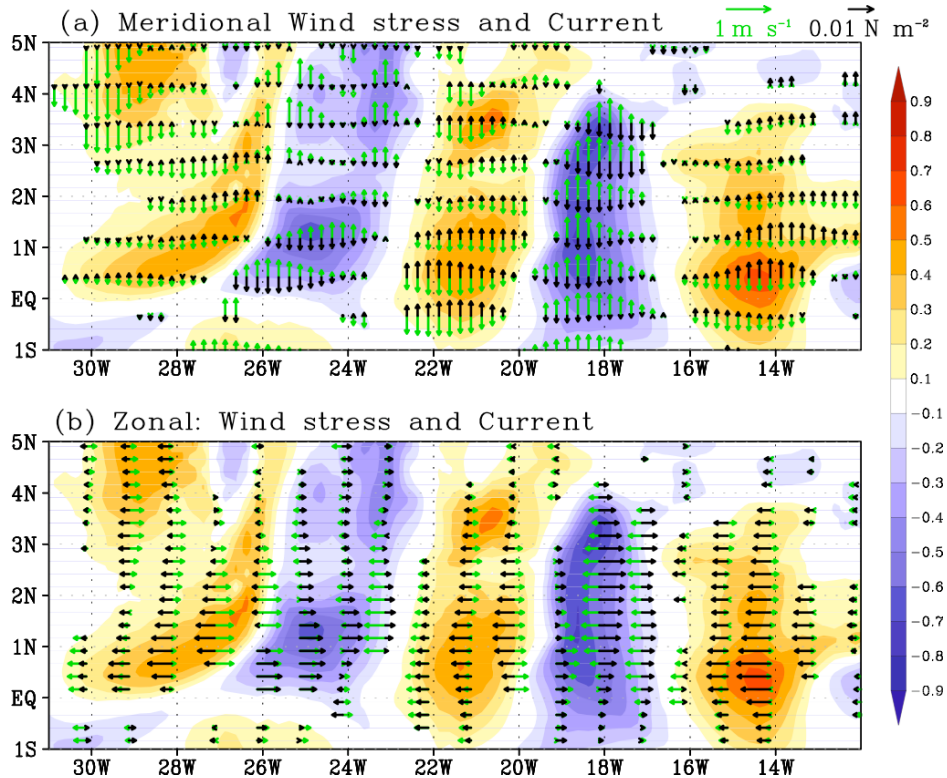


Figure 3.4 Three-day averaged (centered on October 22, 2000) and highpass filtered model SST (color shaded), overlaid with highpass filtered model surface current (green vectors) and model wind stress (black vectors) in (a) the meridional and (b) zonal component.

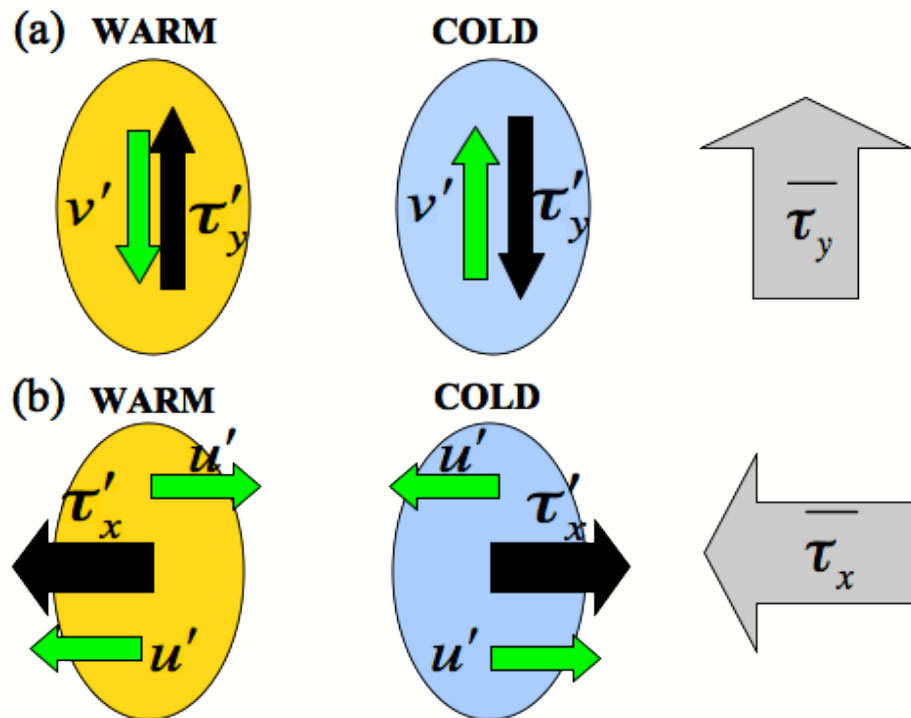


Figure 3.5 Schematic representation of the relationship between wind stress and surface current over TIW-SST. Warm (cold) TIW-SST is shown as light yellow (blue) ovals. Black (green) vectors are perturbation wind stress (surface current). Background wind fields are shown as thick gray vectors.

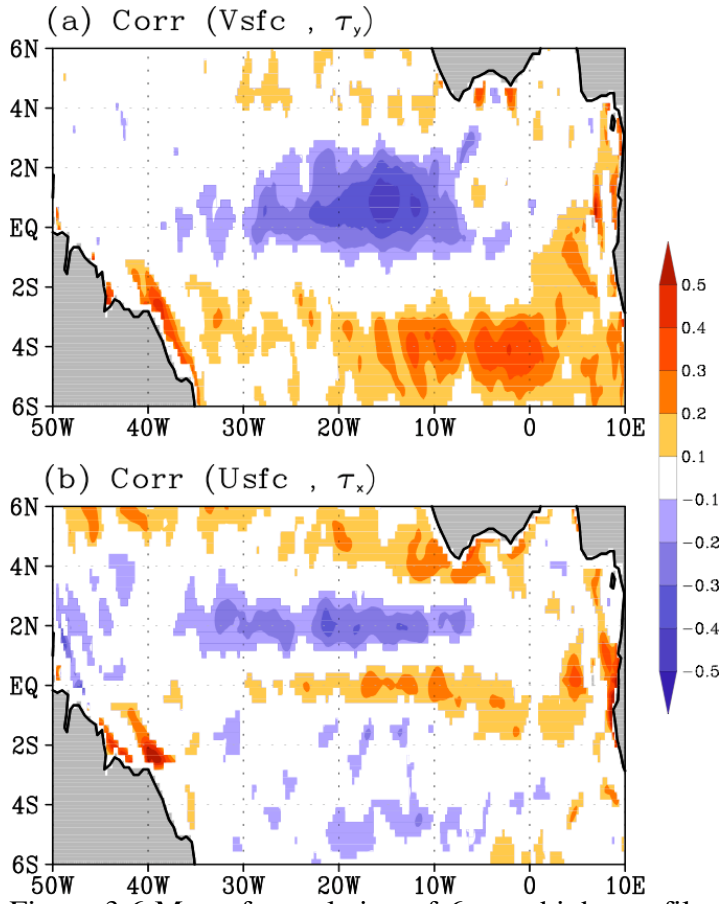


Figure 3.6 Map of correlation of 6-year highpass filtered model wind stress and surface current over tropical Atlantic Ocean in (a) meridional direction and (b) zonal direction.

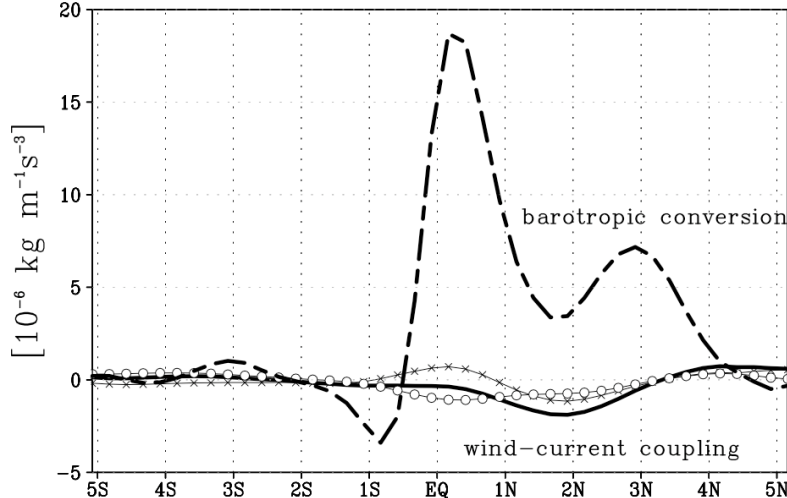


Figure 3.7 Zonal average (30°W - 10°W) of 6-year model mean (dashed line) barotropic conversion rate of the zonal flow, $-\rho_o(u'v'U_y)$ averaged over 150 m, i.e., $\frac{1}{d} \int_d^{sfc} (-\rho_o u' v' U_y) dz$, where d is the depth of the center of EUC (150 m). (Solid line) Time and zonal mean $\bar{u}'_{sfc} \cdot \bar{\tau}'_z$ averaged over 150 m, i.e., $\frac{1}{d} \int_d^{sfc} (\bar{u}'_{sfc} \cdot \bar{\tau}'_z) dz$. Zonal (meridional) component of $\frac{1}{d} \int_d^{sfc} (\bar{u}'_{sfc} \cdot \bar{\tau}'_z) dz$ is shown by the light solid line with x (o).

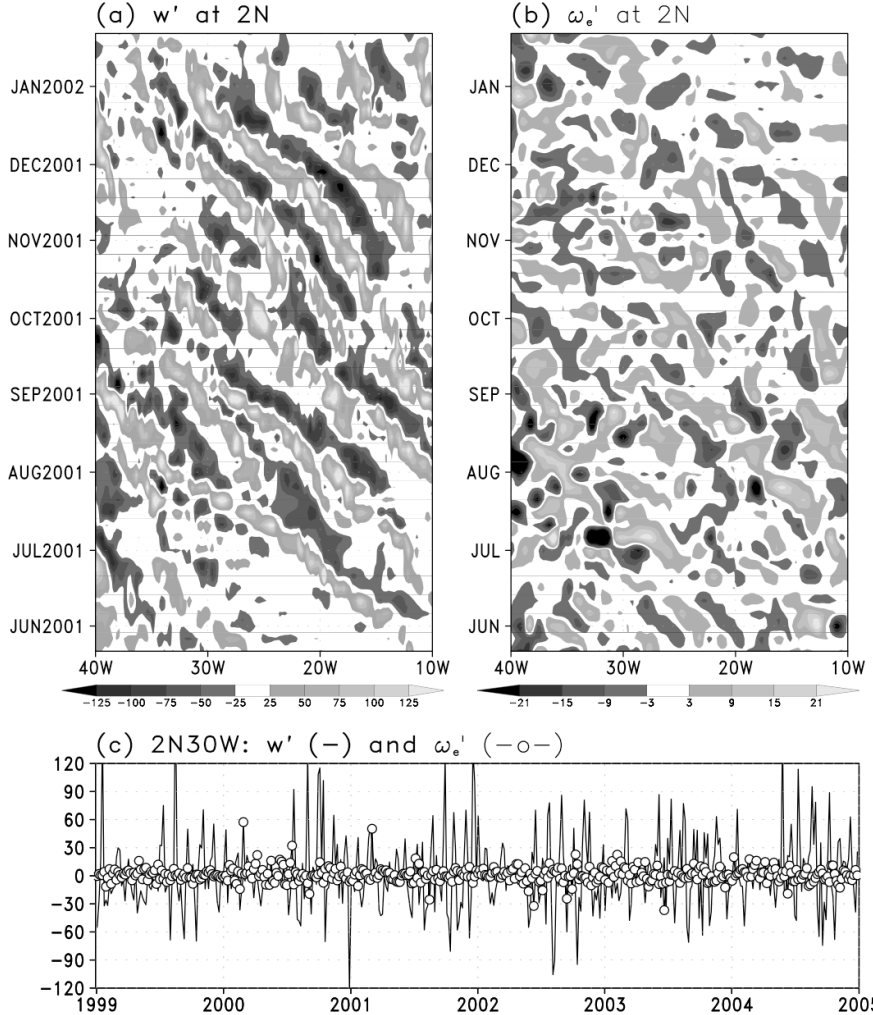


Figure 3.8 Hovmöller diagrams of (a) the model perturbation vertical velocity, w' , from baroclinic convergent rate term ($-g\rho'w'$) and (b) the model Ekman pumping velocity, ω_e' , at 2°N from mid-May 2000 to January 2001. (c) Times series of w' (solid) and ω_e' (line with o) at 30°W, 2°N. Note the different color scales in (a) and (b). Time axis of (a) and (b) denotes January of the year. w' is evaluated at the base of the mixed layer (~40–50 m).

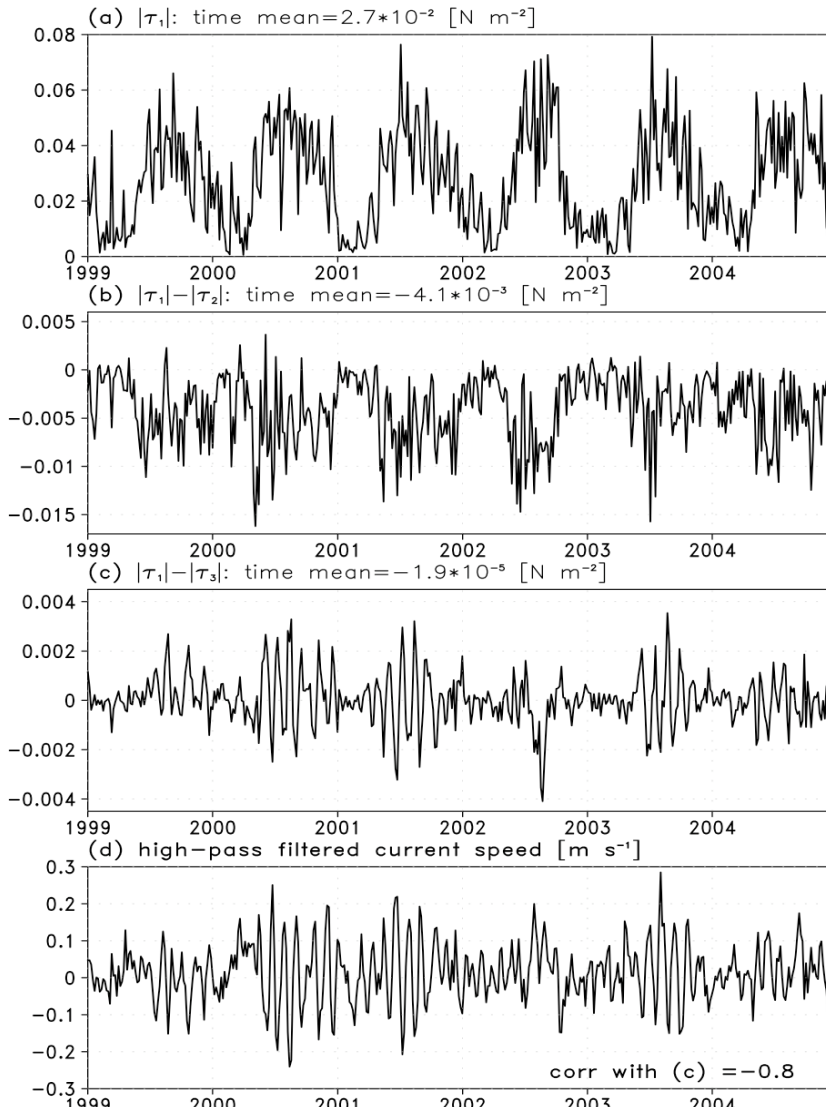


Figure 3.9 Six-year time series of model surface wind stress magnitudes computed for the different scenarios at 2°N averaged over 20°W and 15°W. (a) $\bar{\tau}_1 = \rho C_d |\vec{u}_a - \vec{u}_o| (\vec{u}_a - \vec{u}_o)$, (b) $|\bar{\tau}_1| - |\bar{\tau}_2|$, where $\bar{\tau}_2 = \rho C_d |\vec{u}_a| \vec{u}_a$, and (c) $|\bar{\tau}_1| - |\bar{\tau}_3|$, where $\bar{\tau}_3 = \rho C_d |\vec{u}_a - \vec{u}_{o_lowpass}| (\vec{u}_a - \vec{u}_{o_lowpass})$. \vec{u}_a is the atmospheric wind velocity, \vec{u}_o is the ocean surface current velocity (mean + TIWs), $\vec{u}_{o_lowpass}$ is low-passed surface current velocity. High-pass filtered (TIW) surface current speed (m s^{-1}) is shown in (d). The correlation coefficient of the TIW current speed with $|\bar{\tau}_1| - |\bar{\tau}_3|$ in (c) is -0.8. See text for details.

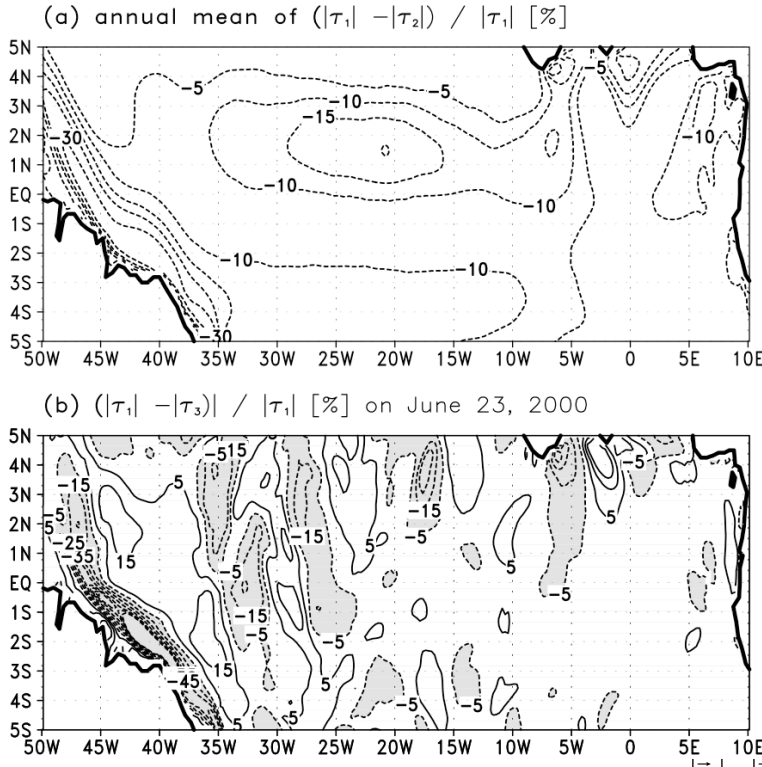


Figure 3.10 (a) Map of ratio (%) of annual mean $\frac{|\vec{\tau}_1| - |\vec{\tau}_2|}{|\vec{\tau}_1|}$. Negative values denote the reduction of wind stress estimate due to the presence of ocean surface current. (b) 5-day averaged (centered on June 23, 2000) ratio, $\frac{|\vec{\tau}_1| - |\vec{\tau}_3|}{|\vec{\tau}_1|}$. Negative values are shaded in gray and contoured in dashed lines. Contour interval is 5% and the zero contour line is omitted.

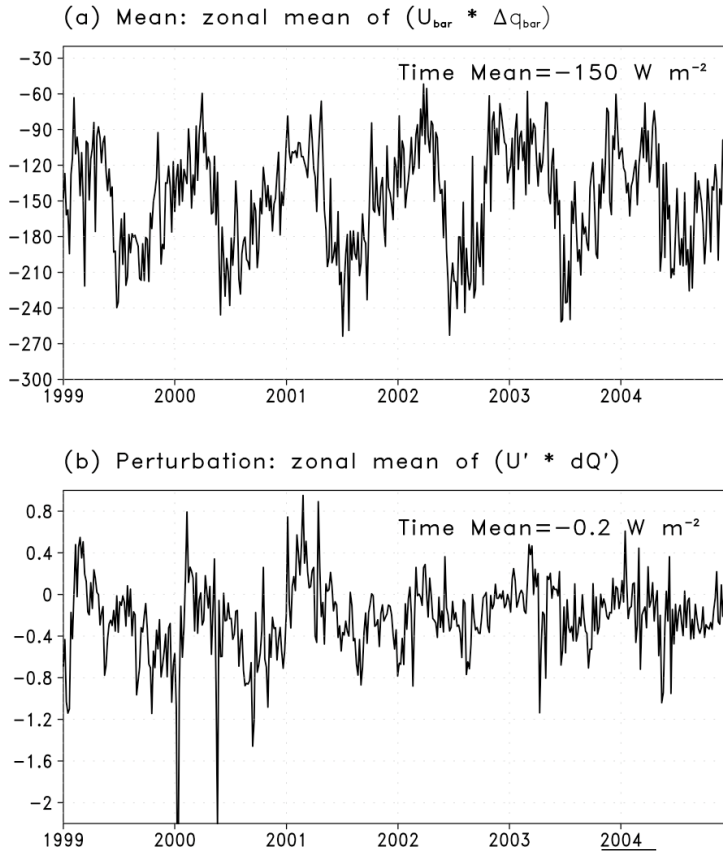


Figure 3.11 Six-year time series of (a) $\rho LC_H \bar{U} \Delta q$ and (b) $\rho LC_H \overline{U' \Delta q'}$ at 2°N averaged over 30°W-10°W in the model. Similar results are found for different areas.

Chapter 4

Effect of Ocean Mesoscale Variability on the Mean State of Tropical Atlantic Climate

Abstract

A regional coupled ocean-atmospheric model is used to investigate the effect of oceanic mesoscale features on the mean climate of the tropical Atlantic. It is shown that, compared to a non-eddy resolving ocean model, resolving oceanic mesoscale variability leads to a cooler mean equatorial cold tongue and a cooler coastal upwelling zone. This changes the meridional SST gradient, and the resulting weaker low-level convergence reduces the mean of rainfall in the marine Inter-Tropical Convergence Zone (ITCZ). The reduced rainfall and the cooler coastal upwelling regions represent a clear improvement of the model solution.

4.1 Introduction

The seasonal cycle of the marine Inter-Tropical Convergence Zone (ITCZ) in the tropical Atlantic (TA) Ocean is associated with seasonal sea surface temperature (SST) variability (Nobre and Shukla 1996). Chiang et al. (2002) discuss the nature of the TA ITCZ, suggesting that the two dominant mechanisms influencing variability of the ITCZ are the local meridional SST gradient and external forcing from ENSO.

While the equatorial upwelling maintains the asymmetric positioning of the ITCZ

most of the year (Xie 2004), in boreal spring the meridional SST gradient is extremely weak which facilitates anomalous latitudinal positioning of the ITCZ. Thus it has been argued that a substantial improvement of seasonal rainfall forecast will be achieved if SST distribution in the TA could be predicted (Nobre and Shukla 1996; Ward and Folland 1991). Unfortunately, most global coupled models fail to reproduce observed SST patterns in the TA, generally exhibiting a warm bias in the coastal upwelling region and incorrect seasonal cycles (Davey et al. 2002).

Jochum et al. (2005, 2004) argue that, because of their impact on the SST gradients, resolving mesoscale structures of the ocean such as Tropical Instability Waves (TIWs) and details of coastal upwelling along the African coast should improve simulations of TA SST. They show that in a forced ocean model the SSTs improve by going to an eddy-resolving model. A caveat of their study is that the winds were prescribed and did not adjust to this changed SST distribution. Thus, the benefits of increasing the resolution could be either lost or amplified in a coupled model.

The present study is a follow up study to the work of Jochum et al. (2005) and simply tries to see if the improvements of the forced experiments are maintained in the coupled experiments. The main benefits (for SSTs) of increasing the resolution were that because of lower horizontal diffusion, higher, more realistic SST gradients could be maintained. The present short note illustrates that this is still the case in the coupled model and leads to improvements in the rainfall.

4.2 Model and experiment setup

The model used for this study is the Scripps Coupled Ocean-Atmospheric

Regional (SCOAR) model. It couples the Regional Spectral Model (RSM) for the atmosphere to the Regional Ocean Modeling System (ROMS) for the ocean. The model has already been shown to be capable of capturing the salient features of coupled ocean-atmosphere feedback in several regions of the eastern Pacific, including TIWs in the tropical Pacific (Seo et al. 2007).

RSM is a regional extension to the Global Spectral Model (GSM) used in the National Centers for Environmental Prediction (NCEP) / Department of Energy (DOE) Reanalysis (Kanamitsu et al. 2002b). It is thus dynamically and physically consistent with Reanalysis products, which are used for large-scale forcing to produce downscaled fields. The parameterization for deep convection is based on Relaxed Arakawa-Schubert scheme (Arakawa and Schubert 1974; Moorthi and Suarez 1992). Further details about the model physics can be found in Kanamitsu et al. (2002a).

ROMS solves the incompressible and hydrostatic primitive equations with a free surface on horizontal curvilinear coordinates, and utilizes stretched general sigma coordinates in order to enhance vertical resolution near the sea surface and bathymetry. In this study, we use 30 vertical sigma layers, with approximately 10 layers in the upper 100 m in the open ocean, and 20 layers below. Implicit diffusivity associated with 3rd-order upstream horizontal advection is used in the lateral plane as opposed to explicit diffusivity. Mixed layer dynamics are parameterized using a KPP scheme (Large et al. 1994), with vertical mixing coefficient of $10^{-5} \text{ m}^2 \text{ s}^{-1}$ (see Shchepetkin and McWilliams (2005) for details).

The flux coupler (Seo et al. 2007) employs linear horizontal interpolations of surface flux fields (momentum, heat, and freshwater flux) from RSM to ROMS and SST fields from ROMS to RSM. The atmospheric boundary layer is based on bulk

parameterization of Fairall et al. (1996), which is implemented in ROMS. In the bulk formula, the relative motion between surface winds and surface currents are calculated for better representation of wind stress near the equator.

In this study, two coupled experiments are designed to isolate the impact of the oceanic mesoscale on TA climate. In the first run (hereafter L), both RSM and ROMS use low (1°) horizontal resolution. Therefore L does not resolve mesoscale features of the TA Ocean. In the second run (hereafter H), horizontal resolution of RSM remains 1° , but high ($\frac{1}{4}^\circ$) resolution is used for ROMS. Since the two experiments are identical except for their horizontal resolutions for ROMS, the differences between H and L represent the difference between mesoscale eddies in H and horizontal diffusion in L.

ROMS is first spun up for 8 years forced with climatological atmospheric forcing obtained from COADS (da Silva et al. 1994), and initial and boundary conditions from World Ocean Atlas 2001 (Conkright et al. 2002). The end state from the forced ocean run is used as an initial condition for the coupled runs. The large-scale (low wavenumber) atmospheric components specified from NCEP for the period 1998-2004 are used as realistic forcing (downscaling). H and L are further spun up in coupled mode for 1-year of 1998 to allow for surface adjustment processes. Solutions from 1999 to 2004 (6 years) are analyzed in this study.

4.3 Results

Figures 4.1-4.3 show that both H and L are reasonably realistic representations of the TA. This is different from the results usually found in *global* coupled models, which have a reversed east-west SST gradient (Davey et al. 2002). A related global modeling study with a localized ocean-atmosphere coupling in the Atlantic also suggests that

regional coupling leads to a more realistic zonal SST gradient both at the equator and south of it, although systematic SST errors similar to those found here are still present (Huang et al. 2004). Thus, both the H and L solutions are controlled by the low-wavenumber components of the flow specified by the NCEP Reanalysis downscaling procedure. From this it can be speculated that the TA Ocean dynamics may only be of minor importance for TA climate. This reflects the fact that the Atlantic basin is relatively small compared to the tropical atmospheric Rossby radius. However, in spite of the close resemblance of the H and L solutions there are important differences, as discussed below.

Figure 4.1 shows that resolving mesoscale features in the ocean results in different SST patterns that are the most distinct near the equator and African coastal upwelling region. H is colder than L in both regions, with the greatest difference of 0.6°C in the upwelling zone of the African coast. Given that most global coupled models produce a too weak SST-gradient and too warm coastal upwelling (Mechoso et al. 1995; Davey et al. 2002), this result is a major improvement and attests to the importance of the ocean mesoscale in the coupled models for more realistic SSTs in upwelling regions. The larger SST gradients in H, and the resulting colder equatorial cold tongue (ECT) and upwelling have been explained for a forced ocean in Jochum et al. (2005). They showed that by resolving the mesoscale eddies in the ocean, one removes the spurious horizontal diffusion of heat from the warm subtropical warmpool to the cold equator, and this increases the SST gradient and thus makes the ECT and coasts colder and the warmpool warmer. Consistent with their analysis, the subtropics are warmer in H. It is a major result of the present study that these results from the forced model still hold true in the coupled model. The resulting changes in tropical SST affect the trade winds and rainfall as

discussed below.

Changes in near-surface atmospheric winds (Figure 4.2) are directly connected to the underlying SST gradient by changing the meridional sea-level pressure gradient (not shown) (*Lindzen and Nigam 1987*). The meridional wind difference map shows that low-level wind convergence is weaker in H in the ITCZ, leading to less rain there (Figure 4.3). Between the equator and 5°N mean rainfall is reduced by up to 20% and in the subtropics of both the northern (5°N - 20°N) and southern (5°S - 20°S) hemispheres, H increases precipitation by approximately 10%. Increases in mean rainfall in the subtropics are roughly compensated by the deficit in the ITCZ, resulting in mean rainfall over the entire basin from 20°S to 20°N remaining roughly the same (difference in rainfall from 20°S to 20°N is only $-0.0373\text{mm day}^{-1}$). Thus changes in SST gradient associated with better-resolved oceanic eddies cause a basin-scale rearrangement of mean rainfall patterns across the equator. A comparison with the NCEP Reanalysis (Figure 4.3c,d) shows that model-mean rainfall of H in the marine ITCZ, especially east of 35°W is reduced compared to L and in better agreement with the observations. Therefore we argue that there is a significant improvement in the precipitation simulation over the open ocean by going from L to H. Such changes in rainfall are consistent with those in winds, but the changes in the winds are not large enough (<5%) to judge whether they improved or not. Over land, the differences between the present model's and NCEP's land-sea mask and topography render judgments on improvement moot.

4.4 Summary and discussion

A regional coupled model has been used to examine if resolving the oceanic mesoscale field is important in determining the mean climate in the TA. It was found,

somewhat surprisingly to the authors, that the TA climate is largely controlled by the large-scale atmospheric background circulation specified in the model from Reanalysis fields and that TA Ocean dynamics is only of minor importance in most of the domain. However, resolving the oceanic mesoscale results in colder and more realistic coastal upwelling regions along the coast of Africa and in a colder ECT. As already explained by Jochum et al. (2005) for the ECT in a forced ocean model, the reason for colder ECT and upwelling regions is that increasing horizontal resolution in the ocean model removes a spurious horizontal diffusion of heat from the warm subtropical warmpool to the ECT and coastal waters.

A direct effect of the increased SST gradient is a reduced low-level convergence along the ITCZ. It is found that H precipitation is suppressed in the marine ITCZ by 20% with similarly sized increases in precipitation statistics in the subtropics, indicating a basin-scale redistribution of mean rainfall patterns. Comparing with the observations (diagnosed from the NCEP Reanalysis), we conclude that by increasing the horizontal resolution in the ocean model, the rainfall simulation over the open ocean is improved. It should be noted that the precipitation differences between H and L are small ($<1 \text{ mm day}^{-1}$) compared to the ranges in estimates of the available observations: annual mean precipitation is $\sim 4 \text{ mm day}^{-1}$ from Reanalysis fields, $\sim 7 \text{ mm day}^{-1}$ from CPC merged Analysis of Precipitation (CMAP) (Xie and Arkin 1997), and $\sim 6 \text{ mm day}^{-1}$ from satellite measurement of Tropical Rainfall Measuring Mission (TRMM). We chose to compare the model with the NCEP fields, because they are consistent with the prescribed large-scale atmosphere and the physics of the RSM (Kanamitsu et al. 2002a).

Due to the short length of the analyzed runs (6 years), we limit the current analysis to the changes in mean structure of winds and ITCZ arising from resolving

oceanic mesoscale features. However, we can speculate that any changes in SST are likely to affect not only the mean but also the variability of the marine ITCZ. The nature of the altered atmospheric variability by SST changes in the TA will need be addressed with longer-term runs, which are currently under way.

The horizontal resolution of the atmospheric model used in this study is not much finer than that of most global coupled atmospheric models and therefore the atmosphere does not experience the full effects of oceanic mesoscale features. To quantify the importance of the atmosphere resolving oceanic mesoscale features we plan to use the RSM in $\frac{1}{4}^{\circ}$ resolution. This allows for a synchronous coupled feedback arising from ocean mesoscale eddies through the localized wind adjustment and corresponding advection of heat and moisture [as observed by Chelton et al. (2001) and Hashizume et al. (2001) and modeled recently by Small et al. (2003) and Seo et al. (2007)], which is absent in the current model study. This will be the next step in our modeling strategy toward a better understanding of the mean and variability of TA climate as a result of resolving the ocean mesoscale in the TA Ocean.

4.5 Acknowledgments

The text of this chapter, in full, a reproduction of the material as it appears as Seo, H., M. Jochum, R. Murtugudde, and A. J. Miller, Effect of Ocean Mesoscale Variability on the Mean State of Tropical Atlantic Climate, *Geophysical Research Letters*, **33**, L09606, 2006. The dissertation author was the primary investigator and author of this paper. The coauthor listed in this publication directed and supervised the research which forms the basis for this chapter.

The authors thank anonymous reviewers for helpful suggestions. This research

was partially funded by NOAA Grant “Impact of oceanic mesoscale variability on the coupled climate”. We gratefully acknowledge additional funding support from DOE (DE-FG02-04ER63857) and NOAA (NA17RJ1231 through ECPC and CORC). The views expressed herein are those of the authors and do not necessarily reflect the views of these agencies. The TMI data are obtained from the Web site of Remote Sensing Systems.

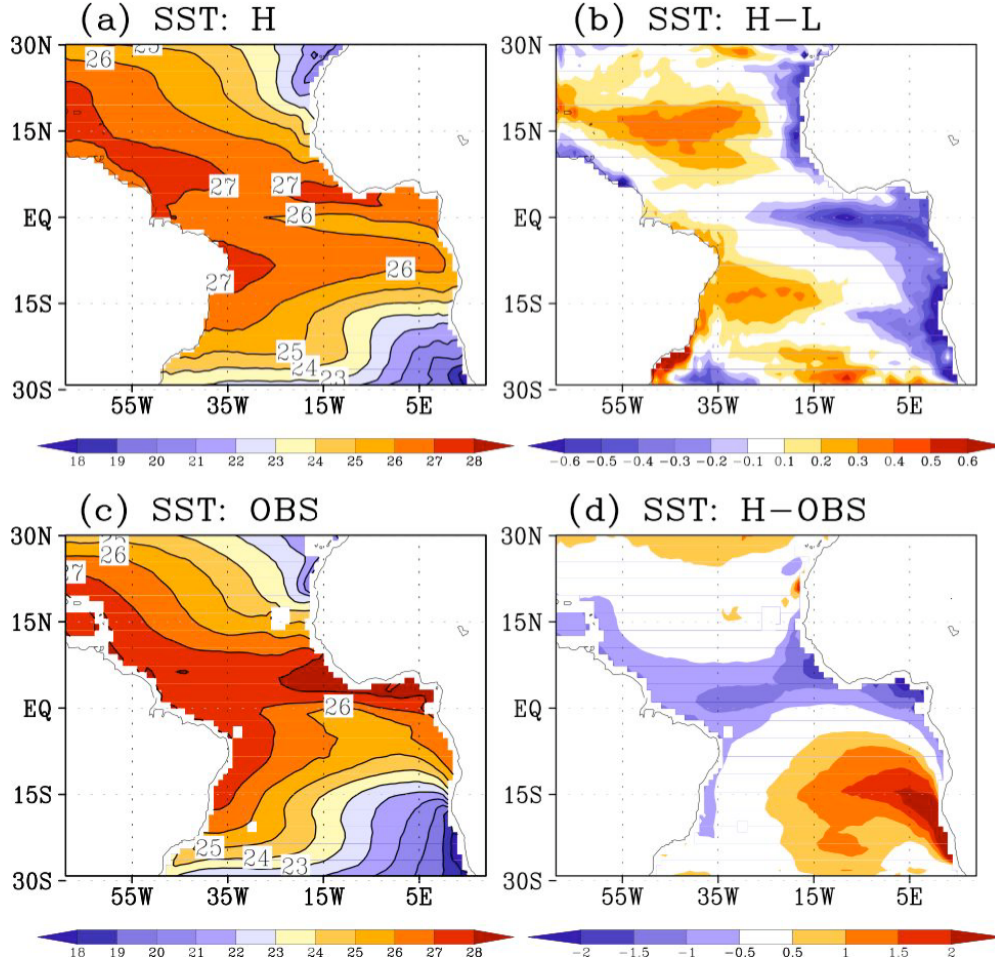


Figure 4.1. Mean SST ($^{\circ}$ C) from 1999 to 2004, (a) H, (b) H-L, and (c) observed SST from Tropical Rainfall Measuring Mission Microwave Image (TMI) (OBS), and (d) H-OBS. H SST is colder by up to 0.6° C in the equatorial cold tongue and African coastal upwelling region, while warmer in the extratropics.

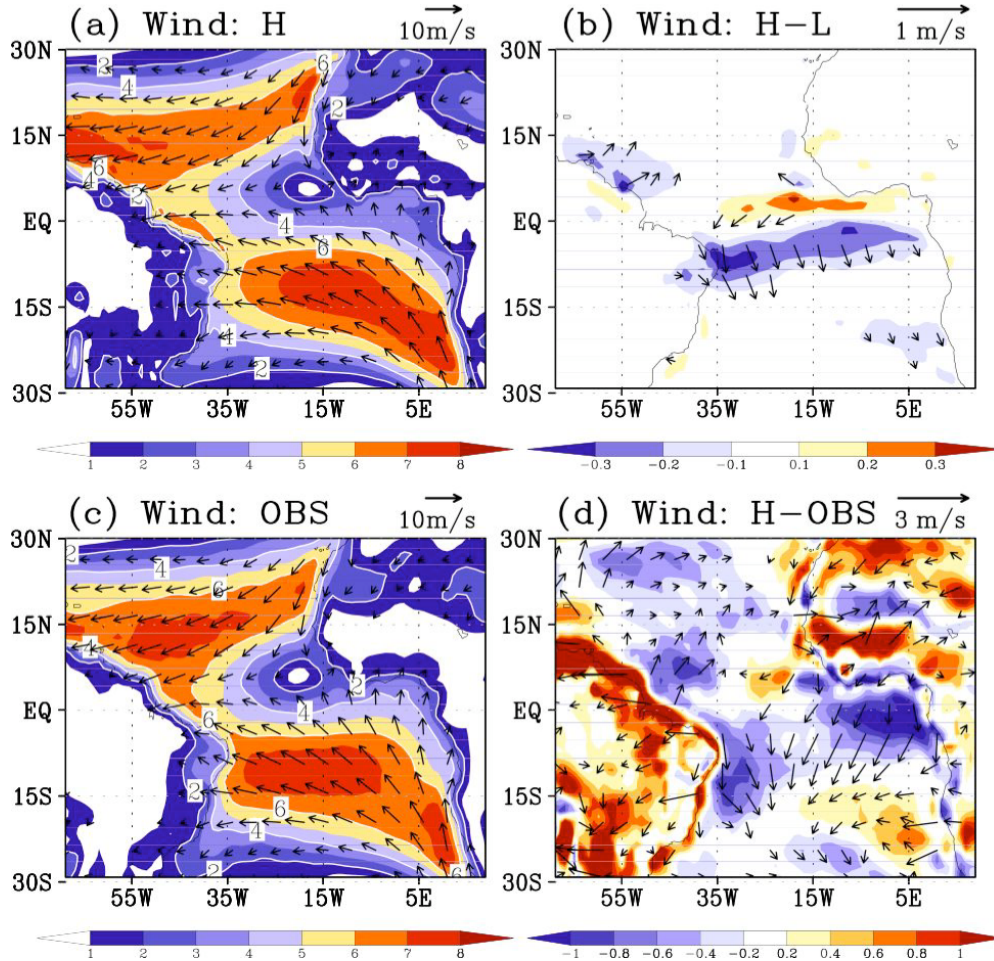


Figure 4.2. Same as Figure 4.1, except for 10 m wind speed (m s^{-1}) and vectors. OBS is the observed wind from NCEP Reanalysis. Difference in wind near the equator shows that wind-convergence is weaker in H, thus weaker ITCZ.

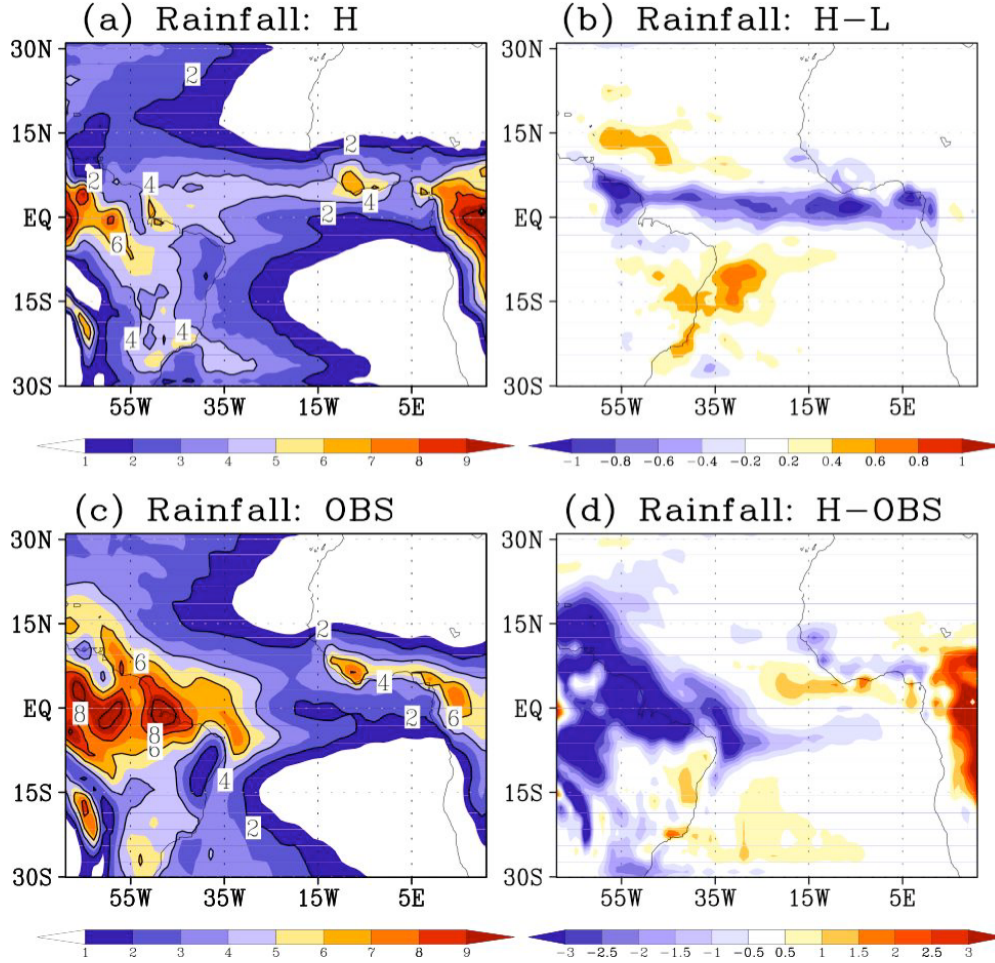


Figure 4.3. Same as Figure 4.1, except for precipitations (mm day⁻¹). OBS is the observed precipitation from NCEP Reanalysis. Rainfall deficit in H near the equator amounts to nearly 20% compared to its mean. Comparing with the observations, rainfall simulation is improved in H over open ocean.

Chapter 5

Precipitation from African Easterly Waves in a Coupled Model of the Tropical Atlantic Ocean

Abstract

A regional coupled climate model is configured for the tropical Atlantic to explore the role of synoptic-scale African Easterly Waves (AEWs) on the simulation of mean precipitation in the marine Inter-Tropical Convergence Zone (ITCZ). Sensitivity tests with varying atmospheric resolution in the coupled model show that these easterly waves are well represented with comparable amplitudes on both fine and coarse grids of the atmospheric model. Significant differences in the model simulations are found in the precipitation fields however, where heavy rainfall events occur in the region of strong cyclonic shear of the easterly waves only on the higher resolution grid. This is because the low-level convergence due to the waves is much larger and more realistic in the fine-resolution simulation, which enables heavier precipitation events that skew the rainfall distributions towards longer tails. The variability in rainfall on these time scales accounts for more than 60-70% of the total variability. As a result, the simulation of mean rainfall in the ITCZ and its seasonal migration improves in the higher-resolution case. This suggests that capturing these transient waves and the resultant strong low-level convergence is one of the key ingredients for improving the simulation of precipitation in global coupled climate models.

5.1 Introduction

Understanding the variability of the Inter-Tropical Convergence Zone (ITCZ) is a major component of the study of the tropical Atlantic climate system (Xie and Carton 2004). The ITCZ exhibits strong seasonal variability, reaching its maximum northward position (7°N - 9°N) in August-September, and migrating to its southernmost location near the equator (3°N - 4°S) in February-April (Chiang et al., 2002). Boreal spring is the season when the ITCZ displays its strongest interannual variability, when the ITCZ can be positioned on either side of the equator due to the weak meridional sea surface temperature (SST) gradient (Chiang et al. 2002). The anomalous rainfall associated with the variable location and strength of the ITCZ can impose devastating environmental and socioeconomic consequences on the heavily populated regions in northeast Brazil and western Africa (Hastenrath and Heller 1977; Folland et al. 1986; Palmer 1986; Nobre and Shukla 1996).

Although the variability in the ITCZ and the SST in this region can be explained to some extent in terms of the interannual and longer-timescale variability (Zebiak 1993; Nobre and Shukla 1996) in combination with remote forcing from the El Niño-Southern Oscillation (ENSO) through teleconnection mechanisms (Enfield and Mayer 1997; Saravanan and Chang 2000), there is no mode of variability stronger than the seasonal cycle in the tropical Atlantic Ocean (Xie and Carton 2004). Furthermore, Davey et al. (2002) reported that most of the state-of-the-art global coupled general circulation models (GCMs) commonly exhibit large biases in the mean climate of tropical regions, particularly in the Atlantic. This indicates that the key processes that determine the mean

and annual cycle of the tropical Atlantic climate are still not yet fully understood (Xie and Carton 2004).

The present study focuses on simulating the mean ITCZ in a coupled climate model and sheds light on the importance of synoptic-scale atmospheric processes. The connection of this transient atmospheric feature to the precipitation over northern Africa and the tropical Atlantic Ocean has been extensively studied (Thorncroft et al. 2003 and the references therein). The low-level positive meridional potential temperature gradient and the negative mid-tropospheric meridional potential vorticity gradient during the summertime indicate the existence of the African easterly Jet (AEJ) (Pytharoulis and Thorncroft 1999). The instability process associated with the baroclinic interaction of these potential temperature and potential vorticity gradients is conducive to the generation of synoptic-scale weather disturbances called African Easterly Waves (AEWs) (Rennick 1976; Reed et al. 1977). Hsieh and Cook (2005) also have pointed out the importance of cumulus convection and the associated release of latent heat within the ITCZ over the African continent in the generation of these atmospheric disturbances. The early analyses of AEWs have revealed the characteristics of these summertime atmospheric disturbances, which have phase speeds of $6\text{--}8 \text{ m s}^{-1}$ westward with periods of 3-5 days (Carlson 1969; Burpee 1972). These waves contribute to the organized convection (Mekonnen et al. 2006) including mesoscale convective systems (Payne and McGarry 1977), and daily precipitation over western Africa (e.g., Frank 1970; Thorncroft and Hodges 2001; Gu et al. 2004). More importantly, they give birth to tropical cyclones over the Atlantic Ocean (Landsea et al. 1998) and modulate their evolution and movement (Peng et al. 2006). Indeed, Thorncroft and Hodges (2001) have shown a

positive correlation between the AEW activity and Atlantic tropical cyclone activity, suggesting that hurricane activity may be influenced by the number of the AEWs leaving the west coast of Africa (see also Avila and Pasch 1992).

In this paper, we examine the effect of these synoptic-scale easterly waves on larger-scale precipitation of the marine ITCZ in two regional coupled model simulations with different atmospheric resolution. We explore how resolution affects the model's ability to capture the horizontal shear and low-level convergence of winds associated with the AEWs, and thus convection and precipitation processes. Analyses reveal that the amplitude of these waves is well simulated on both the coarse (1°) and fine ($\frac{1}{4}^{\circ}$) atmospheric grids. The cyclonic shear of the wind associated with waves on the finer grid, however, yields stronger near-surface convergence, triggers convection, and thus produces more intense precipitation. The rainfall variability associated with the easterly waves accounts for a significant fraction (>60-70%) of the total simulated variance in the marine ITCZ. As a result, simulation of the mean ITCZ improves and the seasonal phasing becomes more realistic.

The paper is organized as follows: in section 5.2, the description of the models and experimental designs are presented. In section 5.3, the sensitivity of the AEW-induced atmospheric convergence and precipitation due to model resolution is examined. In section 5.4, we discuss the impacts on the larger-scale mean climate in the model. Conclusions and discussion follow in section 5.5.

5.2 Models and Experiment Setup

The coupled model used for the present study is the Scripps Coupled Ocean-Atmospheric Regional (SCOAR) model (Seo et al. 2007). It combines two well-known, state-of-the-art regional atmosphere and ocean models using a flux-SST coupling strategy. The atmospheric model is the Experimental Climate Prediction Center (ECPC) Regional Spectral Model (RSM) and the ocean model is the Regional Ocean Modeling System (ROMS).

The RSM, originally developed at the National Centers for Environmental Prediction (NCEP) is described in Juang and Kanamitsu (1994) and Juang et al. (1997). The code was later updated with greater flexibility and much higher efficiency (Kanamitsu et al. 2005). Briefly, it is a limited-area primitive equation atmospheric model with a perturbation method in spectral computation, and utilizes a terrain-following sigma coordinate system (28 levels). The model physics are same as NCEP global seasonal forecast model (Kanamitsu et al. 2002a) and NCEP/ National Center for Atmospheric Research (NCAR) Reanalysis model (Kalnay et al. 1996) except for the parameterization of convection and radiative processes. The parameterization for atmospheric deep convection in the current version of the RSM used in this study is based on Relaxed Arakawa-Schubert scheme (Arakawa and Schubert 1974; Moorthi and Suarez 1992).

The ROMS solves the incompressible and hydrostatic primitive equations with a free surface on horizontal curvilinear coordinates and utilizes stretched generalized sigma coordinates in order to enhance vertical resolution near the sea surface and bathymetry.

The details of the model can be found in Haidvogel et al. (2000) and Shchepetkin and McWilliams (2005).

A flux-SST coupler bridges the atmospheric (RSM) and ocean (ROMS) models. The coupler works in a sequential fashion; the RSM and ROMS take turns integrating while exchanging forcing every 24 hr. The interacting boundary layer between RSM and ROMS is based on the bulk formula for surface fluxes of momentum, and sensible and latent heat adapted from the algorithm of Fairall et al. (1996). Since the grids of the atmosphere and ocean models differ, a simple linear interpolation is used to map the SST and ocean currents to the atmospheric physical-space grid and the resultant fluxes to the ocean grid. Care must be taken in choosing the land-sea mask near the coasts because the atmospheric model is spectral and Gibbs' phenomenon can result in unphysical structures in the surface flux forcing fields over the oceanic grid points adjacent to the coast. In each domain, the land-sea mask must be qualitatively optimized to reduce this effect of the mismatch between spectral-atmospheric and physical-space-oceanic models.

The low-wavenumber atmospheric flows from NCEP/Department of Energy (DOE) Reanalysis II (Kanamitsu et al. 2002b, hereafter RA2) are specified as a base field over the regional domain of the RSM. The RA2 is available in T62 spectral resolution on a global Gaussian latitude-longitude grid, at roughly 200 km grid size in the tropics. However, the effective resolution in the global spectral analysis is coarser than this estimated grid size, since one needs 5-6 grid points to accurately represent the smallest wavenumber in the global spectral model (Pielke 1991; Laprise 1992). Thus, wavelengths from circumglobal to 1000 km are well resolved in the original RA2 model. For downscaling purposes, Kanamaru and Kanamitsu (2007) designed a scale-selective bias

correction (SSBC) to reduce the tendency of wavenumbers longer than 1000 km to drift from the prescribed original RA2 large-scale fields that drive the regional response in RSM. This procedure is invoked in SCOAR, which encourages the large-scale components of AEW events to be similar for both coarse (e.g., RA2) and higher resolution (e.g., SCOAR) grids.

The AEWs discussed in this study have a typical wavelength of 2500 km (Reed et al. 1977) and thus, in SCOAR, they should resemble the waves in the base field from RA2. However, it should be noted that these waves are also substantially influenced by many processes such as meridional temperature gradient, soil moisture content, monsoonal processes, and the resolved orography (Cook 1999; Mekonnen et al. 2006), which can be modulated differently depending on the SCOAR resolution and its downscaling procedure. Therefore, the differences in the details of these waves in the SCOAR simulations shown in the later sections are, by the experimental design, largely due to changes in SCOAR model resolution.

Here we compare two SCOAR model simulations, where the atmospheric resolution is changed in a domain that covers the tropical Atlantic basin from 30°S to 30°N and from 70°W to 20°E, including eastern Brazil and western Africa. In the HL (High ocean-Low atmosphere) simulation, $\frac{1}{4}^{\circ}$ resolution is used for the ocean, but low resolution (1°) is used for the atmosphere. In HH (High ocean-High atmosphere), both the ocean and atmospheric models use $\frac{1}{4}^{\circ}$ resolution. Hence the only major difference in HL and HH is the horizontal resolution in the atmosphere. A minor difference in the two cases is in the altered land-sea mask linking the ocean and atmospheric models. The physical space fields of the atmosphere must be mapped to the oceanic grid (and vice

versa) via interpolation, which is sensitive to the details of the land-sea mask near the coastal ocean where large gradients of atmospheric fields often occur.

In a previous study, Seo et al. (2006) used similar SCOAR configurations to show that increasing oceanic resolution alleviates SST biases by 20%, especially in the African upwelling regions. In that study, they compared results from HL and LL simulations, where LL denotes low 1° resolution in both the ocean and the atmosphere. Despite the improvement in the ocean, the simulation of the mean ITCZ was only marginally improved, likely due to a coarse 1° horizontal resolution in the atmosphere. The present study is an extension of Seo et al. (2006), focusing on the importance of synoptic-scale processes in the atmosphere in altering the mean precipitation over the Atlantic Ocean.

The initialization and forcing procedures for both cases are as follows. The ROMS ocean was first spun up for 8 years with climatological atmospheric forcing and climatological oceanic boundary conditions. Then the SCOAR coupled run was launched for 7 years from 1998 to 2004 with low-wavenumber RA2 atmospheric forcing and climatological oceanic boundary conditions. The 6-year solution from 1999 to 2004 is analyzed in this study.

In this regional modeling framework, the remote influences on the simulated variability of the ITCZ (Chiang et al. 2002; Xie and Carton 2004) are the same in both SCOAR simulations. Chiang et al. (2002) show that the anomalous Walker circulation affects the precipitation over the tropical Atlantic, while the meridional gradient in SST determines the position of the ITCZ. Remote ENSO conditions affect both of these processes: the former through direct atmospheric influence (Dai and Wigley 2000) and the latter via atmospheric teleconnections, which change northern Hemisphere SST. In

the present SCOAR model configurations the large-scale atmospheric and oceanic forcings that drive these two mechanisms are nearly identical. But the regional variability simulated in HH and HL for the tropical Atlantic and western Africa may be different in each case, giving rise to differences in variability of SST and the ITCZ. For example, the meridional SST gradient is affected by local ocean-atmosphere-land coupled variability, independent of the remote forcing (Chang et al. 1997; Xie and Carton 2004). Local feedback processes, such as these, are of primary interest in this study.

5.3 AEW-induced low-level convergence and precipitation: Sensitivity to model resolution

African easterly waves are the dominant synoptic-scale weather disturbances during boreal summer months. These waves originate in eastern Africa (Mekonnen et al. 2006; Kiladis et al. 2006; Berry and Thorncroft 2005; Burpee 1972; Carlson 1969) and traverse the tropical Atlantic Ocean. We are interested in how AEW-induced wind-shear and convergence lead to large precipitation events within the marine ITCZ.

In order to illustrate the summertime background environments that foster the generation of the disturbances, Figure 5.1 compares the large-scale features between the model simulations and the RA2 during the summertime (July-August-September). Figure 5.1a-c shows wind fields at 700 hPa (the jet level) from the model simulations and RA2 over northern Africa and the eastern Atlantic Ocean. In RA2, the core of the AEJ at this level is identified as a maximum of the easterly wind present on the west coast of Africa at 15°W , 15°N , where wind speed reaches 10 m s^{-1} . The width of the jet is about 10° in

latitude and the axis of the jet extends eastward over the continent with an apparent southward shift (Cook 1999). These observed wind structures are well reproduced in both regional simulations, although the models produce stronger jets than RA2. The spatial patterns of the jet are qualitatively similar in both simulations, although the jet in HH is slightly stronger than HL at the core over western Africa. The meridional gradient of vorticity at the jet level (Figure 5.1d-3) and the near-surface potential temperature (Figure 5.1g-h) are largely similar in HH and HL, indicating that barotropic and baroclinic instability conditions that support the formation of the jet (Charney and Stern 1962; Burpee 1972) are similar for both 1° and $\frac{1}{4}^{\circ}$ atmospheric resolution. The simulated positive 925hPa potential temperature gradient over northern Africa (Figure 5.1g-h) compares well with RA2 (Figure 5.1i) and the previous study (e.g., Pytharoulis and Thorncroft 1999). The model relative vorticity on the 700hPa surface (Figure 5.1d-e) is also qualitatively similar to the observed potential vorticity on the 315K isentropic surface (Figure 4 of Pytharoulis and Thorncroft 1999), exhibiting a negative vorticity gradient near and north of the jet and a positive vorticity gradient south of the jet.

Figure 5.2 shows the variance of summertime synoptic-scale (2-6 day) 850 hPa meridional winds for each simulated year over the Atlantic Ocean where the variance is large. The 2-6 day band-pass filtering to highlight the AEW-signals in meridional wind field was previously used by Albignat and Reed (1980) and Mekonnen et al. (2006). Except for the summer of 1999 when they are nearly equally strong, AEW variance over the ocean is stronger in HH than in HL, with mean variance being 20% larger in the higher resolution case. The standard deviation of the meridional winds is therefore only slightly (~4-5%) stronger in HH than HL. An f-test indicates that the difference in

variance in HH and HL is not statistically different (at 95% significance level). Thus both higher and coarser resolution simulations yield statistically similar amplitudes of the AEWs over the tropical Atlantic Ocean. The strikingly different features between the two simulations that emerge from the similar environments associated with the waves are the associated near-surface convergence and the precipitation, which is discussed later.

In order to investigate and compare the details of the simulated wave structure and its propagation, Figure 5.3 presents Hovmöller diagrams of 2-6 band-pass filtered 850 hPa winds for JAS of 2003 when the difference between HH and HL was largest (Figure 5.2). The simulated AEWs from HH (Figure 5.3a) and HL (Figure 5.3b) exhibit wave characteristics consistent with the observed estimates by the synoptic map analysis of Carlson (1969), the compositing study of Reed et al. (1977), and the synoptic map analysis of Burpee (1972), all of which found typical wavelengths of 2000-4000 km, periods of 3.2–3.5 days, and phase speeds of $\sim 8 \text{ m s}^{-1}$. The simulated phase of the waves is similar between the model simulations, and also with the observations.

These large amplitude waves propagate well beyond the eastern Atlantic, traversing the Atlantic Ocean and reaching the Caribbean and western boundary of the model domain. Previous studies have reported that they often propagate beyond the Caribbean across Central America into the eastern Pacific basin (Frank 1970), where they contribute to tropical cyclogenesis (Avila and Pasch 1992). Over the tropical Atlantic Ocean, strong cyclonic shear of the horizontal winds associated with the large amplitude of these waves is accompanied by localized intense precipitation (contours overlaid in Figure 5.3a), implying a tight connection between wind shear generated by AEWs and strong precipitation (Thorncroft and Hodges 2001). Early analyses by Frank (1970) and

Burpee (1972) concluded that the easterly waves account for about half of the tropical cyclones in the Atlantic Ocean. Figure 5.3a suggests that the heavy precipitation events in this model are associated with simulated tropical cyclones, which were formed within the environment favored by the easterly waves in the model. On the other hand, despite the reasonably well-simulated AEWs in HL, there are few heavy precipitation events compared to those that occur with the strong wind shear in HH (the contours of Figure 5.3b). [Note that RA2 does not assimilate precipitation (Kanamitsu et al. 2002) so that individual precipitation events may or may not correspond to observations.]

The heavy precipitation events in HH in the region of high cyclonic shear in the easterly waves are closely related to the markedly enhanced near-surface convergence. Figure 5.4 presents the same plot of meridional winds as in Figure 5.3, but overlaid with the 2-6 day filtered convergence of the 10-m winds diagnosed from the model and RA2. First of all, the coarse grid of RA2 leads to virtually zero near-surface convergence, which does not allow comparison with the model results. In HH, strong convergence occurs within the region of high-shear of easterly waves, which is in phase with the heavy precipitation seen in Figure 5.3a. The in-phase relationship also occurs in HL, although the estimated convergence is generally weaker, producing weaker precipitation (in Figure 5.3b).

The association among the cyclonic wind shear of the easterly waves, near-surface convergence, and the enhanced precipitation events shown in Figures 5.3 and 5.4 can be better illustrated in the selected yet representative example in Figure 5.5. It shows the two-day averaged fields of model rainfall, convergence of 10-m winds, and outgoing longwave radiation (OLR) during August 31 - September 1, 2003, a period of strong

AEW activity and intense precipitation (Figure 5.3). Note that this time period corresponds to the development of Hurricane Fabian in observations in this region of the tropical Atlantic as provided by the National Hurricane Center. Model tropical storms do not necessarily follow observations closely, however, since the path and intensity of model mesoscale disturbances are free to evolve without constraint due to dynamical instability processes, which are sensitive to initial conditions.

During this particular period, the large wave amplitudes shown in Figure 5.3a,b are due to tropical cyclones (or depressions) located near 50°W , 13°N and 20°W , 7°N in HH and HL. The cyclone simulated in HH produces massive precipitation of more than 200 mm day $^{-1}$ and is associated with a local minimum of OLR, which indicates that precipitation occurs through a convective process. This convective precipitation in the cyclone is in turn associated with the strong low-level convergence that exceeds $6 \times 10^{-5} \text{ s}^{-1}$ at the core. In HL, on the other hand, weaker convergence of less than $3 \times 10^{-5} \text{ s}^{-1}$ causes weaker convection and thus less rain of only 30 mm day $^{-1}$.

Heavy rainfall exceeding 200 mm day $^{-1}$ captured by HH is an observed phenomenon. Lonfat et al. (2004), for example, reported that a maximum rainfall rate of 288 mm day $^{-1}$ is observed for category 3-5 systems of hurricanes using the Tropical Rainfall Measuring Mission (TRMM) microwave imager rain estimates. Observations of rainfall rate measured from moored buoys agree with this as well. Figure 5.6a shows time-series of rainfall measured at the PIRATA (Pilot Research moored Array in the Tropical Atlantic) buoy moored at 4°N - 38°W and from the model grid at the mooring site. In both models and observations, the variability of rainfall is markedly larger than its mean. The standard deviation (std) of rainfall in the observations is roughly 7 times

greater than its mean, while in HH (HL), the std is 2.5 (1.7) times larger than its mean. The strongest peak in the observations at this particular site during this period reaches 914 mm day⁻¹. Statistically, the means of HH and HL are both consistent with PIRATA, but the variability in HH is clearly more realistic than in HL. The map of std of rainfall (not shown) reveals that, in a large area around this mooring site, the std of HH rainfall is greater than 25 mm day⁻¹, while HL has everywhere a std less than 10 mm day⁻¹. Thus, the chosen mooring site is a typical location within the ITCZ where variability in rainfall well exceeds its mean. The probability distribution functions (PDFs) of observed rainfall (Figure 5.6b) confirms that several peaks produce extremely high precipitation in the observations. Although HH rainfall does not display peaks as strong as in the observations, the extreme cases shown in HH compares better with the observations. This indicates that increasing model resolution can enhance heavy precipitation events, which skew the rainfall distributions towards longer tails.

Biasutti et al. (2006) have shown that most of the atmospheric general circulation models (AGCMs) underestimate the high-frequency variability of the rainfall within the marine ITCZ and thus exhibit a reduced range in daily precipitation there. The observed rainfall distribution, on the other hand, extends to higher rainfall values with shorter decorrelation time-scales (~1 day). Figure 5.6 indicates that HL resembles the typical case of these AGCMs, while HH emulates the observed distribution of daily precipitation.

The heavy precipitation events are closely related to the convergence fields (Figure 5.4), which are better resolved on the higher-resolution atmospheric grid. This relation is illustrated in Figure 5.7. It shows PDFs of convergence for the 10-m wind

computed from the models in comparison with the estimate from the QuikSCAT winds over 2000-2004, averaged over the ITCZ (2°N - 7°N and 40°W - 30°W). Both model runs exhibit the slight skewness towards convergence as in the observations, implying large-scale convergence within the ITCZ. Yet, convergences greater than $6 \times 10^{-5} \text{ s}^{-1}$ are found only in the observations and in HH. On the other hand, the convergence does not exceed $6 \times 10^{-5} \text{ s}^{-1}$ in HL for any event during this 5-year period in this region. The propensity for even higher convergence is observable in QuikSCAT winds, and HH is clearly better than HL when compared with the QuikSCAT.

Easterly waves are large-scale atmospheric processes (wavelengths of 2000-4000 km) and thus, compared to the $\frac{1}{4}^{\circ}$ resolution in HH, the 1° atmospheric resolution should be sufficient to resolve the wave activity reasonably well. Indeed, the simulated 6-year mean variances of the wind were not statistically different. Furthermore, Figures 5.3 and 5.4 suggest that the related cyclonic wind shear is well simulated on both grids. However, compared to the 1° grid, it rains more, and with a far more realistic distribution, on the $\frac{1}{4}^{\circ}$ grid. The lack of rain in HL despite the reasonably well-resolved AEWs implies that wind convergence and subsequent convection are important processes in order to produce a realistic mean precipitation pattern. At $\frac{1}{4}^{\circ}$ resolution, we approach the horizontal scales of convection and are nearly able to resolve the observed low-level convergence (Figure 5.7).

This result can be anticipated from the idealized study of Pauluis and Garner (2006) on the impacts of the horizontal resolution on the statistics of the atmospheric convection. They demonstrate a close connection between the horizontal resolution of the cloud resolving model and the statistical properties of the deep convective towers. They

find a significant improvement in the simulation of vertical velocity and convection (and thus perhaps the low-level convergence) when they transit from coarse 50 km to finer 16 km horizontal resolutions.

The close connection between convergence and the convection is supported by the recent study of Biasutti et al. (2006). They show the importance of dynamic lifting in the deep convection of the marine ITCZ, which allows the observed maximum ITCZ precipitation to be positioned over the region of the maximum near-surface convergence rather than the maximum SST. Most of the AGCMs, on the other hand, are shown to be overly sensitive to the thermodynamic convective available potential energy over warm SST, yielding a tendency to locate the maximum ITCZ rainfall over the local maximum SST.

5.4 Impacts on the larger-scale mean precipitation and SST

5.4.1. Mean and Seasonal Cycle of the ITCZ

Synoptic precipitation events associated with the easterly wave convergence and convection contribute a significant fraction of the total rainfall variability. Figure 5.8 shows the ratio of the variance of 2-6 day filtered rainfalls to the total variance. Within the marine ITCZ, synoptic scale precipitation accounts for 40-60% of the total variance in HL. This high ratio in HL is striking, indicating that more than half of the total rainfall variability originates from the synoptic scales. The RA2 has a similar percentage of the variance associated with synoptic events (Figure 5.8c), suggesting that this 40-60% contribution to rainfall variability in the marine ITCZ may be an upper limit from the synoptic scale variability on the coarser grids. In HH, however, the ratio rises to more

than 60-70%, suggesting that a substantial fraction of the total rainfall variability is indeed determined by the synoptic-scale heavy rainfall events associated with the easterly waves.

The fact that a significant fraction of rainfall variance is explained by synoptic-scale variability implies that there will be a net contribution to the larger-scale mean rainfall in the model. Figure 5.9 shows 6-year mean precipitation from 1999-2004 from the model in comparison with the observational estimates from the Global Precipitation Climatology Project (GPCP, Xie and Arkin 1997) for the corresponding period. Precipitation from both observations and the model shows the ITCZ (as described in Chiang et al. 2002) as a zonally tilted (northeast-southwest) structure over the open ocean with maximum rainfall between the equator and 10°N. Although the HH model tends to produce more rain within the marine ITCZ than the observations, the figure demonstrates that the rainfall simulation in HH is improved compared to HL. Precipitation over the open ocean in HH is about 9 mm day⁻¹, much closer to the observed rainfall of about 8 mm day⁻¹. On the other hand, rainfall in HL is only 4 mm day⁻¹.

Figure 5.10 illustrates the seasonal variation of the location of maximum precipitation in the model and observations, representing the seasonal migration of the ITCZ. Generally, the location of the ITCZ is well reproduced in the model during most of the year except for the boreal spring season. During boreal spring months, from February to May, the ITCZ in HL crosses the equator into the Southern Hemisphere, while the ITCZ in HH stays north of the equator throughout the year, which is consistent with the observations (Chiang et al. 2002). It is clear that not only the mean rainfall but also the seasonal cycle of the ITCZ is better simulated in HH than in HL.

5.4.2. Large-scale SST distribution

This section investigates the role of large-scale mean SST and its relation to the improved ITCZ simulation. Figure 5.11a shows the 6-year mean SST for HH, and the mean difference with HL (HH minus HL) is presented in Figure 5.11b. Also shown are (HH minus HL) difference maps of 6-year mean surface winds, net surface heat flux, latent surface heat flux and surface radiative flux. The change in SST when increasing the resolution (Figure 5.11b) shows a notable basin-scale open-ocean cooling of $\sim 0.5^{\circ}\text{C}$ in the extratropics in both hemispheres, little change near the equator (5°S - 5°N), and coastal warming (up to 2°C) along the west coast of Africa. The cooling in the extratropics and warming along the coast are both damped by the net surface heat flux (Figure 5.11d). On the other hand, SST does not change along the equator, implying the presence of an altered oceanic heat flux at the ocean surface, which balances the thermodynamic cooling. The altered total surface heat flux along the equator is a result of both evaporative cooling by enhanced southeasterly winds (Figure 5.11c) and radiative cooling by increased cloudiness (not shown). In HH, both hemispheres have enhanced trade winds that support the large-scale convergence into the ITCZ, which is significantly stronger even though the mean position of the ITCZ remains nearly the same in HH and HL (Figure 5.9).

Figure 5.12 shows the seasonal cycles of monthly averaged SST in the extratropics for both hemispheres in the regions where the SST was colder in HH. Both in the northern and southern hemispheres, the SSTs in HH are persistently colder than HL throughout the annual cycle. The seasonal cycle of the position of ITCZ (Figure 5.10) is

sensitive to the seasonal variability of the meridional (inter-hemispheric) gradient of SST through the modulation of meridional surface pressure gradient and the near-surface winds (Hastenrath and Greischar 1993). The seasonal cycle of the anomalous meridional SST gradient is computed as the difference in anomalous SST between the northern and southern regions defined in Figure 5.12a,b. Chiang et al. (2002) defined the tropical Atlantic gradient index in a similar way (albeit using zonally integrated SST instead of using a box) to describe the relation among the meridional SST gradient, the near-surface winds, and the precipitation in the ITCZ. Figure 5.12c shows that the seasonal cycles of the simulated meridional SST gradients are almost indistinguishable, albeit weaker than the observed estimate. The gradients look similar in the model simulations because the open-ocean SST cooled by roughly the same amount in both hemispheres in HH.

The debate still continues about whether the meridional SST gradient and the large-scale convergence determine the rain in the ITCZ or whether the wind convergence is determined by mid-tropospheric heating and hence the rainfall in the ITCZ. Gill (1980) argues for the latter, whereas Lindzen and Nigam (1987) favor the former. Figure 5.11 suggests that Gill (1980) is more relevant in the current model because the meridional SST gradient did not change in the simulations; this implies that the enhanced southerlies in HH are forced by the larger-scale, stronger ITCZ.

Enhanced southerlies across the equator will have dynamical consequences for the ocean. The details of mixed layer heat budget calculations can reveal the dynamical and thermo-dynamical balances in SST, mixed layer depth and net surface heat and freshwater fluxes. Such an analysis is beyond the scope of this paper and will be reported elsewhere.

The warming along the west coast of Africa in Figure 5.11a deserves some attention. It is likely that the coastal warming in HH is simply due to the altered near-coastal winds, which drive reductions in upwelling and open-ocean Ekman advection of SST gradients. However, the details of the atmospheric land-sea mask are very different in the HL and HH cases, due to the enhanced resolution in HH. Since an interpolation/extrapolation scheme is used to map the atmospheric fields to the oceanic grids, the small-scale structures in the HH land-sea mask play an important role in establishing the near-coastal alongshore upwelling/downwelling wind fields. In the both HL and HH, the land-sea mask was qualitatively optimized to attempt to reduce the mismatch between oceanic and atmospheric grids and the misrepresentation of fluxes due to spectral truncations errors (Gibbs phenomenon). But it is not completely clear whether a different interpolation scheme for HH and HL (and/or a smoother land-sea mask) would result in similarly warmer SST along the coast in case HH. Nonetheless, this study focuses on the *basin-scale* SST changes and its meridional gradient, not the changes in SST concentrated in the narrow band along the coast, which appear to be too localized to generate the basin-wide effects.

5.5 Conclusions and Discussion

A regional coupled climate model has been configured for the tropical Atlantic in the present study to explore the climatic importance of synoptic-scale atmospheric disturbances originating from the African continent. The analyses have shown that these synoptic-scale easterly waves are reasonably well simulated in the model with similar strengths both on 1° and $\frac{1}{4}^\circ$ atmospheric grids. The simulated wave characteristics,

including their amplitudes, are comparable between the model simulations, and the phases of the waves are similar to those of the RA2 fields that drive the regional models.

Strong cyclonic shear of the wind is generated in the easterly waves both in HH and HL, although this wind shear is accompanied by heavy precipitation events only in HH, not in HL (Figure 5.3). This is because the computed convergence in HH is much larger than in HL (Figure 5.4), which leads to stronger convection and heavier precipitation (Figure 5.5 and 5.6). This propensity for higher convergence in the high-resolution case compares well with QuikSCAT observations of winds and clearly represents an improvement over the low-resolution case (Figure 5.7).

The climatic importance of AEW-related convergence and convection processes is that they can lead to a more realistic model precipitation climatology and seasonality over the Atlantic Ocean (Figure 5.9 and 5.10). The occurrences of extreme rainfall events are much more realistic in HH, and resemble rainfall measurements from the PIRATA buoy. These heavy rainfall events, occurring on the 2-6 day time scales associated with the easterly waves, account for a significant fraction (>60-70%) of the simulated variance of precipitation (Figure 5.8), which implies a considerable alteration of the larger-scale annual mean rainfall due to these heavy rainfall events.

This improvement in the simulation of mean precipitation and the seasonal migration of ITCZ in the SCOAR model does not appear to be directly related to changes in the mean meridional SST gradient, which remain the same in both HH and HL (Figure 5.11, 12). The location of the ITCZ is largely well captured in both simulations, but the convection associated with the AEWs in HH enhances the precipitation, which yields a

more realistic ITCZ. This results in enhanced cross-equatorial southerlies, which leads to stronger large-scale convergence into the ITCZ (Gill 1980).

The details of the AEWs including the mechanism(s) of generation, life cycle, and the connection to the convection and hurricanes are not fully understood despite their important role in regulating precipitation and regional climate (Thorncroft et al. 2003; Mekonnen et al. 2006). The resultant small-scale atmospheric convergence and convection processes cannot be realistically resolved in the coupled GCMs that are used for climate prediction in this region primarily due to the coarseness of the atmospheric grids. As a result, these models commonly exhibit large systematic errors in the tropical Atlantic Ocean (Davey et al. 2002) and over western African nations (WCRP 2000). Our study here proposes that these climate models require higher horizontal resolution for better capturing the observed scale of convergence and convection. Higher horizontal resolution allows heavier precipitation events in the model that skew overall rainfall distributions towards longer tails, which can alter the mean large-scale climate in this region.

One of the foci of the international project called the African Monsoon Multidisciplinary Analysis (AMMA, Redelsperger et al. 2006) is to understand western African climate variability on multi-spatial/temporal scales and its complex interactions in the western African region. On the atmospheric mesoscale, the AMMA aims to study the typical rain-producing processes associated with the synoptic easterly waves and the African easterly jet, and their connection to the larger-scale climate variability. The current study directly addresses this issue by substantiating that 1) the transient synoptic-scale easterly waves that capture cyclonic wind shear and 2) the fine horizontal resolution

that facilitates low-level convergence and convection are both essential to climate models in order to generate realistic and much improved mean precipitation climatologies.

5.6 Acknowledgments

The text of this chapter, in full, is a reproduction of the material as it appears as Seo, H., M. Jochum, R. Murtugudde, A. J. Miller, and J. O. Roads, Precipitation from African Easterly Waves in a Coupled Model of the Tropical Atlantic Ocean, accepted, 2007. The dissertation author was the primary investigator and author of this paper. The coauthor listed in this publication directed and supervised the research which forms the basis for this chapter.

This research was partially funded by NOAA Grant, ‘Impact of oceanic mesoscale variability on the coupled climate’. We gratefully acknowledge additional funding support from DOE (DE-FG02-04ER63857) and NOAA (NA17RJ1231 through ECPC). The views expressed herein are those of the authors and do not necessarily reflect the views of these agencies. We thank the two anonymous reviewers for their comments and suggestions, which substantially improved the manuscript. We also thank Joe Tribbia, Phil Rasch, Masao Kanamitsu and Hideki Kanamaru for stimulating discussions and Stephen Yeager for providing the QuikSCAT daily wind product. The Center for Observations, Modeling and Prediction at Scripps (COMPAS) provided indispensable computer time. The Tropical Rainfall Measuring Mission (TRMM) Microwave Imager (TMI) SST data were obtained from the Web site of Remote Sensing Systems at <http://www.ssmi.com>. The GPCP precipitation and NCEP/DOE Reanalysis II were provided by the NOAA/OAR/ESRL PSD, Boulder Colorado, USA, from its Web site at

<http://www.cdc.noaa.gov>. The PIRATA data were obtained from the Web site of NOAA PMEL at <http://www.pmel.noaa.gov/tao>.

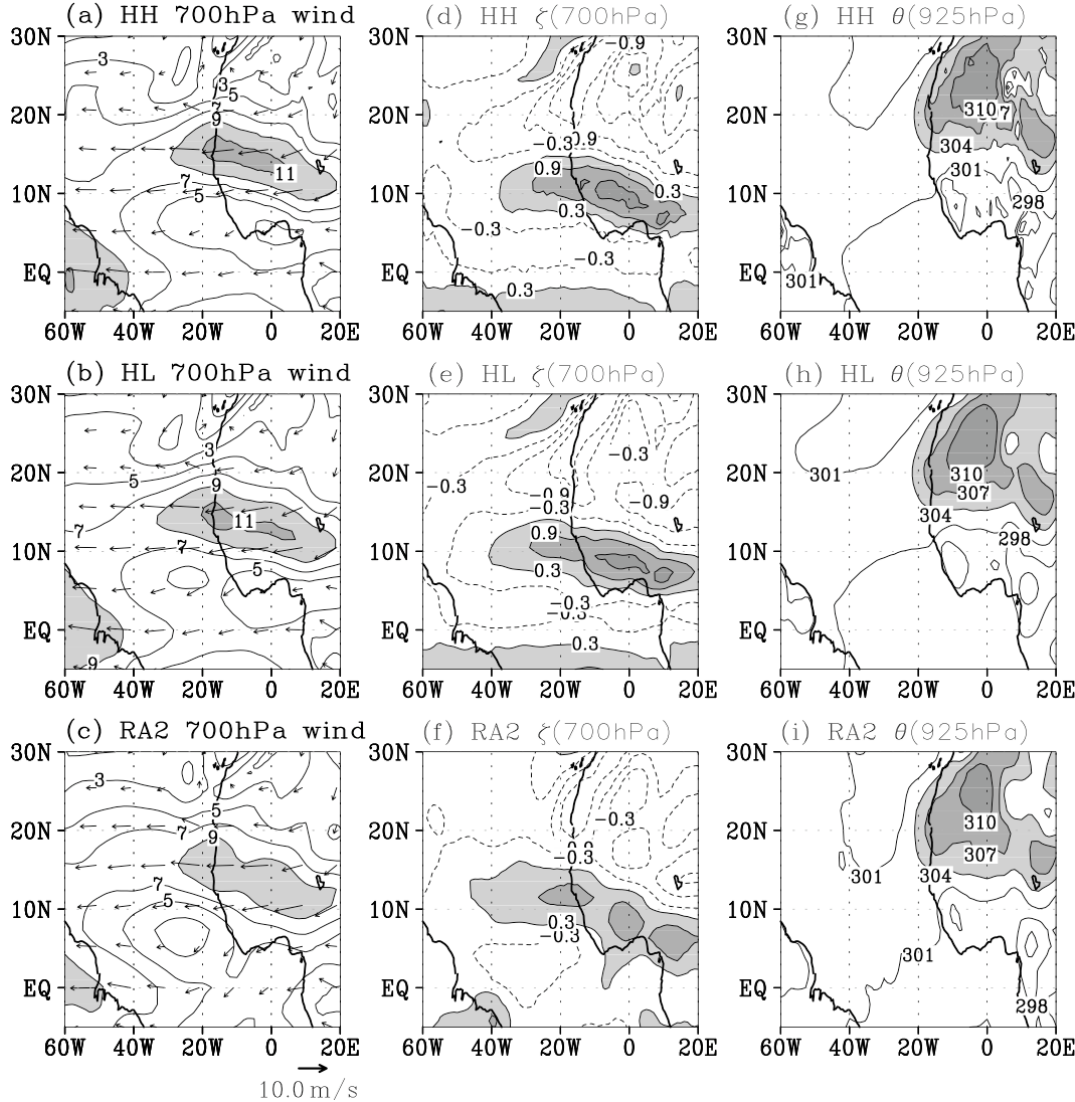


Figure 5.1 Six-year summertime (July-August-September) mean (a-c) wind speeds and vectors at 700 hPa (shaded when greater than 9 m s^{-1}), (d-f) 700 hPa relative vorticity (shaded when greater than 0.3 s^{-1}), and (g-i) 925 hPa potential temperature (shaded when greater than 304K). (top) HH, (middle) HL, and (bottom) NCEP/DOE Reanalysis II (RA2). HH in the top panel and RA2 in the bottom panel are interpolated to the grids on HL.

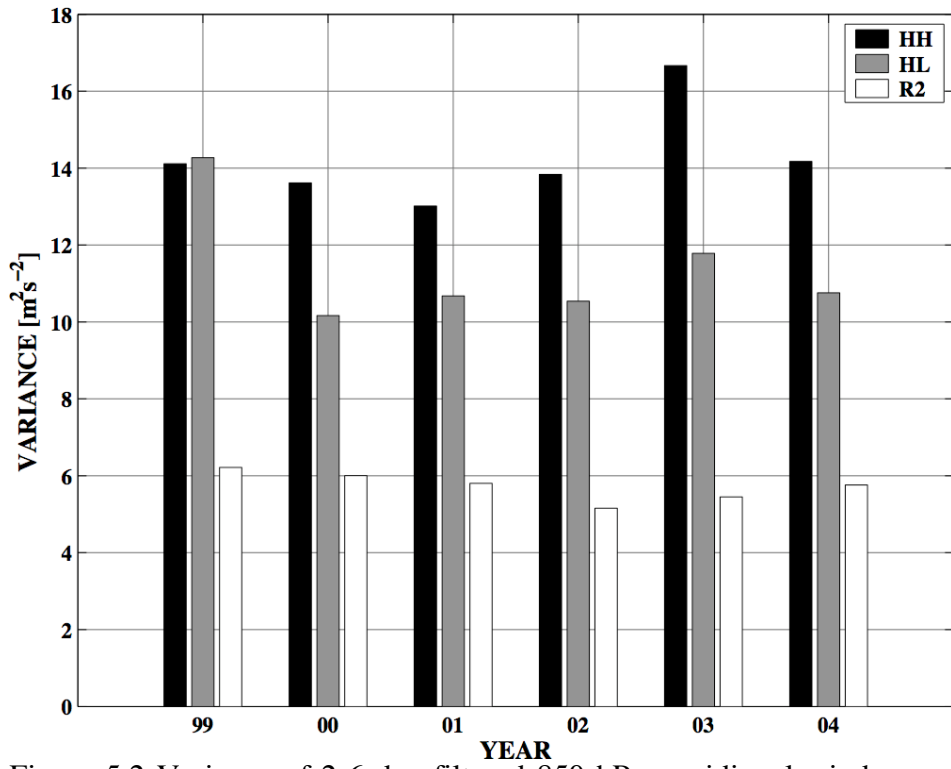


Figure 5.2 Variance of 2-6 day filtered 850 hPa meridional wind averaged over 55°W-15°W and 5°N-15°N for summer months (JAS) for 1999-2004 for (black) HH, (gray) HL and (white) RA2. The mean variance in HH, HL, and RA2 is 14.2, 11.3, and $5.7 \text{ m}^2 \text{ s}^{-2}$, respectively.

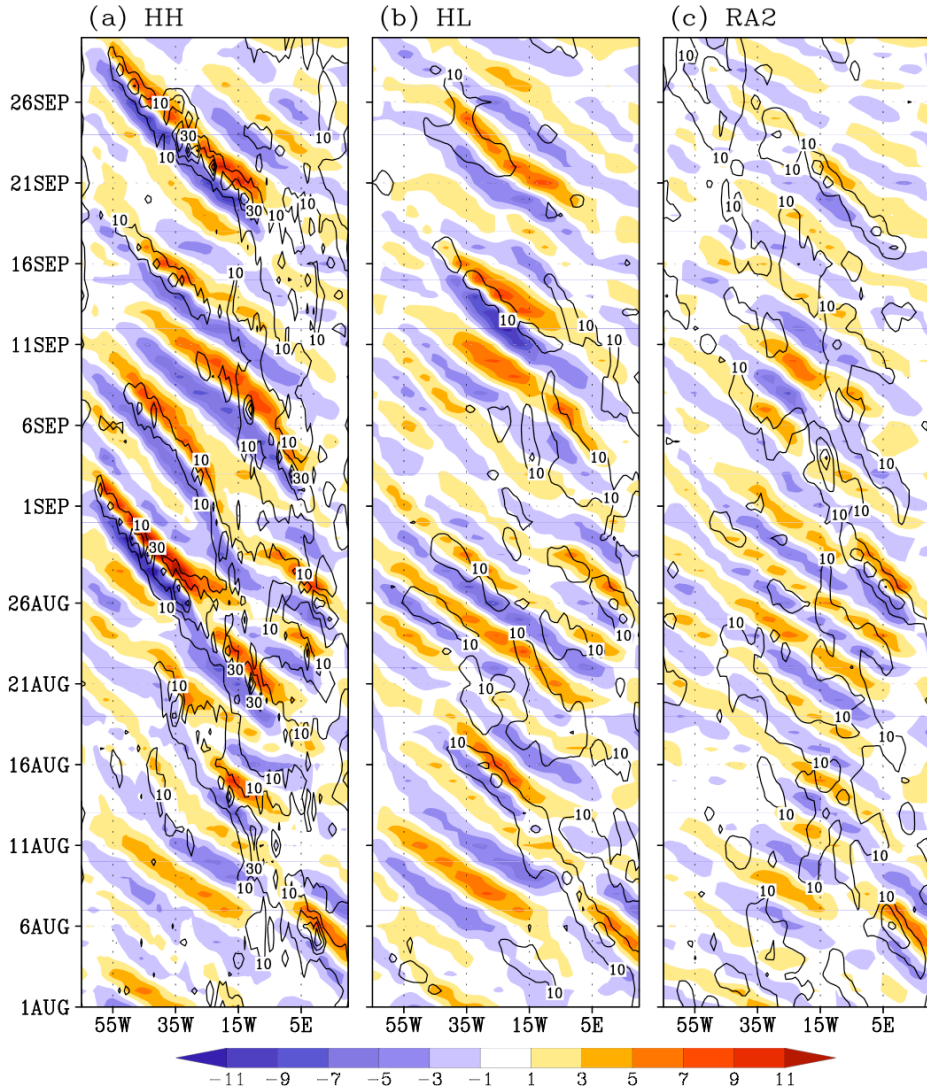


Figure 5.3 Hovmöller diagrams of 2-6 day filtered meridional wind (m s^{-1}) at 850 hPa averaged between 5°N - 15°N for August-September 2003 from (a) HH, (b) HL, and (c) RA2. Overlaid with the winds are the contours of unfiltered rainfall (mm day^{-1} , contours=10, 30, and 50 mm day^{-1}) for the same period. [Note that RA2 does not assimilate precipitation (Kanamitsu et al., 2002b) so that individual precipitation events may or may not correspond to observations.]

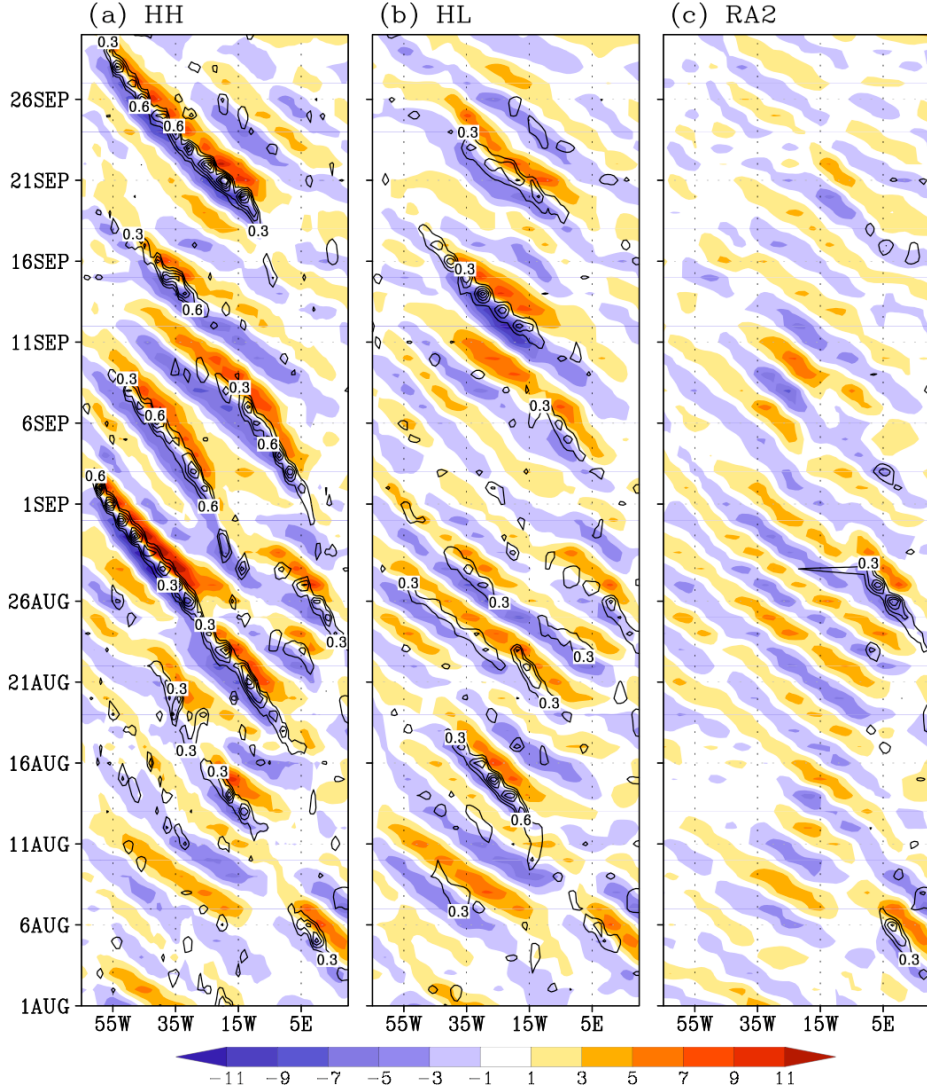


Figure 5.4 Same as in Figure 5.3 except overlaid with the contours of 2-6 day filtered near-surface convergence (10^{-5} s^{-1}), which were computed from 10-m winds. Only convergence is contoured (CI=0.3 with the zero contours omitted). Note the coarse grid of RA2 leads to generally zero near-surface convergence, which does not allow comparison with the model results.

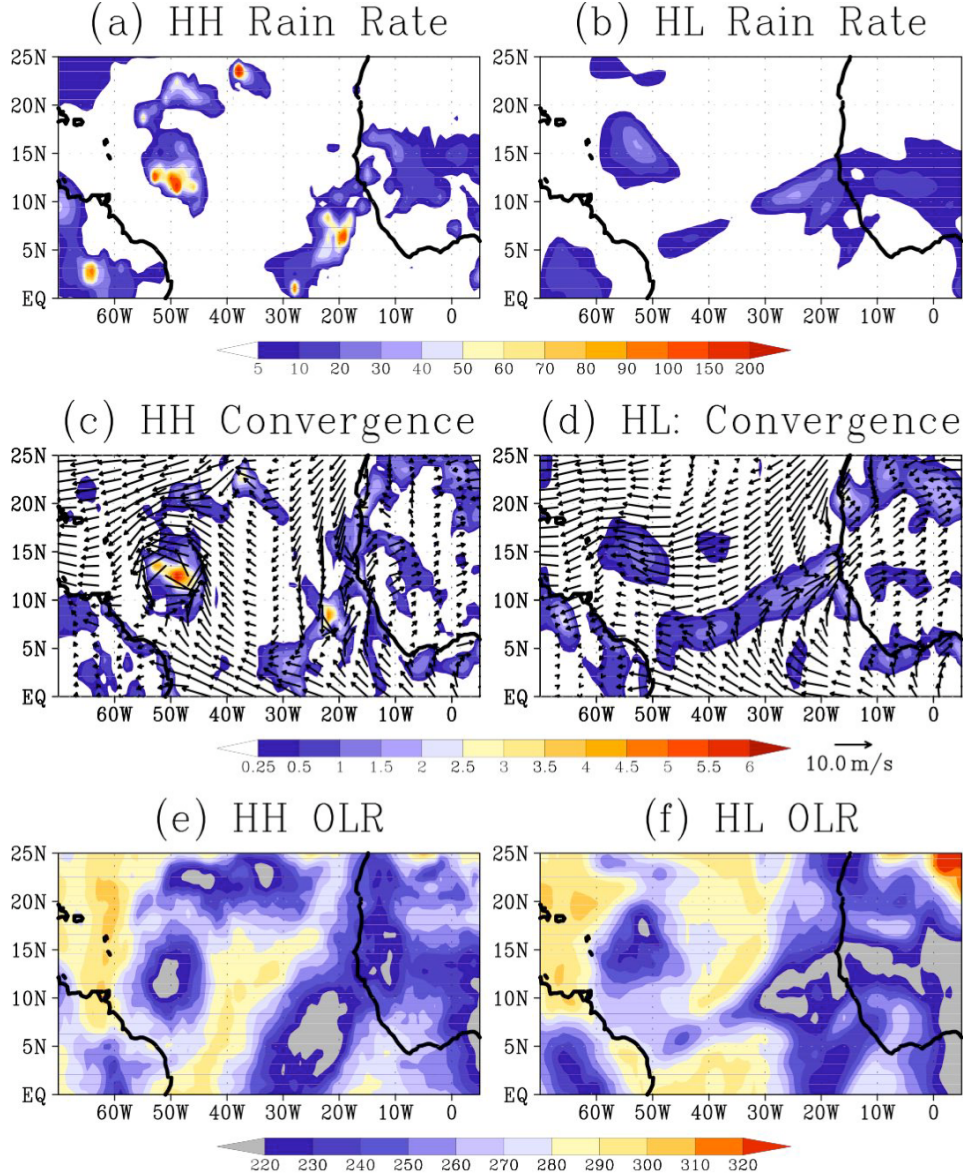


Figure 5.5 Two-day averages (August 31 – September 1, 2003) of (top) rainfall (mm day^{-1}), (middle) near-surface convergence (10^{-5} s^{-1}) of 10 m winds and the wind vectors (m s^{-1}), and (bottom) outgoing longwave radiation (OLR, W m^{-2}) from (left) HH and (right) HL. Only convergence is plotted in (c) and (d) for clarity. OLR less than 220 W m^{-2} in (e) and (f) is plotted in gray and represents strong atmospheric convection.

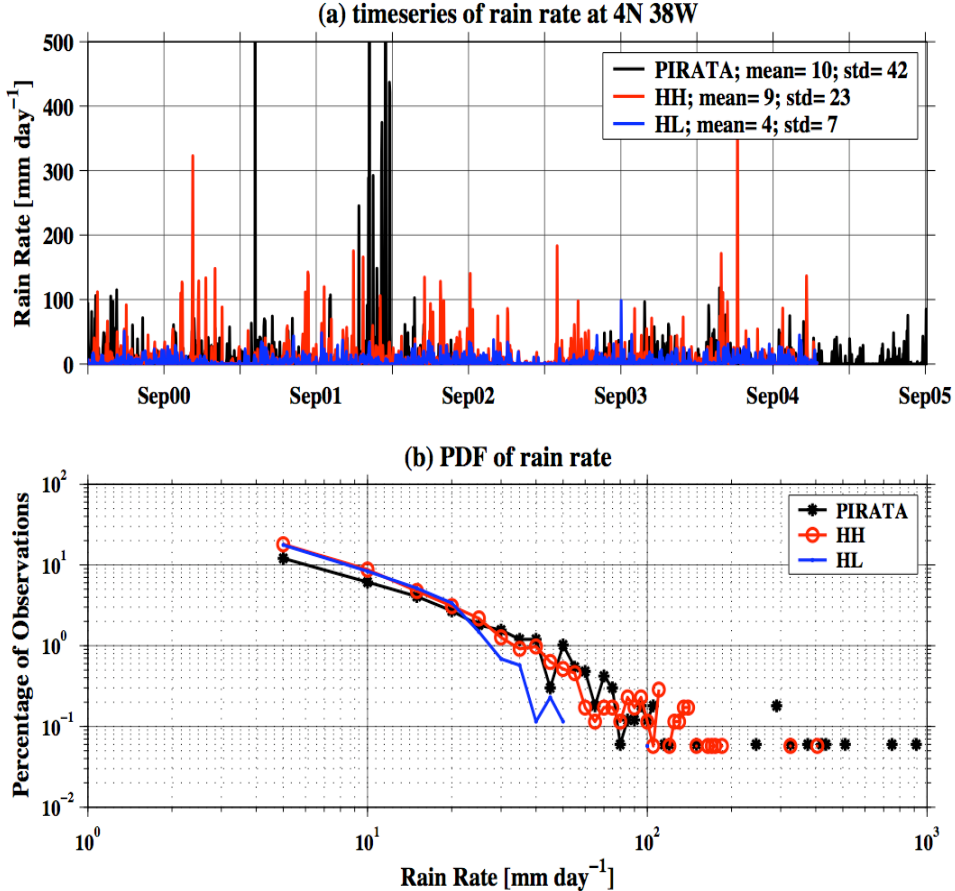


Figure 5.6 (a) (black line) Time-series of rainfall measured from the PIRATA mooring site at 4°N , 38°W from March 2000 to September 2005. There is a gap in the observations from mid-August 2002 to late August 2003, and no interpolation has been done in computing the mean and std. Model rainfall is shown red (HH) and blue (HL) at the nearest grid point to the mooring site. Mean and standard deviations are shown in the upper right corner of the plot. For the purpose of display, the y-axis is limited to 500 mm day^{-1} . There are three occasions in the observations, where the rainfall exceeds the limit of this plot. The precipitation amounts on these three days are 508 mm day^{-1} on April 24, 2000, 751 mm day^{-1} on January 22, 2001, and 914 mm day^{-1} on March 2, 2001. (b) Same as in (a), except for the probability distribution functions of the observed and simulated precipitation (shown in log-scales).

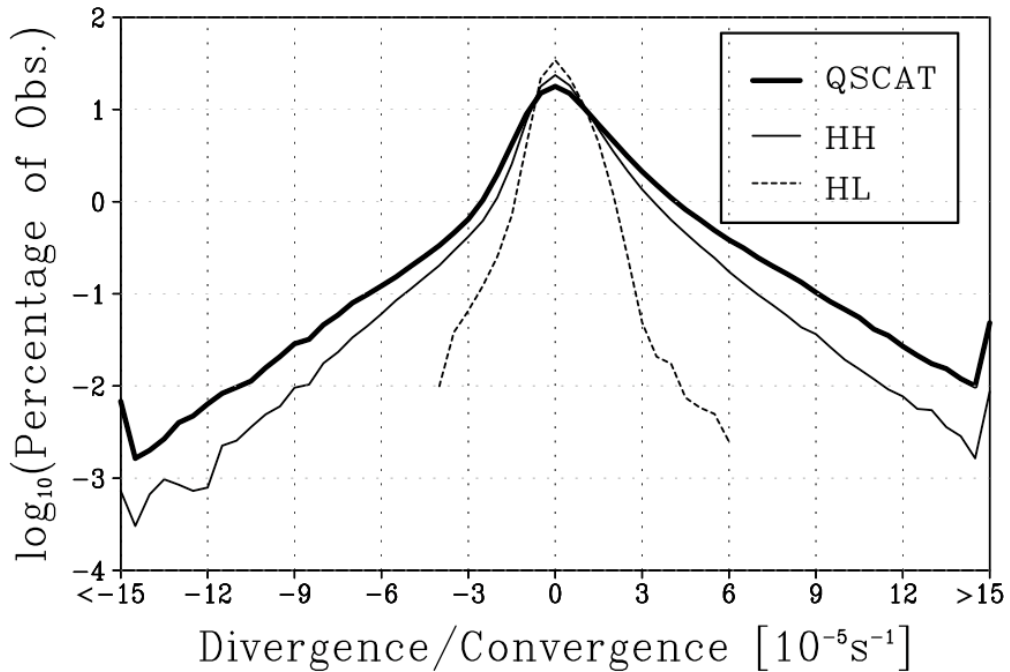


Figure 5.7 Probability distribution functions of 10 m wind convergence from (thick solid line) the QuikSCAT, (thin solid line) HH, and (thin dashed line) HL, from 2000 to 2004 over 2°N-7°N and 40°W-30°W. Note the y-axis is shown in logarithmic scale in order to highlight the difference at the higher ends. The positive (negative) values are convergence (divergence).

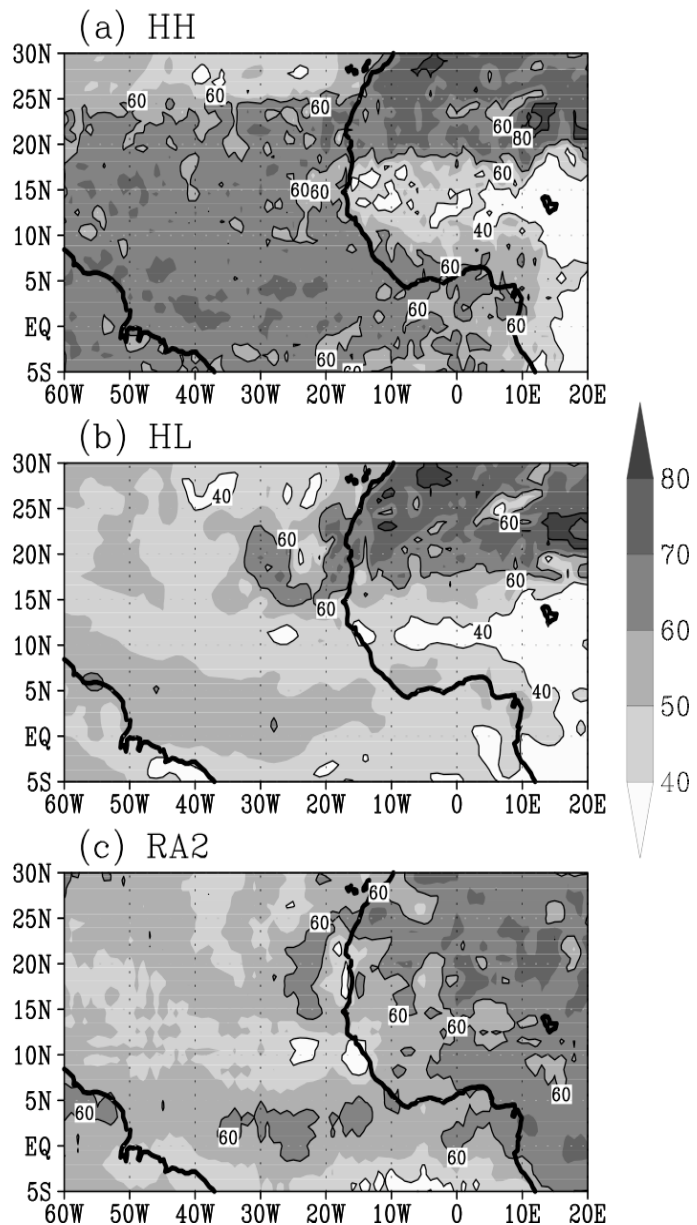


Figure 5.8 Ratio (%) of variance of 2-6 band-pass filtered rainfall to the variance of the total rainfall from (a) HH, (b) HL, and (c) RA2 averaged from 1999 to 2004. Contours shown are 50%, 60% and 70%. The variances are computed for all seasons.

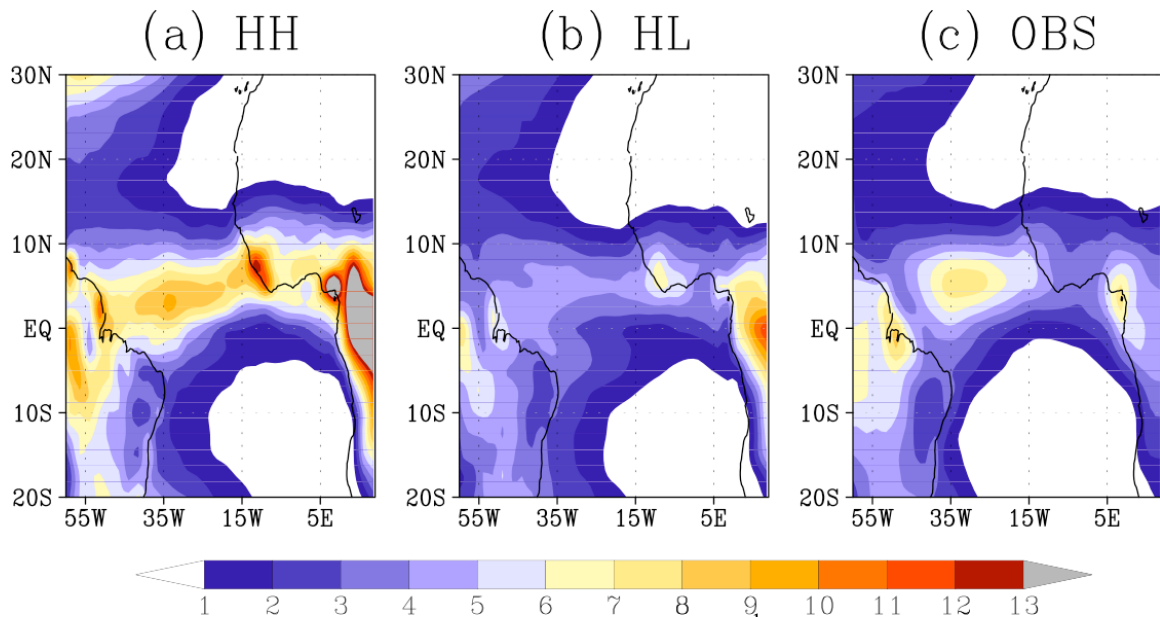


Figure 5.9 Six-year (1999-2004) mean rainfall (mm day^{-1}) from model; (a) HH, (b) HL, and (c) the observations from the Global Precipitation Climatology Project (GPCP). The model precipitation in (a) and (b) is re-gridded to the GPCP grids at $2.5^\circ \times 2.5^\circ$. Precipitation greater than 13 mm day^{-1} is shaded in gray.

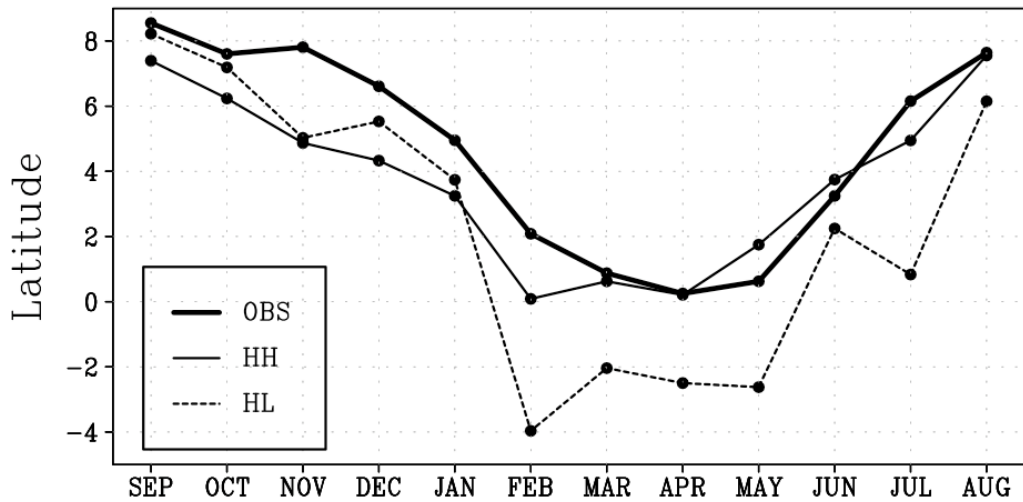


Figure 5.10 The seasonal variation of latitude of the maximum precipitation averaged between 50°W - 20°W from the 6-year (1999-2004) monthly averages for (thick solid) the GPCP precipitation, (thin solid line) HH, and (thin dashed line) HL.

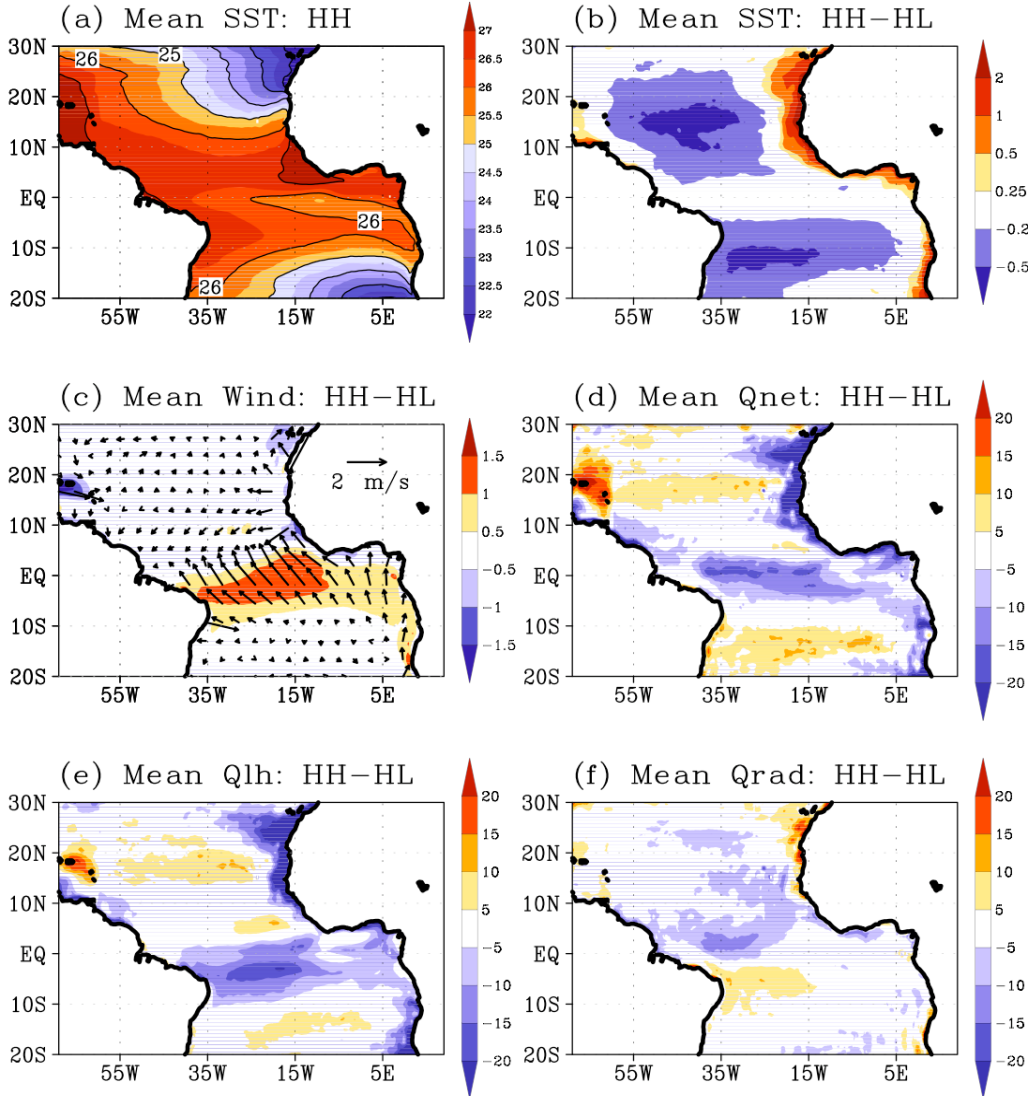


Figure 5.11 (a) Six-year mean SST in HH. (b-f) the mean difference with HL (HH minus HL) of (b) SST, (c) 10-m wind speed (shaded) and vectors, (d) net surface heat flux, (e) surface latent heat flux, and (f) net surface radiative flux. The negative (positive) in heat flux in cools (warms) the ocean.

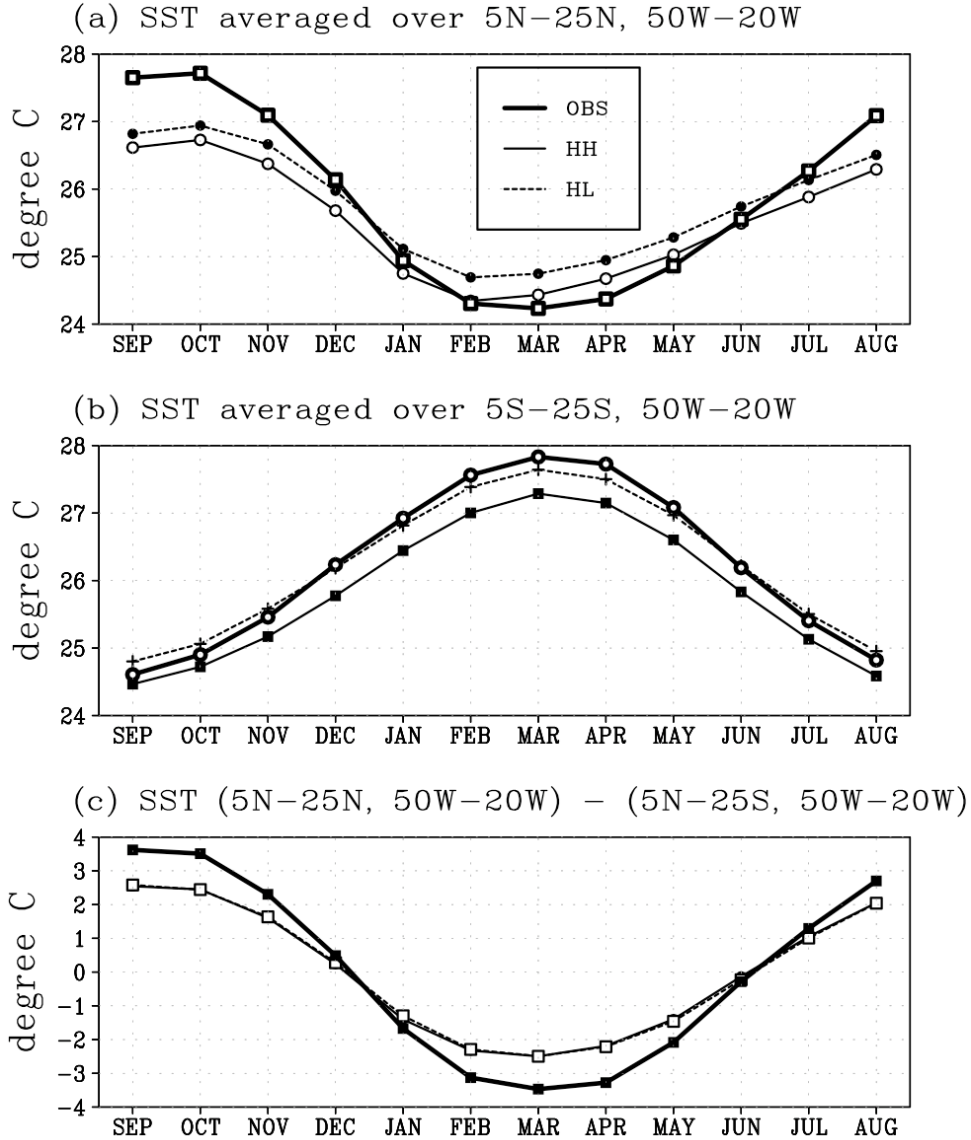


Figure 5.12 (a) Seasonal cycle of monthly averaged SST (1999-2004) over 5°N - 25°N , 50°W - 20°W for (thick solid) the observations from TRMM SST, (thin solid) HH, and (thin dashed) HL. (b) Same as (a), except for the southern hemisphere in 5°S - 25°S , 50°W - 20°W . (c) Same as (a) except for the seasonal cycle of meridional gradient of SST anomaly. SST gradient is computed as the difference in SST anomaly in the northern extratropics (5°N - 25°N , 50°W - 20°W) and the southern extratropics (5°S - 25°S , 50°W - 20°W).

Chapter 6

Summary and Future Plans

6.1 Summary of Results

This chapter provides a summary of the results of dissertation research. The summary is followed by a brief background introduction and description of some of my planned future research.

Overall, this dissertation research consisted of three major components:

1. Developing and testing the Scripps Coupled Ocean-Atmosphere Regional (SCOAR) Model (Chapter 2),
2. Studying mesoscale ocean-atmosphere interactions (Chapter 2 and 3), and
3. Investigating the connection between mesoscale ocean-atmosphere features and larger-scale climate variability (Chapter 4 and 5).

In Chapter 2, a detailed description of the SCOAR model was presented. The uniqueness of the SCOAR model is that it has great portability, flexible coupling processes, parallel architecture, state-of-the-art physics, and realistic large-scale forcing consistent with the National Centers for Environmental Prediction (NCEP) Reanalysis products.

A quantitative assessment of the SCOAR model performance is provided for three different scenarios in the eastern Pacific sector: tropical instability waves (TIWs) in the equatorial ocean, mesoscale eddies and upwelling fronts in the California Current System

(CCS) region and mountain gap winds and their effects on the regional climate of the Central American coast (CAC). For all three cases, the SCOAR model is capable of capturing the salient features of the observed coupled feedback involving mesoscale oceanic and short-scale atmospheric variability.

The characteristics of the TIWs generated in the SCOAR model agree well with the observations (Legeckis 1977). It was shown that the model quantitatively reproduces the observed linear relation of the perturbation wind stress and turbulent heat flux with the propagating SST anomalies of TIWs. Large perturbations in the surface fluxes imply a potential feedback on the ocean (Chelton et al. 2001). The influence of these TIW-induced SST anomalies is not confined to the near-surface, but extends throughout the whole height of the atmospheric boundary layer (Hashizume et al. 2002).

The universal nature of the interaction of the mesoscale SST and the atmospheric boundary layer (Xie 2004) is also observed in the midlatitude coastal ocean in the CCS. Observations and modeling studies reveal that summertime SST fronts due to coastal upwelling and mesoscale eddies exert a significant impact on the atmosphere, which is most evident in the wind stress derivative fields (Chelton et al. 2007, Haack et al. 2005). This indicates significant feedback effects on the ocean, which can alter the SST and the dynamical properties of the CCS. The model reproduces an observed aspect of coupling of the mesoscale SST fronts and the wind stress curl, although the intensity of coupling strength is underestimated.

Lastly, in the CAC region, the model reproduces observed patterns of air-sea interaction arising from the orographically induced gap winds and the thermocline dome. These gap winds exert significant forcings on the eastern Pacific warm pool via direct wind-induced mixing and the turbulent heat flux, and through Ekman upwelling and

downwelling. The pronounced positive Ekman forcing input by the Papagayo jet generates what is referred to as the Costa Rica Dome, the permanent shoaling of the thermocline centered at 9°N, 90°W. The slow evolution of the ocean thermocline exerts its strongest impact on the SST, which consequently affects seasonal precipitation during the summer months when the mean Inter-Tropical Convergence Zone (ITCZ) is located directly overhead. The colder SST, which is below the convective thresholds, is associated with the shallow thermocline, suppresses the atmospheric deep convection, and punches a “dry hole” in the summertime mean ITCZ. This seasonal coupled process was first hypothesized by Xie et al. (2005) based on satellite observations, and is supported by the present modeling study. This suggests that the narrow mountain gaps in the coastal range and the low-level gap winds are central components of the eastern Pacific climate, which help establish the distinctively different climate regime that occurs in the eastern Pacific compared to the western and central Pacific (Kessler 2002).

In Chapter 3, the study of the air-sea interaction involving the TIWs was extended to investigate potential effects of the atmospheric feedback on the tropical Atlantic Ocean. Analysis reveals that the perturbation winds generated by the evolving TIW-induced SST anomalies are negatively correlated with the TIW-induced surface currents. This indicates that the TIW currents are slowed down by the overlying wind response. This effect is sink of eddy kinetic energy (EKE) of the TIWs, estimated to be roughly 10% of the oceanic barotropic instability, which is the dominant source for the EKE of the TIW. Furthermore, it is shown that TIW-induced perturbation ocean currents can significantly alter the surface wind stress estimate from satellite scatterometers. Surface stress over the TIWs can vary by ±25-30% due to the surface currents of the TIWs. This implies a consistency problem for ocean simulations forced with the observed QuikSCAT

wind stresses, where a mismatch between the prescribed winds and the generated waves can lead to a potentially spurious feedback on the waves.

Chapter 4 presented the results from the study of the effect of oceanic mesoscale features on the mean climate of the tropical Atlantic. It was shown that resolving oceanic mesoscale variability, such as that due to the TIWs and the details of the coastal upwelling, can help mitigate the warm biases, which are commonly exhibited by most of the coarse-resolution coupled climate models (Davey et al. 2002). The resultant meridional SST gradient favors the improved mean precipitation simulations in the ITCZ. This model result represents a clear improvement of the mean climate simulations in the tropical Atlantic, and emphasizes the importance of the poorly resolved mesoscale oceanic features and the coupled feedback for their net contribution to the basin-scale climate (Jochum and Murtugudde 2006).

Chapter 5 focused on simulating the mean ITCZ in a coupled climate model and sheds light on the importance of synoptic-scale atmospheric disturbances. The African easterly waves (AEWs) modulate the convection and the daily precipitation over western Africa and contribute to cyclogenesis over the Atlantic and the eastern Pacific Ocean (Thorncroft et al. 2003 and the references therein). The comparison of the SCOAR model results using coarse and fine atmospheric resolution simulations reveals that strong shear of the easterly waves is accompanied by extreme precipitation only on the finer atmospheric grid. This is because the computed near-surface convergence is substantially higher in the high resolution, which is, compared to the estimate from the QuikSCAT, more realistic. The strong low-level convergence triggers more intense local convection, which facilitates heavy precipitation events associated with the synoptic-scale tropical storms and at times hurricanes. The variability in rainfall on these time scales accounts

for 60-80% of its total variability. The climatic importance of better-resolved convergence and convection processes in the easterly waves is that they can lead to a more realistic model precipitation climatology and seasonality over the Atlantic Ocean. This suggests that capturing these transient atmospheric waves and the resultant low-level convergence is important for improving the simulation of precipitation in global coupled climate models, with obvious implications for regional climate prediction.

6.2 Future Plans

This research has clearly demonstrated that the SCOAR model is a unique and useful tool for studying mesoscale air-sea coupling processes in different climate regimes. With many challenging but interesting scientific goals, I intend to continue to study various coupled climate processes, not necessarily limited to the tropics but also including the mid and eventually high latitudes. For example, I am preparing several long-term simulations using SCOAR in the Indian Ocean and in the North Pacific Ocean.

In the Indian Ocean (IO), I intend to develop a set of 50-year simulations with and without the large-scale interannual forcing due to El Niño-Southern Oscillation (ENSO) events and Eurasian snow cover. The hypothesis is that a regional feedback between the IO warm pool and the Findlater Jet determines the variability of the ITCZ and the monsoons. The goal of this study is to understand the importance of the local coupled feedback effects, compared to remote influences from the large-scale ENSO forcing, in determining the basin-scale climate. The local processes are not realistically simulated in current state-of-the-art coupled climate models, which exhibit spurious coupled feedbacks between the warm pool in the IO, the Findlater Jet, and the Indian summer monsoons, which are related in turn to coupled interactions in the Southern Indian Ocean,

Arabian Sea, and the Bay of Bengal. We believe that these coupled processes are mostly due to the poor resolution in the ocean and atmosphere and subsequent lack of coupling. The ultimate goal is to explore the potential predictability problem of the seasonal and interannual monsoon variability and its relation to intraseasonal variability such as the Madden-Julian Oscillations, which has significant climatic implications to the global climate.

In addition, I would like to investigate air-sea interaction associated with tropical cyclones in the IO. How do they make a large-scale contribution to the oceanic heat content? How does this feed back on the hurricane activity? Of significant importance to the neighboring continents in the IO would be how to predict the evolution and pathways of the landfall cyclones.

We also plan to investigate how SST variability in the Kuroshio-Oyashio-Extention (KOE) can excite a basin-wide atmospheric response in the North Pacific and downstream regions over the North America. This interannual and decadal process inherently involves mesoscale oceanic variability and local air-sea interaction, which can create anomalous SSTs in the KOE region, as well as large-scale oceanic and atmospheric wave adjustment processes, which can deliver coupled signals into the downstream region (Miller et al. 1994; Schneider et al. 2002). In addition, the prediction of the KOE SST itself is imperative for storm track variability in the North Pacific, as the atmosphere is particularly sensitive to the changes in KOE SST.

For this purpose, we are planning a set of coupled and uncoupled 50-year hindcast simulations downscaled from the NCEP large-scale atmospheric forcings. The model results in tandem with a comparison to the available observations will allow investigations to isolate which part of the atmospheric response is due to ocean-

atmosphere coupling, and which part is the response to specified oceanic and atmospheric forcing. This study will be linked to the predictability of climate variability on interannual timescales in the North Pacific and its downstream regions, which are important for ecosystem and commercial fisheries in the California Current System, the Bering Sea, and the Gulf of Alaska.

References

- Albignat, J. P. and R. J. Reed, 1980: The origin of African wave disturbances during Phase III of GATE. *Mon. Wea. Rev.*, **108**, 1827-1839.
- Aldrian, E., D. V. Sein, D. Jacob, L. D. Gates, and R. Podzun, 2005: Modeling Indonesian rainfall with a coupled regional model. *Clim. Dynm.*, **25**, 1-17
- Allen, J. S., 1980: Models of wind-driven currents on the continental shelf. *Annu. Rev. Fluid Mech.*, **12**, 389-433
- Arakawa, A., and W. H. Schubert, 1974: Interaction of a Cumulus Cloud Ensemble with the Large-Scale Environment, Part I. *J. Atmos. Sci.*, **31**, 674-701
- Avila, L. A. and R. J. Pasch, 1992: Atlantic tropical systems of 1991. *Mon. Wea. Rev.*, **120**, 2688-2696
- Bao, J.-W., J. M. Wilczak, J.-K. Choi, and L. H. Kantha, 2000: Numerical Simulations of Air-Sea Interactions under High Wind Conditions Using a Coupled Model: A Study of Hurricane Development. *Mon. Wea. Rev.*, **128**, 2190-2210
- Baturin, N. G., and P. P. Niiler, 1997: Effects of instability waves in the mixed layer of the equatorial Pacific. *J. Geophys. Res.*, **102**, 27771-27794
- Behringer, D., L. Regier, and H. Stommel, 1979: Thermal feedback on wind-stress as a contributing cause of the Gulf Stream. *J. Mar. Res.*, **37**, 699-709
- Bender, M. A. and I. Ginis, 2000: Real-case simulations of hurricane-ocean interaction using a high-resolution coupled model: Effects on hurricane intensity. *Mon. Wea. Rev.*, **128**, 917-946
- Berry, G. J. and C. D. Thorncroft, 2005: Case Study of an Intense African Easterly Wave. *Mon. Wea. Rev.*, **133**, 752-766
- Biasutti, M., A. H. Sobel, and Y. Kushnir, 2006: AGCM Precipitation Biases in the Tropical Atlantic. *J. Climate*, **19**, 935-958
- Brandt, P., F. A. Schott, C. Provost, A. Kartavtesff, V. Hormann, B. Bourlès, J. Fischer, 2006: Circulations in the central equatorial Atlantic: Mean and Intraseasonal to seasonal variability. *Geophys. Res. Lett.*, **33**, L07609
- Bryden, H. L., and E. C. Brady, 1989: Eddy momentum and heat fluxes and their effect on the circulation of the equatorial Pacific Ocean. *J. Mar. Res.*, **47**, 55-79
- Burpee, R. W., 1972: The origin and structure of easterly waves in the lower troposphere of North Africa. *J. Atmos. Sci.*, **29**, 77-90

- Bye, J. A. T., 1986: Momentum exchange at the sea surface by wind stress and understress. *Quart. J. R. Met. Soc.*, **112**, 501-510
- Carlson, T. N., 1969: Some remarks on African disturbances and their progress over the tropical Atlantic. *Mon. Wea. Rev.*, **97**, 716-726
- Castelao, R. M., T. P. Mavor, J. A. Barth, and L. C. Breaker, 2006: Sea-surface temperature fronts in the California Current System from geostationary satellite observations. *J. Geophys. Res.-Ocean*, submitted
- Chang, P., L. Ji, and H. Li, 1997: A decadal climate variation in the tropical Atlantic ocean from thermodynamic air-sea interactions. *Nature*, **385**, 516-518
- Charney, J. G., and M. E. Stern, 1962: On the stability of internal baroclinic jets in a rotating atmosphere. *J. Atmos. Sci.*, **19**, 159–172
- Chelton, D. B., M. G. Schlax, and R. M. Samelson, 2007: Summertime Influence of Sea Surface Temperature on the Wind Stress Field Over the California Current. *J. Phys. Oceanogr.*, in press
- Chelton, D. B., and F. J. Wentz, 2005: Global microwave satellite observations of sea-surface temperature for numerical weather prediction and climate research. *Bull. Amer. Meteor. Soc.*, **86**, 1097-1115
- Chelton, D. B., 2005: The Impact of SST Specification on ECMWF Surface Wind Stress Fields in the Eastern Tropical Pacific. *J. Climate*, **18**, 530–550
- Chelton, D. B., and M. H. Freilich, 2005: Scatterometer-based assessment of 10-m wind analyses from the operational ECMWF and NCEP numerical weather prediction models. *Mon. Wea. Rev.*, **133**, 409-429
- Chelton, D. B., M. G. Schlax, M. H. Freilich, and R. F. Milliff, 2004: Satellite measurements reveal persistent small-scale features in ocean winds. *Science*, **303**, 978–983
- Chelton, D. B., and S. K. Esbensen, M. G. Schlax, N. Thum, M. H. Freilich, F. J. Wentz, C. L. Gentemann, M. J. McPhaden, and P. S. Schopf, 2001: Observations of coupling between surface wind stress and sea surface temperature in the eastern tropical Pacific. *J. Climate*, **14**, 1479-1498
- Chelton, D. B., M. H. Freilich, and S. N. Esbensen, 2000a: Satellite observations of the wind jets off the Pacific coast of Central America. Part I: Case studies and statistical characteristics. *Mon. Wea. Rev.*, **128**, 1993–2018

- Chelton, D. B., M. H. Freilich, and S. N. Esbensen, 2000b: Satellite observations of the wind jets off the Pacific coast of Central America. Part II: Regional Relationships and Dynamic Considerations. *Mon. Wea. Rev.*, **128**, 2019-2043
- Chelton, D. B., F. J. Wentz, C. L. Gentemann, R. A. de Szoeke, and M. G. Schlax, 2000c: Satellite Microwave SST Observations of Transequatorial Tropical Instability Waves. *Geophys. Res. Lett.*, **9**, 1239-1242
- Chen, S. S., W. Zhao, M. A. Donelan, J. F. Price, E. J. Walsh, T. B. Sanford, and H. L. Tolman, 2006: Fully coupled atmosphere-wave-ocean modeling for hurricane research and prediction: Results from CBLAST-Hurricane. *Bull. Amer. Meteor. Soc.*, *submitted*
- Chiang, J. C. H., Kushnir, Y., and Giannini, A., 2002: Deconstructing Atlantic Intertropical Convergence Zone variability: Influence of the local cross-equatorial sea surface temperature gradient and remote forcing from the eastern equatorial Pacific. *J. Geophys. Res.*, **107(D1)**, 10.1029/2000JD000307
- Conkright, M. E., R. A. Locarnini, H. E. Garcia, T. D. O'Brien, T. P. Boyer, C. Stephens, J. J. Antonov, 2002: World Ocean Atlas 2001: Objective Analysis, Data Statistics, and Figure, CD-ROM Documentation. *National Oceanographic Data Center, Silver Spring, MD*, 17p
- Cook, K. H: 1999: Generation of the African Easterly Jet and Its Role in Determining West African Precipitation. *J. Climate*, **12**, 1165-1184
- Cornillon, P. and K.-A. Park, 2001: Warm core ring velocities inferred from NSCAT. *Geophys. Res. Lett.*, **28**, 575-578
- Cox, M. D., 1980: Generation and propagation of 30-day waves in a numerical model of the Pacific. *J. Phys. Oceanogr.*, **10**, 1168-1186
- Cronin, M. F., N. A. Bond, C. Fairall, J. Hare, M. J. McPhaden, and R. A. Weller, 2002: Enhanced oceanic and atmospheric monitoring underway in eastern Pacific. *Eos, Trans. Amer. Geophys. Union*, **83**, 210-211
- Dai, A. G., and T. M. L. Wigley 2000: Global patterns of ENSO-induced precipitation. *Geophys. Res. Lett.*, **27**, 1283-1286
- da Silva, A., Young, C., Levitus, S., 1994: Atlas of Surface Marine Data 1994. NOAA Atlas NESDIS 6-110, US Government Printing Office, Washington, DC, pp. 1-5
- Davey, M., and M. Huddleston, K. Sperber, P. Braconnot, F. Bryan, D. Chen, R. Colman, C. Cooper, U. Cubasch, P. Delecluse, D. DeWitt, L. Fairhead, G. Flato, C. Gordon, T. Hogan, M. Ji, M. Kimoto, A. Kitoh, T. Knutson, M. Latif, H. Le Treut, T. Li, S. Manabe, C. Mechoso, G. Meehl, S. Power, E. Roeckner, L. Terray, A. Vintzileos, R. Voss, B. Wang, W. Washington, I. Yoshikawa, J. Yu, S.

- Yukimoto and S. Zebiak, 2002: STOIC: A study of coupled model climatology and variability in tropical ocean regions. *Clim. Dynm.*, **18**, 403-420
- Dawe, J. T. and L. Thompson, 2006: The effect of ocean surface currents on wind stress, heat flux, and wind power input to the ocean. *Geophys. Res. Lett.*, **33**, No. 9, L09604 10.1029/2006GL025784
- Deser, C., J. J. Bates, and S. Wahl, 1993: The influence of sea surface temperature gradients on stratiform cloudiness along the equatorial front in the Pacific Ocean. *J. Climate*, **6**, 1172–1180
- de Szoeke, S. P., C. S. Bretherton, N. A. Bond, M. F. Cronin, and B. M. Morley, 2005: EPIC 95°W Observations of the Eastern Pacific Atmospheric Boundary Layer from the Cold Tongue to the ITCZ. *J. Atmos. Sci.*, **62**, 426-442
- de Szoeke, S. P., and C. S. Bretherton, 2004: Quasi-Lagrangian Large Eddy Simulations of Cross-Equatorial Flow in the East Pacific Atmospheric Boundary Layer. *J. Atmos. Sci.*, **61**, 1837-1858
- Di Lorenzo, E., 2003: Seasonal dynamics of the surface circulation in the Southern California Current System. *Deep-Sea. Res. II*, **50**, 2371-2388
- Di Lorenzo, E., A. J. Miller, N. Schneider, and J. C. McWilliams, 2005: The warming of the California Current System: Dynamics and ecosystem implications. *J. Phys. Oceanogr.*, **35** (3), 336-362
- Döscher, R., U. Willén, C. Jones, A. Rutgersson, H.E.M. Meier, U. Hansson, and L. P. Graham, 2002: The development of the regional coupled ocean-atmosphere model RCAO. *Boreal Env. Res.*, **7**, 183-192
- Duhaut, T. H. A., and D. N. Straub, 2006: Wind stress dependence on ocean surface velocity: implications for mechanical energy input to ocean circulation. *J. Phys. Oceanogr.*, **36**, 202–211
- Düing, W., P. Hisard, E. Katz, J. Knauss, J. Meincke, L. Miller, K. Moroshkin, G. Philander, A. Rybnikov, K. Voigt, R. Weisberg, 1975: Meanders and long waves in the equatorial Atlantic. *Nature*, **257**, 280-284
- Eady, E. T., 1949: Long Waves and Cyclone Waves, *Tellus*, **1**, 33-52
- Emanuel, K., 2005: Increasing destructiveness of tropical cyclones over the past 30 years. *Nature*, **436**, 686-688
- Enfield, D B., and D. A. Mayer, 1997: Tropical Atlantic sea surface temperature variability and its relation to El Nino-Southern Oscillation. *J. Geophys. Res.*, **102**, 929-945

- Fairall, C. W., E. F. Bradley, D. P. Rogers, J. B. Edson, and G. S. Young, 1996: Bulk parameterization of air-sea fluxes for Tropical Ocean Global Atmosphere Coupled-Ocean Atmosphere Response Experiment. *J. Geophys. Res.*, **101**, 3747-3764
- Fiedler, P. C., 2002: The annual cycle and biological effects of the Costal Rica Dome. *Deep-Sea Res.*, **49A**, 321-338
- Fiedler, P. C., 1994: Seasonal and interannual variability of coastal zone color scanner phytoplankton pigments and winds in the eastern tropical Pacific. *J. Geophys. Res.*, **99**, 18371-18384
- Folland, C., T. Palmer, and D. Parker, 1986: Sahel rainfall and worldwide sea temperatures: 1901-85. *Nature*, **320**, 602-606
- Frank, N. L., 1970: Atlantic tropical systems of 1969. *Mon. Wea. Rev.*, **98**, 307-314
- Gill, A. E., 1980: Some simple solutions for heat-induced tropical circulations. *Quart. J. Roy. Meteor. Soc.*, **106**, 447-462
- Gu, G., R. F. Adler, G. J. Huffman, and S. Curtis, 2004: African easterly waves and their association with precipitation. *J. Geophys. Res.*, **109**, D04101
- Gustafsson, N., L. Nyberg, and A. Omstedt, 1998: Coupling of a High-Resolution Atmospheric Model and an Ocean Model for the Baltic Sea. *Mon. Wea. Rev.*, **126**, 2822-2846
- Haack, T., S. D. Burk, and R. M. Hodur, 2005: U.S. West Coast Surface Heat Fluxes, Wind Stress, and Wind Stress Curl from a Mesoscale Model. *Mon. Wea. Rev.*, **133**, 3202-3216
- Hagedorn, R., A. Lehmann, and D. Jacob, 2000: A coupled high resolution atmosphere-ocean model for the BALTEX region. *Meteorol. Z.*, **9**, 7-20
- Haidvogel, D. B., H. G. Arango, K. Hedstrom, A. Beckmann, P. Malanotte-Rizzoli, and A. F. Shchepetkin, 2000: Model Evaluation Experiments in the North Atlantic Basin: Simulations in Nonlinear Terrain-Following Coordinates, *Dyn. Atmos. Oceans*, **32**, 239-281
- Hansen, D. and C. A. Paul, 1984: Genesis and effects of long waves in the equatorial Pacific. *J. Geophys. Res.*, **89**, 10431-10440
- Hashizume, H., S.-P. Xie, M. Fujiwara, M. Shiotani, T. Watanabe, Y. Tanimoto, W. T. Liu, and K. Takeuchi, 2002: Direct observations of atmospheric boundary layer response to SST variations associated with Tropical Instability Waves over the eastern equatorial Pacific. *J. Climate*, **15**, 3379–3393

- Hashizume, H., S.-P., Xie, W. T. Liu, and K. Takeuchi, 2001: Local and remote atmospheric response to tropical instability waves: A global view from space. *J. Geophys. Res.*, **106**, 10173-10185
- Hastenrath, S., and L. Greischar, 1993: Circulation Mechanisms Related to Northeast Brazil Rainfall Anomalies. *J. Geophys. Res.*, **98**, 5093-5102
- Hastenrath, S., and L. Heller, 1977: Dynamics of Climate Hazards in Northeast Brazil. *Q. J. R. Meteorol. Soc.*, **103**, 77-92
- Hayes, S. P., M. J. McPhaden, and J. M. Wallace, 1989: The Influence of Sea Surface Temperature on Surface Wind in the Eastern Equatorial Pacific: Weekly to Monthly Variability. *J. Climate*, **2**, 1500-1506
- Hickey, B. M., 1979: The California Current System-Hypothesis and facts. *Progress in Oceanography*, **8**, 191-279
- Hong, S.-Y., and H.-L. Pan, 1996: Nonlocal Boundary Layer Vertical Diffusion in a Medium-Range Forecast Model. *Mon. Wea. Rev.*, **124**, 2322-2339
- Hsieh, J.-S. and K. H. Cook, 2005: Generation of African Easterly Wave Disturbances: Relationship to the African Easterly Jet. *Mon. Wea. Rev.*, **133**, 1311-1327
- Huang, B., P. S. Schopf, and J. Shukla, 2004: Intrinsic Ocean-Atmosphere Variability of the Tropical Atlantic Ocean. *J. Climate*, **17**, 2058-2077
- Hurd, W. E., 1929a: Fog in the Gulf of Tehuantepec, November 1929. *Mon. Wea. Rev.*, **57**, 485-485
- Hurd, W. E., 1929b: Northers of the Gulf of Tehuantepec. *Mon. Wea. Rev.*, **57**, 192-194
- Jochum, M. and R. Murtugudde, 2006: Temperature Advection by Tropical Instability Waves. *J. Phys. Oceanogr.*, **36**, 592-605
- Jochum, M., and R. Murtugudde, 2005: Internal Variability of Indian Ocean SST. *J. Climate*, **18**, 3726-3738
- Jochum, M., Murtugudde, R., Manlanotte-Rizzoli, P., and Busalachi, A., 2004: Internal Variability of the Tropical Atlantic Ocean, *Geophys. Monogr. Ser.*, **147**, 181-187
- Jochum, M., P. Malanotte-Rizzoli, and A. Busalacchi, 2004: Tropical Instability Waves in the Atlantic Ocean. *Ocean. Modell.*, **7**, 145-163
- Johns, W. E., T. N. Lee, R. C. Beardsley, J. Candela, R. Limeburner, B. Castro, 1998: Annual cycle and variability of the North Brazil Current. *J. Phys. Oceanogr.*, **28**(1), 103-128

- Juang, H.-M. H. and M. Kanamitsu, 1994: The NMC nested regional spectral model. *Mon. Wea. Rev.*, **122**, 3-26
- Juang, H.-M. H., S.-Y. Hong, and M. Kanamitsu, 1997: The NCEP Regional Spectral Model: An Update. *Bull. Am. Meteorol. Soc.*, **78**, No 10
- Kalnay, E., and Co-authors, 1996: The NCEP/NCAR 40-Year Reanalysis Project. *Bull. Amer. Met. Soc.*, **77**, 437-471
- Kanamaru, H. and M. Kanamitsu, 2007: Scale Selective Bias Correction in a Downscaling of Global Analysis using a Regional Model. *Mon. Wea. Rev.*, **135**, 334-350
- Kanamitsu, M., W. Ebisuzaki, J. Woolen, J. Potter, and M. Fiorino, 2002a: NCEP-DOE AMIP-II Reanalysis (R-2). *Bull. Amer. Met. Soc.* **83**, 1631-1643
- Kanamitsu, M., H. Kanamaru, Y. Cui, and H. Juang, 2005: Parallel Implementation of the Regional Spectral Atmospheric Model. CEC-500-2005-014.
- Kanamitsu, M., A. Kumar, H.-M. H. Juang, J.-K. Schemm, W. Wang, F. Yang, S.-Y. Hong, P. Peng, W. Chen, S. Moorthi, and M. Ji, 2002b: NCEP Dynamical Seasonal Forecast System 2000. *Bull. Amer. Met. Soc.*, **83**, 1019-1037
- Kelly, K. A., S. Dickinson, M. J. McPhaden, and G. C. Johnson, 2001: Ocean Currents Evident in Satellite Wind Data. *Geophys. Res. Lett.*, **28**, 2469-2472
- Kessler, W. S., G. C. Johnson, and D. W. Moore, 2003: Sverdrup and nonlinear dynamics of the Pacific Equatorial Currents. *J. Phys. Oceanogr.*, **33**, 994-1008
- Kessler, W. S., 2002: Mean Three-Dimensional Circulation in the Northeast Tropical Pacific. *J. Phys. Oceanogr.*, **32**, 2457-2471
- Landsea, C. W., G. D. Bell, W. M. Gray, and S. B. Goldenberg, 1998: The extremely active 1995 Atlantic hurricane season: Environmental conditions and verification of seasonal forecast. *Mon. Wea. Rev.*, **126**, 1174-1193
- Laprise, R., 1992: The resolution of global spectral models. *Bull. Amer. Met. Soc.*, **73**, 1453-1454
- Large, W. G., J. C. McWilliams, S. C. Doney, 1994: Oceanic vertical mixing: a review and a model with a nonlocal boundary layer parameterization. *Rev. Geophys.*, **32** (4), 363-404
- Legeckis, R., 1977: Long waves in the Eastern Equatorial Pacific Ocean: A View from a Geostationary Satellite. *Science*, **197**, 1177-1181

- Legeckis, R., W. Pichel, and G. Nesterczuk, 1983: Equatorial Long Waves in Geostationary Satellite Observations and in a Multichannel Sea Surface Temperature Analysis. *Bull. Am. Meteorol. Soc.*, **64**, 133-139
- Legeckis, R., and Reverdin, G., 1987: Long waves in the equatorial Atlantic Ocean during 1983. *J. Geophys. Res.*, **92**, 2835-2842
- Levitus, S., and T. P. Boyer, 1994a: Temperature, Vol. 4, World Ocean Atlas 1994. NOAA Atlas NESDIS 4, 117pp
- Levitus, S., and Burgette, and T. P. Boyer, 1994b: Salinity. Vol. 3, World Ocean Atlas 1994. NOAA Atlas NESDIS 3, 99pp
- Li, Y., and H. Xue, 2002: Air-sea interactions during the passage of a winter storm over the Gulf Stream: A three-dimensional coupled atmosphere-ocean model study. *J. Geophys. Res.*, **107**, NO. C11, 3200, doi:10.1029/2001JC001161
- Lindzen, R. S., and Nigam S, 1987: On the role of sea surface temperature gradients in forcing low-level winds and convergence in the tropics, *J. Atmos. Sci.*, **44**, 2418–2436
- Liu, W. T, X. Xie, P. S. Polito, S. P. Xie, and H. Hashizume, 2000: Atmospheric manifestation of tropical instability waves observed by QuikSCAT and Tropical Rain Measuring Mission. *Geophys. Res. Lett.*, **27**, 2545–2548
- Loglisci, N., M. W. Qian, N. Rachev, C. Cassardo, A. Longhetto, R. Purini, P. Trivero, S. Ferrarese, and C. Giraud, 2004: Development of an atmosphere-ocean coupled model and its application over the Adriatic Sea during a severe weather event of Bora wind. *J. Geophys. Res.*, **109**, D01102, doi:10.1029/2003JD003956
- Lonfat, M., F. D. Marks, Jr., S. S. Chen, 2004: Precipitation Distribution in Tropical Cyclones Using the Tropical Rainfall Measuring Mission (TRMM) Microwave Imager: A Global Perspective. *Mon. Wea. Rev.*, **132**, 1645-1660
- Luo, J.-J., S. Masson, E. Roeckner, G. Madec, and T. Yamagata, 2005 : Reducing Climatology Bias in an Ocean-Atmosphere CGCM with Improved Coupling Physics. *J. Climate*, **18** (13), 2344-2360
- Lynn, R. J., and J. J. Simpson, 1987: The California Current system: The seasonal variability of its physical characteristics. *J. Geophys. Res.*, **92**, 12947-12966
- Marchesiello, P., J. C. McWilliams, and A. Shchepetkin, 2001: Open boundary conditions for long-term integration of regional oceanic models. *Ocean Modell.*, **3**, 1-20

- Marchesiello, P., J. C. McWilliams, and A. Shchepetkin, 2003: Equilibrium structure and dynamics of the California Current System. *J. Phys. Oceanogr.*, **33**(4), 753-783
- Masina, S., S. Philander, A. Bush, 1999: An analysis of tropical instability waves in a numerical model of the Pacific Ocean-2. Generation and energetics of the waves. *J. Geophys. Res.*, **104**, 29613-29635
- McCreary, J. P., Jr., H. S. Lee, and D. B. Enfield, 1989: The response of the coastal ocean to strong offshore winds: With application to circulations in the Gulfs of Tehuantepec and Papagayo. *J. Mar. Res.*, **47**, 81-109
- Mechoso, C. R. A.W. Robertson, N. Barth, M.K. Davey, P. Delecluse, P.R. Gent, S. Ineson, B. Kirtman, M. Latif, H. Le Treut, T. Nagai, J.D. Neelin, S.G.H. Philander, J. Polcher, P.S. Schopf, T. Stockdale, M.J. Suarez, L. Terray, O. Thual, and J.J. Tribbia, 1995: The seasonal Cycle over the Tropical Pacific in Coupled Ocean-Atmosphere General Circulations Models. *Mon. Wea. Rev.*, **123**, 2825-2838
- Mekonnen, A., C. D. Thorncroft, and A. R. Aiyyer, 2006: Analysis of Convection and Its Association with African Easterly Waves. *J. Climate*, **19**, 5405-5421
- Mikolajewicz, U., D. V. Sein, D. Jacob, T. Konigk, R. Pozdun, and T. Semmler, 2005: Simulating Arctic sea ice variability with a coupled regional atmosphere-ocean-sea ice model. *Meteorol. Z.*, **14**, 793-800
- Miller, A. J., D. R. Cayan, T. P. Barnett, N. E. Graham, and J. M. Oberhuber, 1994: Interdecadal variability of the Pacific Ocean: Model response to observed heat flux and wind stress anomalies. *Climate Dyn.*, **9**, 287-302
- Moore, A. M., H. G. Arango, E. Di Lorenzo, D. B. Cornuelle, A. J. Miller, and D. J. Nielson, 2004: A comprehensive ocean prediction and analysis system based on the tangent linear and adjoint of a regional ocean model. *Ocean Modell.*, **7**, 227-258
- Moorthi, S., and M. J. Suarez, 1992: Relaxed Arakawa-Schubert. A Parameterization of Moist Convection for General Circulation Models. *Mon. Wea. Rev.*, **120**, 978-1002
- Nobre, P., and J. Shukla, 1996: Variations of sea surface temperature, wind stress and rainfall over the tropical Atlantic and South America, *J. Climate*, **9**, 2464-2479
- Nonaka, M., and S.-P. Xie, 2003: Covariations of sea surface temperature and wind over the Kurishio and its extension: Evidence for ocean-to-atmosphere feedback. *J. Climate*, **16**, 1404-1413

- O'Neill, L. W., D. B. Chelton, and S. K. Esbensen, and F. J. Wentz, 2005: High-Resolution Satellite Measurements of the Atmospheric Boundary Layer Response to SST Variations along Agulhas Return Current. *J. Climate*, **18**, 2706-2723
- Overland, J. E., and B. A. Walter Jr., 1981: Gap winds in the Strait of Juan de Fuca. *Mon. Wea. Rev.*, **109**, 2221-2233
- Pacanowski, R. C., 1987: Effect of Equatorial Currents on Surface Stress. *J. Phys. Oceanogr.*, **17**, 833-838
- Palacios, D. M., and S. J. Bograd, 2005: A census of Tehuantepec and Papagayo eddies in the northeastern tropical Pacific, *Geophys. Res. Lett.*, **32**, L23606
- Palmer, T., 1986: Influence of Atlantic, Pacific, and Indian oceans on Sahel rainfall. *Nature*, **322**, 251-253
- Park, K.-A., P. Cornillon, and D. L. Codiga, 2006: Modification of surface winds near ocean fronts: Effects of Gulf Stream rings on scatterometer (QuikSCAT, NSCAT) wind observations. *J. Geophys. Res.*, **111**, C03021, doi:10.1029/2005JC003016
- Parmenter, F. C., 1970: A "Tehuantepecer.". *Mon. Wea. Rev.*, **98**, 497
- Pauluis, O. and S. Garner, 2006: Sensitivity of Radiative-Convective Equilibrium Simulations to Horizontal Resolution. *J. Atmos. Sci.*, **63**, 1910-1923
- Payne, S. and M. M. McGarry, 1977: The relationships of satellite inferred convective activity to easterly waves over West Africa and the adjacent ocean during phase III of GATE. *Mon. Wea. Rev.*, **105**, 413-420
- Peng, M. S., B. Fu, T. F. Hogan, and T. Li, 2006: On African easterly waves that impacted two tropical cyclones in 2004. *Geophys. Res. Lett.*, **33**, L11807
- Perlin, N., R. M. Samelson, and D. B. Chelton, 2004: Scattermoter and model wind and wind stress in the Oregon-Northern California coastal zone. *Mon. Wea. Rev.*, **132**, 2110-2129
- Perrie, W., X. Ren, W. Zhang, and Z. Long, 2004: Simulation of extratropical Hurricane Gustav using a coupled atmosphere-ocean-sea spray model. *Geo. Res. Lett.*, **31**, L03110, doi: 10.1029/2003GL018571
- Pezzi, L. P., J. Vialard, K. J. Richard, C. Menkes, and D. Anderson, 2004: Influence of ocean-atmosphere coupling on the properties of tropical instability waves. *Geophys. Res. Lett.*, **31**, L16306
- Philander, S. G. H., 1976: Instabilities of zonal equatorial currents. *J. Geophys. Res.*, **81**, 3725-3735

- Philander, S. G. H., 1978: Instabilities of zonal equatorial currents, 2. *J. Geophys. Res.*, **83**, 3679-3682
- Pickett, M. H. and J. D. Paduan, 2003: Ekman transport and pumping in the California Current based on the U.S. Navy's high-resolution atmospheric model (COAMPS). *J. Geophys. Res.*, **108**, NO. C10, 3327
- Pielke, R. A., 1991: A Recommended specific definition of "resolution". *Bull. Amer. Meteor. Soc.*, **72**, 1914
- Polito, P. S., J. P. Ryan, W. T. Liu, and F. P. Chavez, 2001: Oceanic And Atmospheric Anomalies of Tropical Instability Waves. *Geophys. Res. Lett.*, **28**, 2233-2236
- Powers, J. G. and M. T. Stoelinga, 2000: A Coupled Air-Sea Mesoscale Model: Experiments in Atmospheric Sensitivity to Marine Roughness. *Mon. Wea. Rev.*, **128**, 208-228
- Proehl, H., 1996: Linear instability of equatorial zonal flows. *J. Phys. Oceanogr.*, **26**, 601-621
- Pullen, J., J. D. Doyle, and R. P. Signell, 2006: Two-Way Air-Sea Coupling: A Study of the Adriatic. *Mon. Wea. Rev.*, **134**, 1465-1483
- Pytharoulis, I., and C. Thorncroft, 1999: The low-level structure of African easterly waves in 1995. *Mon. Wea. Rev.*, **127**, 2266-2280
- Qiao, L., and R. H. Weisberg, 1995: Tropical Instability Wave Kinematics: Observations from the Tropical Instability Wave Experiment (TIWE). *J. Phys. Oceanogr.*, **100**, 8677-8693
- Qiao, L., and R. H. Weisberg, 1998: Tropical Instability Waves Energetics: Observations from the Tropical Instability Wave Experiment. *J. Phys. Oceanogr.*, **28**, 345-360
- Raymond, D. J., S. K. Esbensen, M. Gregg, and C. S. Bretherton, 2004: EPIC 2001 and the coupled ocean-atmosphere system of the tropical east Pacific. *Bull. Amer. Meteor. Soc.*, **85**, 1341-1354
- Redelsperger, J.-L., C. D. Thorncroft, A. Diedhiou, T. Lebel, D. J. Parker, and J. Polcher, 2006: African Monsoon Multidisciplinary Analysis. *Bull. Amer. Meteor. Soc.*, **87** (12), 1739-1746
- Reed, R. J., D. C. Norquist, and E. E. Recker, 1977: The structure and properties of African wave disturbances as observed during Phase III of GATE. *Mon. Wea. Rev.*, **105**, 317-333

- Ren, X., and Y. Qian, 2005: A coupled regional air-sea model, its performances and climate drift in simulation of the east Asian summer monsoon in 1998. *Int. J. Climatol.*, **25**, 697-692
- Rennick, M. A., 1976: The generation of African easterly waves. *J. Atmos. Sci.*, **33**, 1955-1969
- Roads, J. O., S.-C. Chen, and M. Kanamitsu, 2003: U.S. regional climate simulations and seasonal forecasts. *J. Geophys. Res.-Atmos.*, **108**(D16), 8606
- Roden, G. I., 1961: On the wind-driven circulation in the Gulf of Tehuantepec and its effect upon surface temperatures. *Geofis. Int.* **1**, 55-72
- Sakamoto, T. T., A. Sumi, S. Emori, T. Nishimura, H. Hasumi, T. Suzuki, and M. Kimoto, 2004: Far-reaching effects on the Hawaiian Islands in the CCSR/NIES/FRCGC high-resolution climate model. *Geophys. Res. Lett.*, **31**, L17212
- Saravanan, R., and P. Chang, 2000: Interaction between tropical Atlantic variability and El Niño-Southern Oscillation. *J. Climate*, **13**, 2177-2194
- Schade, L. R., Emanuel, J. A., 1999: The ocean's effect on the intensity of tropical cyclones: Results from a simple coupled atmosphere-ocean model. *J. Atmos. Sci.*, **56**, 642-651
- Schneider, N., A. J. Miller, and D. W. Pierce, 2002: Anatomy of North Pacific decadal variability. *J. Climate*, **15**, 586-605
- Schott, F. A., M. Dengler, P. Brandt, K. Affler, J. Fischer, B. Bourlès, Y. Gouriou, R. L. Molinari, M. Rhein, 2003: The zonal currents and transports at 35°W in the tropical Atlantic. *Geophys. Res. Lett.*, **30**, NO. 7, 1349, doi:10.1029 / 2002GL016849
- Schrum, C., U. Hübner, D. Jacob, and R. Podzun, 2003: A coupled atmosphere/ice/ocean model for the North Sea and Baltic Sea. *Clim. Dynam.*, **21**, 131-141
- Schultz, D. M., W. E. Bracken, L. F. Bosart, G. J. Hakim, M. A. Bedrick, M. J. Dickinson, and K. R. Tyle, 1997: The 1993 Superstorm Cold Surge: Frontal Structure, Gap Flow, and Tropical Impact. *Mon. Wea. Rev.*, **125**, 5-39
- Seo, H., A. J. Miller and J. O. Roads, 2007: The Scripps Coupled Ocean-Atmosphere Regional (SCOAR) Model, with applications in the eastern Pacific Sector. *Journal of Climate*, **20**, 381-402
- Seo, H., M. Jochum, R. Murtugudde, and A. J. Miller, 2006: Effect of Ocean Mesoscale Variability on the Mean State of Tropical Atlantic Climate. *Geophys. Res. Lett.* **33**, L09606, doi:10.1029/2005GL025651

- Shchepetkin, A. F., and J. C. McWilliams, 2005: The regional oceanic modeling system (ROMS): a split-explicit, free-surface, topography-following-coordinate ocean model. *Ocean Modell.*, **9**, 347-404
- Small, R. J., S.-P. Xie, Y. Wang, S. K. Esbensen, and D. Vickers, 2005: Numerical Simulation of Boundary Layer Structure and Cross-Equatorial Flow in the Eastern Pacific. *J. Atmos. Sci.*, **62**, 1812-1830
- Small, R. J., S.-P. Xie, and Y. Wang, 2003: Numerical Simulation of Atmospheric Response to Pacific Tropical Instability Waves. *J. Climate*, **16**, 3723–3741
- Spall, M. A. Effect of sea surface temperature / wind stress coupling on baroclinic instability in the ocean. *J. Phys. Oceanogr.*, in press
- Steenburgh, W. J., D. M. Schultz, and B. A. Colle, 1998: The Structure and Evolution of Gap Outflow over the Gulf of Tehuantepec, Mexico. *Mon. Wea. Rev.*, **126**, 2673-2691
- Strub, P. T., and C. James, 2000: Altimeter-derived variability of surface velocities in the California Current System: 2. Seasonal circulation and eddy statistics. *Deep-Sea Research II*, **47**(4), 831-870
- Stumpf, H. G., and R. V. Legeckis, 1977: Satellite Observations of Mesoscale Eddy Dynamics in the Eastern Tropical Pacific Ocean. *J. Phys. Oceanogr.*, **7**(5), 648 – 658
- Stumpf, H. G., 1975: Satellite detection of upwelling in the Gulf of Tehuantepec, Mexico. *J. Phys. Oceanogr.*, **5**, 383-388
- Sweet, W., R. Fett, J. Kerling, and P. La Violette, 1981: Air-sea interaction effects in the lower troposphere across the north wall of the Gulf Stream. *Mon. Wea. Rev.*, **109**, 1042-1052
- Thorncroft, C. D. and K. Hodges, 2001: African Easterly Wave Variability and Its Relationship to Atlantic Tropical Cyclone Activity. *J. Climate*, **14**, 1166-1179
- Thorncroft, C. D., D. J. Parker, R. R. Burton, M. Diop, J. H. Ayers, H. Bariat, S. Devereau, A. Diongue, R. Dumelow, D. R. Kindred, N. M. Price, M. Saloum, C. M. Taylor, and A. M. Tompkins, 2003: The Jet2000 Project - Aircraft Observations of the African Easterly Jet and African Easterly Waves. *Bull. Amer. Meteor. Soc.*, **84** (3), 337-351 MAR 2003
- Thum, N., S. K. Esbensen, D. B. Chelton, and M. J. McPhaden, 2002: Air-sea heat exchange along the northern sea surface temperature front in the eastern tropical Pacific. *J. Climate*, **15**, 3361-3378

- Trasviña, A., E. D. Barton, J. Brown, H. S. Velez, P. M. Kosro, and R. L. Smith, 1995: Offshore wind forcing in the Gulf of Tehuantepec, Mexico: the asymmetric circulation. *J. Geophys. Res.*, **100**, 20649-20663
- Vecchi, G. A., S.-P. Xie, and A. S. Fischer, 2004: Ocean-Atmosphere Covariability in the Western Arabian Sea. *J. Climate*, **17**, 1213-1224
- Wallace, J. M., T. P. Mitchell, and C. Deser, 1989: The influence of sea surface temperature on surface wind in the eastern equatorial Pacific: Seasonal and interannual variability. *J. Climate*, **2**, 1492–1499
- Ward, M. N., and C. K. Folland, 1991: Prediction of seasonal rainfall in the north Nordeste of Brazil using eigenvectors of sea-surface temperature, *Int. J. Climatol.*, **11**, 711-743
- WCRP, 2000: CLIVAR Africa implementation plan. Informal Rep. 5/2000 ICPO, Publication Series 35, 35 pp.
- Webster, P. J., V. O. Magana, T. N. Palmer, J. Shulka, R. A. Tomas, M. Yanai, and T. Yasunari, 1998: Monsoons: Processes, predictability, and the prospects for prediction
- Weisbrg, R., and T. Weingartner 1988: Instability waves in the equatorial Atlantic Ocean. *J. Phys. Oceanogr.*, **18**, 1461-1657
- Weisberg, R. H., 1984: Instability waves observed on the equator in the Atlantic Ocean during 1983. *Geophys. Res. Lett.*, **11**, 753-756
- Wentz, F. J., and T. Meissner, 2000: Algorithm Theoretical Basis Document (ATBD), version 2. AMSR-E Ocean Algorithm. Remote Sensing Systems Tech. Rep. RSS 121599A-1, 55 pp
- Wentz, F. J., C. Gentemann, D. Smith, and D. Chelton, 2000: Satellite Measurement of Sea Surface Temperature Through Clouds. *Science*, **288**, 847-850
- Wilkin, J. L., H. G. Arango, D. B. Haidvogel, C. S. Lichtenwalner, S. M. Glenn, and K. S. Hedström, 2005: A Regional Ocean Modeling System for the Long-term Ecosystem Observatory. *J. Geophys. Res.*, **110**, C06S91
- Xie, P., and P. A. Arkin, 1997: Global Precipitation: A 17-year monthly analysis based on gauge observations, satellite estimates, and numerical model outputs, *Bull. Am. Meteorol. Soc.*, **78**, No. 11, pp. 2539-2558
- Xie, S.-P., T. Miyama, Y. Wang, H. Xu, S. P. de Szoeke, R. J. Small, K. Richards, T. Mochizuki, and T. Awaji, 2007: A Regional Ocean-Atmosphere Model for Eastern Pacific Climate Towards Reducing Tropical Biases. *J. Climate, in press*

- Xie, S.-P., H. Xu, W. S. Kessler, M. Nonaka, 2005: Air-Sea Interaction over the Eastern Pacific Warm Pool: Gap Winds, Thermocline Dome, and Atmospheric Convection. *J. Climate*, **18**, 5-20
- Xie, S.-P., 2004: The shape of continents, air-sea interaction, and the rising branch of the Hadley circulation. *The Hadley Circulation: Past, Present and Future*, J. F. Diaz and R. S. Bradely. Eds. Springer-Kluwer Academic, 2005
- Xie, S.-P. and J. A. Carton, 2004: Tropical Atlantic variability: Patterns, mechanisms, and impacts, " In *Earth Climate: The Ocean-Atmosphere Interaction*, C. Wang, S.-P. Xie and J.A. Carton (eds.), Geophysical Monograph, **147**, AGU, Washington D.C., 121-142
- Xie, S.-P., 2004: Satellite observations of cool ocean-atmosphere interaction. *Bull. Amer. Meteor. Soc.*, **85**, 195–209
- Xie, S.-P., W. T. Liu, Q. Liu, and M. Nonaka, 2001: Far-reaching effects of the Hawaiian Islands on the Pacific ocean-atmosphere system. *Science*, **292**, 2057-2060
- Yu, Z., J. P. McCreary Jr., J. A. Proehl, 1995: Meridional asymmetry and energetics of tropical instability waves. *J. Phys. Oceanogr.*, **25**, 2997-300
- Zebiak, S. E., 1993: Air-sea interaction in the equatorial Atlantic region. *J. Climate*, **6**, 1567-1586
- Zhang, G. J., and M. J. McPhaden, 1995: The relationship between sea surface temperature and latent heat flux in the equatorial Pacific. *J. Climate*, **8**, 589-605